This electronic thesis or dissertation has been downloaded from Explore Bristol Research, http://research-information.bristol.ac.uk

Author:
Russell, Bethany K

Title:
DEVELOPING CAPABILITIES IN MATERIALS AND MANUFACTURE FOR WIND TURBINE BLADES BY THE APPLICATION OF AN ANHYDRIDE-CURED EPOXY RESIN SYSTEM

Author:
Russell, Bethany K

Title:
DEVELOPING CAPABILITIES IN MATERIALS AND MANUFACTURE FOR WIND TURBINE BLADES BY THE APPLICATION OF AN ANHYDRIDE-CURED EPOXY RESIN SYSTEM

DEVELOPING CAPABILITIES IN MATERIALS AND MANUFACTURE FOR WIND TURBINE BLADES BY THE APPLICATION OF AN ANHYDRIDE-CURED EPOXY RESIN SYSTEM

Bethany K. Russell

A dissertation submitted to the University of Bristol in accordance with the requirements for award of the degree of Doctor of Philosophy in the Faculty of Engineering

December 2020

Word count: 51061

ABSTRACT

The increased demand for sustainable energy sources has resulted in a boom for the wind energy industry. The industry therefore wants to manufacture wind turbine blades at higher production rates and for the blades themselves to be more efficient. The project undertaken assessed anhydride-cured epoxy resins alongside a novel manufacturing process, vascular curing, to develop both material and manufacturing capabilities to achieve these goals.

This study initially characterised three anhydride-cured epoxy resins developed by Hitachi Chemical Company Ltd. These resins were shown to offer increased interfacial adhesion to glass fibres over an amine-cured epoxy industry benchmark, with an increase in interfacial shear strength of 24-66% depending on the anhydride. Preliminary trials on carbon fibre were conducted due to demand for larger blades to increase energy efficiency, this again showed improved performance was attained for the anhydride-cured epoxy resin, with a 34% increase in interlaminar shear strength over the industry benchmark.

Composite wind turbines are currently manufactured using long and low temperature cure cycles to prevent thermal gradients developing in the part which lead to manufacturing defects, ultimately limiting the production rate and incurring manufacturing costs. A proof-of-concept setup to experimentally validate vascular curing for thick composite sections (50 mm) was developed. This novel manufacturing process embedded a secondary heating mechanism within the part. It was shown both experimentally that the embedment of a vascule network reduced the observed peak exotherm on average by 25 °C.

Overall, this work has furthered knowledge of anhydride-cured epoxies and showcased that they could have much wider use, due to the improved interfacial adhesion to both glass and carbon fibres. The vascular cure laboratory-scale setup has been developed and shown exciting preliminary results. With further development both these resins and processing methods could both be integrated into current industrial processes to enable better quality wind turbine blades to be made at higher production rates to meet demand.

DECLARATION

I declare that the work in this dissertation was carried out in accordance with the requirements of the University's Regulations and Code of Practice for Research Degree Programmes and that it has not been submitted for any other academic award. Except where indicated by specific reference in the text, the work is the candidate's own work. Work done in collaboration with, or with the assistance of, others, is indicated as such. Any views expressed in the dissertation are those of the author.

SIGNED: ....█████████████................. DATE: 01/12/2020

ACKNOWLEDGEMENTS

AUTHORS CONTRIBUTIONS

The work presented in this document was done by B. K Russell unless otherwise indicated using references. The following contributions are recognised:

Ian Hamerton (University of Bristol) and Carwyn Ward (University of Bristol) have given supervision and guidance throughout this work and have provided feedback on this manuscript.

Sarah Azamtu (University of Bristol) conducted some of the microbond tests during her MEng dissertation project which was co-supervised by B. K Russell. Her work focused upon repeating microbond experiments on glass fibres to increase the sample size, which was required to obtain a representative sample set. Further to this Usman Sikander (University of Bristol) provided his microbond data for Prime^{TM} 20LV on glass fibre to use in addition to data collected by the author to increase the data set for this work.

Dr Matt O'Donnell (University of Bristol), conducted the finite differential analysis (FDA) work and helped the author develop the finite element analysis model used in this work. The FDA model develop by O'Donnell allowed for the optimised cure cycle for the vascular cure work to be determined. This was used by the author in the experimental setup developed in the work. The FDA model was developed as it would allow for quicker simulations to be conducted. The work conducted in collaboration with O'Donnell has been written into a journal paper which is currently awaiting publication.

PUBLICATIONS

Journal publications

B. K. Russell, S. Takeda, C. Ward, I. Hamerton, Examining the influence of carboxylic anhydride structures on the reaction kinetics and processing characteristics of an epoxy resin for wind turbine applications, *Reactive and Functional Polymers*, 144, 2019 (104353).

Under review and pending publication

M. P. O'Donnell, B. K. Russell, H. Jones, Y. Mahadik, S. Takeda, I. Hamerton, C. Ward, Cure management of thick composites using vascular networks.

Conference papers and presentations

B. K. Russell, C. Ward, S. Takeda, I. Hamerton, Initial studies to characterise a polymer matrix for use in composite wind turbine blades, 21st International Conference on Composite Materials (ICCM21), Xi'an, China, 2017.

B.K Russell, I. Hamerton. S. Takeda, C. Ward, Embedding vascular networks into thick composite parts as thermal management tools for cure processing: a feasibility study, 11th International Conference on Manufacturing of Advanced Composites (ICMAC 2018), Nottingham, UK, July 2018.

B. K. Russell, C. Ward, S. Takeda, I. Hamerton, The processing of a novel polymer matrix for wind turbine blades, Thermosetting Resins, Berlin, Germany, September 2018.

B. K Russell, C. Ward, S. Takeda, I. Hamerton, Development of resin and curing process for wind turbine blades, 8th Annual Conference of the CDT in Advanced Composites for Innovation and Science (ACCIS), Bristol, UK, April 2019.

x

CONTENTS

LIST OF TABLES

LIST OF FIGURES

LIST OF ABBREVIATIONS AND ACRONYMS

AFM	Atomic force microscopy
CAPRI	Controlled atmospheric pressure resin infusion
CFRP	Carbon fibre reinforced polymer
CNT	Carbon nanotube
CNF	Carbon nanofibre
CPT	Cured ply thickness
CTE	Coefficient thermal expansion
DSC	Differential scanning calorimetry
DGEBA	Diglycidyl ether bisphenol-A
DMA	Dynamic mechanical analysis
EB	Electron beam
EEW	Epoxy equivalent weight
FTIR	Fourier transform infrared
FRP	Fibre reinforced polymer
FDA	Finite difference analysis
FEA	Finite element analysis
GFRP	Glass fibre reinforced polymer
gsm	Gramme per square metre
HCCL	Hitachi chemical company Ltd.
HAWT	Horizontal axis wind turbine
HBP	Hyperbranched polymer
ID	Inner diameter
IFSS	Interfacial shear strength
ILSS	Interlaminar shear strength
LFA	Laser flash analysis

LbL	Layer by layer
LVR	Linear viscoelastic regime
MDSC	Modulated differential scanning calorimetry
NCF	Non-crimp fabric
OD	Outer diameter
PCA	Principle component analysis
PTFE	Polytetrafluoroethylene
POSS	Polyhedral oligomeric silsesquioxane
RTM	Resin transfer moulding
SEM	Scanning electron microscopy
SCRIMP	Seemann composite resin infusion process
SBS	Short beam shear
STA	Simultaneous thermal analysis
SFF	Single fibre fragmentation
SD	Standard deviation
TGA	Thermogravimetric analysis
TRL	Technology readiness level
UV	Ultra-violet
UATR	Universal attenuated total reflection
VAP	Vacuum assisted process
VARI	Vacuum assisted resin infusion
VAWT	Vertical axis wind turbine
WTBs	Wind turbine blades
3D	Three dimensional
2D	Two dimensional

LIST OF COMMONLY USED SYMBOLS

T_e	Absolute temperature
E_a	Activation energy
γ_c	Char yield
η^*	Complex viscosity
υ	Crosslink density
$\alpha,$	Degree of cure
α_p	Degree of cure at maximum rate of reaction
ρ	Density
G^*, G', G''	Dynamic modulus: complex, storage and loss respectively
E^*, E', E''	Elastic modulus: complex, storage and loss respectively
l_e	Embedment length
d_f	Fibre diameter
σ_f	Fibre strength
v_f	Fibre volume fraction
R	Gas constant (8.314 J K^{-1} mol^{-1})
Q	Heat flow
β	Heating rate
T_g	Glass transition temperature
R	Gas constant
F	Maximum force
T_o	Onset of polymerisation temperature
ω	Oscillation frequency
T_{max}	Peak exotherm temperature
δ	Phase difference
$P (P_w, P_c)$	Power (P_w = total wind power, P_c = power coefficient)

A	Pre-exponential factor
k	Rate constant
$\dot{\alpha}$	Rate of cure ($d\alpha/dt$)
ΔH_c	Reaction enthalpy
ΔH_{pc}	Residual cure
G^*, G', G''	Shear modulus: complex, storage and loss respectively
τ	Shear stress
S	Skewness
C_p	Specific heat capacity
l	Specimen length
h	Specimen thickness
b	Specimen width
T_0	Temperature of onset of polymerisation
κ	Thermal conductivity
$\propto_D$	Thermal diffusivity
t	Time

1 INTRODUCTION

1.1. Motivation

Since the industrial revolution (1800s) the global population started to exploit fossil fuels - coal, oil, and gas - to meet its energy demands, which have only kept increasing. Today fossil fuels are used in everyday life to generate electricity, as fuel for transportation and for heat. Fossil fuels are not only a limited resource but contribute to the emissions of carbon dioxide and other greenhouse gases, which act to trap heat within the atmosphere and thus lead to global warming. To reduce emissions from energy generation there is a global shift to sustainable, greener energy production.

Wind is one of the most practical sources of sustainable energy, and therefore wind turbines are of great interest to generate electricity. As the wind passes over the blades of the wind turbine it creates lift, causing the rotor (which is connected to a generator) to rotate, in turn outputting electrical energy. Between 2007 and 2010 the installed capacity to harvest wind energy worldwide, increased from 94 GW to 197 GW [1], and reached 435 GW at the end of 2015 [2]; it continues to grow.

Current wind turbine blades (WTBs) are large structures, with blades approaching 80 m in length, and have variable thickness from root to tip, with root sections being up to 60 mm thick [3]. At thick sections, curing of composite parts becomes more complex as there are temperature gradients through the thickness. There is an initial lag in the cure at the centre of the part, and once cure starts the heat generated during the exothermic cure reaction is slower to dissipate leading to thermal spiking. In combination, these

heighten the risk of runaway reactions (causing an exotherm) which would ultimately lead to the loss of the part. To mitigate these issues manufacturers currently opt for long low temperature cure cycles, thus incurring high manufacturing costs and limiting part turnover. However, there is a shift within the composites industry toward faster manufacturing and therefore shorter cure cycles (with lower peak exotherms) to enable faster production rates in order to meet the greater demand for composites and at more affordable prices is desired [3–8].

As the demand for wind energy is increasing, the drive to build larger more efficient WTBs is also increasing. Glass fibre is widely used in the manufacture of WTBs as they offer the best cost-performance to meet the requirements for the current WTBs. However, to meet the demand for larger more efficient blades, carbon fibre or hybrid composites will be required. Carbon fibres have much higher stiffness and lower density and therefore at longer blade lengths, less material is needed to meet the structural performance requirements and thus makes the cost: performance ratio swing in favour of carbon fibre.

This project was undertaken with sponsorship from Hitachi Chemical Company Ltd. (HCCL). HCCL is a supplier of chemical raw materials and is a subsidiary to Hitachi Ltd., a wind turbine blade manufacturer.

HCCL had developed an anhydride-cured epoxy resin which was evaluated within this project. In the literature it has been reported that anhydride-cured epoxies typically have low reaction enthalpies and reduced cure shrinkage compared to their amine cured counterparts, which are much more widely used by industry.

As discussed, the desire to manufacture wind turbine blades at higher production rates with faster optimised cure cycles and to have resin systems that could be exploited in carbon fibre or hybrid composite systems in order to meet the demand for larger blades is of great importance to the industry.

1.2. Project aims and objectives

The thesis aims to address the following research question: 'Can anhydride-cured epoxy resins offer performance gains in terms of material properties and manufacturing in large-scale composite structures?'

Based on this, the project took a three-pronged approach: firstly, assess the properties of these HCCL resins, secondly assess their interfacial adhesion for both glass and carbon fibre systems. Thirdly, the project looked to develop a new process technology, vascular curing, which could offer a unique solution to allow for faster production of WTBs.

The objectives of the thesis can be summarised as:

1. Characterise the anhydride-cured epoxy resin as supplied by HCCL. Assessing the effect of the anhydride structure on the resin properties and comparing these to a commercially available diamine-cured epoxy resin widely used in the WTB industry.

2. Assess the interfacial performance of the anhydride-cured HCCL resin on the glass fibre reinforcement currently used by HCCL. There is a major drive in the WTB industry to move toward carbon/hybrid composites to build larger more efficient WTBs. Therefore, assessing the anhydride-cured resin interfacial adhesion on carbon fibres with different sizings /surface treatments was an objective of this work, in order to help inform HCCL's carbon fibre selection.

3. Develop a proof-of-concept experimental setup to demonstrate the technology of vascular curing. Assess if this novel manufacturing method can improve cure homogeneity in thick parts and thus enable gains in manufacturing capabilities.

1.3.   Thesis structure

Based on the research objectives the thesis is presented as:

Literature review (Chapter 2):

This section discusses the current state of the art wind turbines both in terms of materials used and the manufacture methods employed. The resins and fibres used, and the advancements being made to improve laminate performance, including the role of the interface and the methods employed to improve the adhesion between the resin and fibre, is discussed. The review delves into the current manufacturing challenges and the novel methods currently being explored to mitigate these and increase manufacturing production rates.

Methodology (Chapter 3):

Provides details of the resin formulations, fibres and manufacturing methods used in this work. The principles of techniques used from resin characterisation methods to short

beam shear testing will be outlined in this section. The section will also present a review of different methods available to assess interfacial shear strength and justify why microbond testing was selected.

Resin characterisation (Chapter 4):

Three different anhydrides were assessed to understand the effect of the structure on the resin performance including thermal and mechanical properties, viscoelasticity, and thermal degradation. This evaluation led to the down selection of one resin system as it gave the best overall performance and was later used in the work on vascular curing (Chapter 7). To facilitate modelling of vascular curing, in Chapter 7, characterisation of the resins conductivity and specific heat capacity was required. All measured properties were benchmarked against an amine-cured epoxy resin industrially used for WTBs.

Resin cure kinetics (Chapter 5):

The resin cure kinetics for the anhydride-cured epoxies were assessed by adopting Kissinger and Ozawa kinetics models. Structure-property relationships were determined for the anhydride networks. However, these models assume first-order kinetics, and may not be most appropriate for further process modelling. To allow for more accurate modelling of the development of cure, using isothermal DSC methods an appropriate autocatalytic cure kinetics model was selected.

Laminate performance (Chapter 6):

The interfacial adhesion of the resin to the fibre is critical to the overall composite laminate performance. This was assessed from both macromechanical (short beam shear interlaminar shear strength) and micromechanical (microbond) testing. Development of an in-house microbond procedure formed a large part of this work. The wind industry is moving toward carbon fibre systems due to demand for larger blades, therefore evaluating the effect of sizing of carbon fibre on the interfacial adhesion was to be evaluated to inform HCCLs choice of carbon fibre. However, the microbond setup in its current state, although suitable for glass fibre, was limited for its evaluation of carbon fibre, therefore only preliminary assessment of the anhydride-cured resin on carbon fibre was conducted.

Optimisation of cure at thick composite sections – vascular curing (Chapter 7):

In this chapter, the novel manufacturing method of vascular curing was evaluated. Finite element analysis was used to model the reduction in exotherm and cure variation for the cure of thick composite sections with and without a central vascule. A laboratory scale proof-of-concept experimental setup was developed which enabled oil to be circulated at a controlled temperature through a central vascule within a glass fibre reinforced polymer (GFRP) laminate (50 mm thick). The results from the model are validated using the experimental setup and understanding of the effect of the vascule of cure uniformity was determined.

Conclusions and suggestions for further work (Chapter 8):

The overall findings of the project are concluded in this chapter. This chapter also discusses future work which would be undertaken to further this research, mainly focusing on the vascular cure manufacturing process which could be developed further to take it to the next technology readiness level (TRL).

2 LITERATURE REVIEW

Wind power has been exploited for thousands of years, for many tasks from grinding grain to pumping water [9]. James Blythe, a Scottish engineer, is widely credited with the development of the modern wind turbine as it was the first which facilitated the generation of electricity. In 1887, at his home in Scotland, Blythe built a vertical axis wind turbine (VAWT), constructed with four sails attached to arms at right angles to each other, supported by a wooden tripod (Figure 1). To generate electricity Blythe utilised technologies that also came about during the industrial revolution, such as the Robinson anemometer, dynamo generator, and Faure accumulator, the design was patented in 1891. At the time, Blythe's invention was met with significant scepticism as wind turbines were seen to be large and inefficient, therefore fossil fuels led the way for large scale energy generation [10].
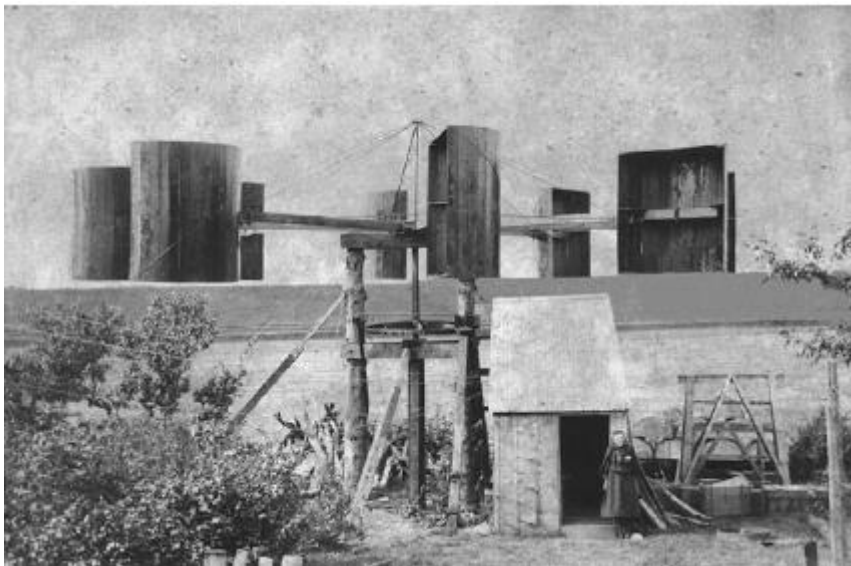
Figure 1: Photograph of the wind turbine developed by James Blythe. Taken from [10].

In the later 20th century understanding of aerodynamics and advanced materials, including the development of composite materials, led to wind turbines being re-examined as a viable means of sustainable large-scale energy generation; especially as

there is now a pressing concern to look for alternative energy resources due to climate change and limited supplies of fossil fuels [11, 12].

2.1. Types of wind turbines

There are two classes of wind turbine blades, identified by the direction of the shaft and rotational axis, examples of each are shown in Figure 2:

- Horizontal axis wind turbine (HAWT) - shaft mounted horizontal to the ground.
- Vertical axis wind turbine (VAWT) - shaft normal to the ground.

a)   b)
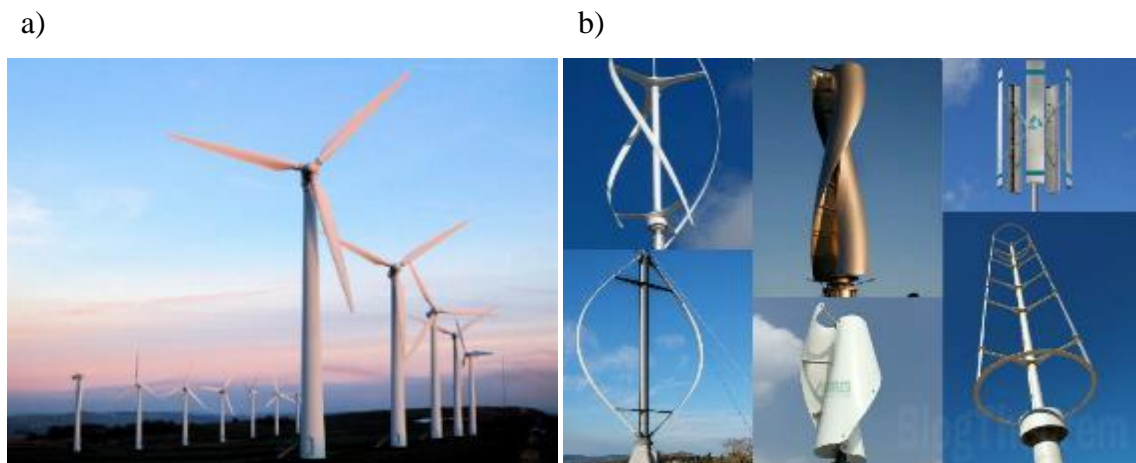
Figure 2: Examples of two classes of wind turbine blades a) HAWT and b) VAWT.

VAWTs demonstrate multiple advantages over HAWTs. They do not require any additional mechanism to face the wind, and heavy generator equipment can be mounted on the ground instead of being at the top of the tower. However, VAWTs rely on a drag mechanism, which limits its efficiency as they have a tip speed ratio which cannot exceed one; limiting its maximum efficiency which is far exceeded by the three-bladed HAWTs more widely available. Thus, VAWTs have not been developed for mass market at present. With continued development, they should not be disregarded for future wind farms, as they could be packed much more closely and thus could be used in more residential and industrial areas where space is limited [13, 14, 15].

Within VAWTs there is much greater variety of designs seen, a very interesting example is presented by Jayaram *et al.* [15], who investigated a biologically inspired blade shape based on a maple/triplaris seed. Several blade geometries inspired by these seeds were modelled using finite element analysis (FEA) and subjected to static loading conditions. These initial studies showed very promising results as the maple seed design was shown

to deflect less compared to a standard blade and could withstand high wind speeds of 55 m s^{-1}. The study also investigated tubercles, inspired by those found on the leading edge of humpback whale flippers, as seen in Figure 3, which have been shown to increase the mammal's ability to manoeuvre through the water, due to the increase in lift and decrease in drag afforded to it from these growths. In the study by Jayaram *et al.* [15], the addition of tubercles to the blade designs further reduced the deflections observed, thus were highlighted as points of interest for further work.
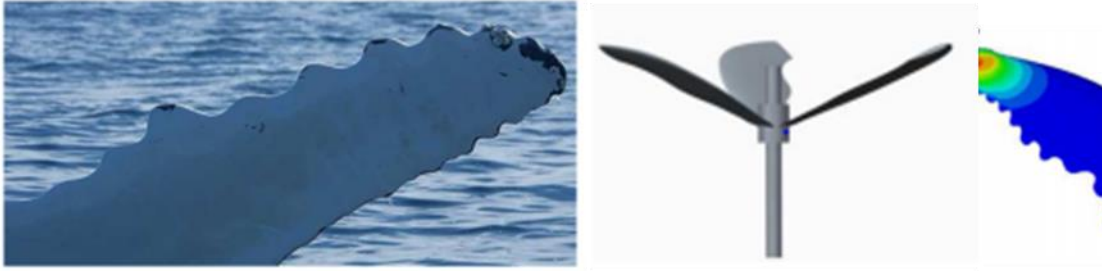
Figure 3: a) Image of humpback whale flipper, b) Maple turbine setup used in study by Jayaram *et al.* [15], c) stress analysis of one blade from the maple seed inspired blade design with addition of tubercles. Image reconstructed from [15].

HAWTs however, dominate todays large scale market for wind turbine blades, due to their increased rotor control through pitch (rotation of blades to control amount of lift) and yaw control (keeping the rotor facing wind direction) [9]. Hence the focus of this work is directed towards HAWT blades, and therefore further mention of wind turbine blades (WTBs) will refer to HAWTs.

2.2. How do HAWT wind turbines generate power?

Wind turbines harness a fraction of the power available in order to turn a generator, thus converting kinetic energy into useful electrical power [16, 17]. The total power available to the turbine, P_W, is given by Equation 1.

$$P_W = P_c \cdot \frac{1}{2} \cdot \rho \, A_s \, V^3$$

(1)

where, A_s is the swept area of the turbine blades ($A_s = \pi r^2$, where r is half the rotor diameter), ρ is the density of the air, V is the wind speed through the turbine and, P_c is the power coefficient [18, 19, 20]. The power coefficient is defined as 0.593, based upon Betz's law, which showed regardless of wind turbine blade design the maximum amount of kinetic energy which can be extracted from the wind into mechanical energy turning

a rotor is 59.3%. In practice typical HAWTs achieve efficiencies of 70-80% of the Betz power coefficient due to energy losses (*i.e.* drag) [9]. To improve the efficiency and increase the power output there has been extensive development within the industry including: aerodynamics, blade shape and geometry, and configuration [9].

2.3.   Materials for wind turbines

Historically, wind turbines were made from wood or aluminium, but from the 1970s, with the advancement of composite materials this moved to glass fibre composites [3]. Now, carbon fibre systems are also commonly used and becoming of increasing importance due to the industrial demand for larger more efficient wind turbine blades and this will be discussed in Sections 2.4.1 and 2.4.2. Polyester resins were previously widely employed within the wind turbine industry as they demonstrated good mechanical properties, thermal stability, and environmental resistance, while being easily processable without requiring a post cure step. However, in recent years, epoxy resins have superseded polyesters and have become the industry standard as they exhibit superior mechanical properties and offer better fatigue resistance, resulting in much more durable composite laminates [20]. Since epoxies were first used commercially in 1947, they have been utilised in many sectors from coatings, electronics, adhesives and in structural applications in both construction and composite fields [21].

2.4.   Epoxy resins

Traditionally, the industry has had a 'one size fits all' approach and, as much stimulus for epoxy resin development has come from the aerospace industry which has very different performance demands to the wind industry, this has meant that the development of advanced composite materials for the specific application to WTBs has yet to be fully exploited.

The manufacturing challenge faced by the wind industry, as with other industries including aerospace and automotive, is to develop resin systems that are infusible and offer quick, low temperature cure cycles to increase productivity and reduce costs [22].

During their lifetime (20-30 years), WTBs are expected to undergo 100 million load cycles (high cycle fatigue) whilst being exposed to harsh environments with lightning strikes, erosion from wind particles, impact events, and variations in operating temperature with icing events being common place [3].

9

For structural epoxies the most frequently used resins are oligomers based on the diglycidyl ether bisphenol A (DGEBA), produced from the reaction of epichlorohydrin and bisphenol-A in an *O*-alkylation reaction, given in Figure 4. DGEBA accounts for approximately 75% of the global epoxy consumption [21]. DGEBA exhibits several favourable properties including thermal resistance, toughness, rigidity, good adhesion, and chemical resistance; this explains its prominence in the field, and why it is used in this work [21].
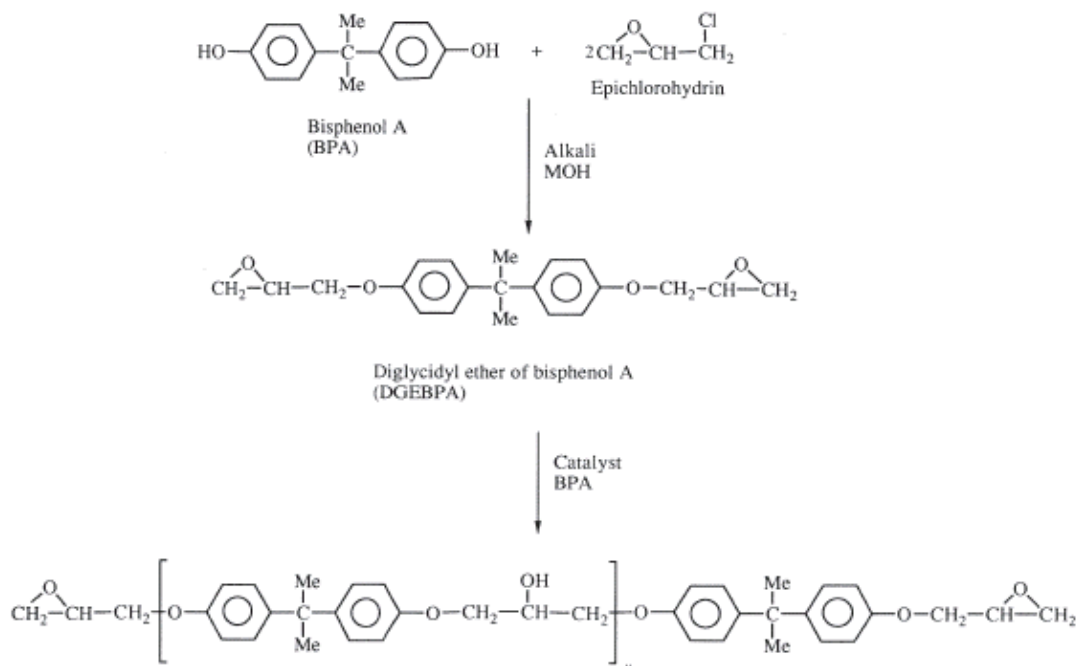
Figure 4: DGEBA production from epichlorohydrin and bisphenol-A. Reconstructed from [23].
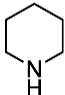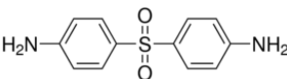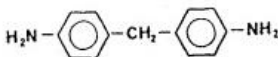
The versatility of epoxies and the reason why they have found use in so many industrial fields is that they have the ability to undergo cure with a wide variety of curing agents [23] including amines [24], anhydrides [25, 26] thiols [27, 28, 29], and imidazoles [30]. The properties of the cured resin are dictated by the structure of epoxy and curing agent selected, the resin formulation, the addition of initiators, diluents, plasticisers, toughening agents, and finally the curing processes which it undergoes [31–35].

In 2001, it was seen that amines were the largest class of curing agents (as used by volume) taking 50% of the US market; the second largest group was carboxylic acids and anhydrides, making up 36%, followed by the third class which was phenols and

related substances (14%) [36]. Amines have been utilised most widely as there are many types (aromatic, aliphatic, primary, and secondary *etc*) which can be reacted with different epoxies to produce resins with different properties. These can then be exploited in a vast array of applications.

Some typical properties of epoxy resins cured with different hardener summarised from [34] are presented in Table 1. These properties are dependent upon the inherent flexibility and molecular motions of the cross-linked network, and the crosslink density of the network. Modifiers can also be added to the resin formulation i.e. rubbers or thermoplastics, these are often used to increase the fracture toughness of epoxy resins which are inherently brittle. There are many references which provide a good source of information upon effect of epoxy and cure agent structure-property relationships and the effect of thermoset modifiers [29, 34, 35].

Table 1: Typical properties of epoxy resins cured with different curing agents [34].

Curing agent	Cycloaliphatic amine – piperidine	Aromatic amine-diphenyl sulfone (DDS)	Aromatic amine-methylenedianiline (MDA)
Cure agent structure			
T_g (°C)	75-110	190	144
Tensile strength, psi (MPa)	7,000-9,000 (48 – 62)	8,550 (59)	8,100 (56)
Flexural strength, psi (MPa)	13,500-15,500 (93-107)	17,500 (121)	17,900 (123)
Compressive strength, psi (MPa)	13,000-16,000 (90-110)	-	10,500 (72)

Anhydride-cured epoxies, although not as widely studied, have been reported in literature to have numerous benefits over their amine cured counterparts. The reaction of anhydrides and epoxies is characterised by a reduced enthalpy of reaction (lower exotherm) and although long cure cycles are required to reach full cure, the resulting resins have low shrinkage and consequently reduced residual stresses locked within the cured laminates [37, 38]. In addition, anhydride-cured epoxy blends yield lower mix viscosity without the need for diluents, making them ideal for infusion processing [38]. It is these properties which make them particularly appealing as resin systems for the wind turbine industry, and hence why an anhydride-cured epoxy was investigated in this work.

Reactions between epoxies and anhydrides require an initiator in order to allow the cure reaction to occur at low temperatures at a quick rate, and often tertiary amines are used [23]. There is general agreement amongst researchers that the reaction is an anionic one, but the nature of the mechanism still provokes some debate. Fischer [39], suggested the tertiary amine first reacts with the anhydride to form a zwitterion, which then reacts with the epoxide ring, prior to polymerisation. In contrast, Tanaka and Kakiuchi [40], suggested the reaction required the presence of an additional proton donor as a co-catalyst which can form a complex with the amines. This complex is then able to ring open the anhydride to form a zwitterion which can then polymerise with the epoxy. It was also suggested that these proton donors may not need to be added but could be formed *in-situ* during the reaction. It was suggested that the isomerisation of the epoxide may form a proton donor in the form of an allyl alcohol [25]. However, Antoon and Koenig [41] dispute this as they did not observe the formation of allyl alcohol in their FTIR spectroscopic investigations into the cure mechanism, but they hypothesise the initiation is due to the presence of a proton donor could come from the presence of alcohol functional groups with the resin constituents [26, 43].

As will be discussed, in this work the amine and the anhydride are pre-mixed before the addition of the epoxy, and therefore the first suggested reaction mechanism (Fischer [39]) is presumed, and the general reaction scheme is shown in Figure 5. However, the fact that so many reaction mechanisms have been suggested only emphasises that the mechanism is not fully understood and is perhaps more complex with multiple reactions occurring [36].
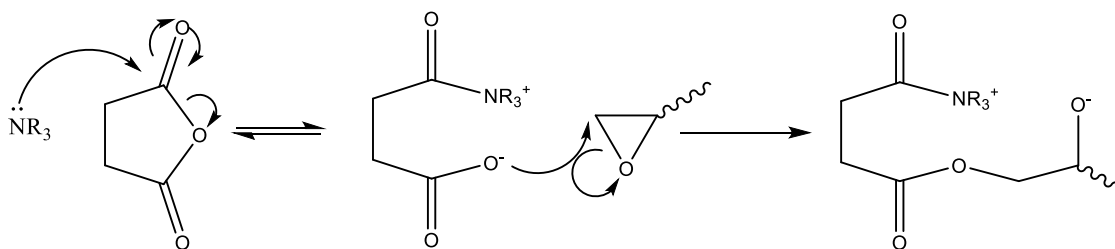
Figure 5: Scheme showing mechanism of tertiary amine-initiated epoxy-anhydride reaction.

2.4.1. Development of more efficient WTBs

Owing to increased demand for wind energy and a limited number of wind farms, there is increased demand to build more efficient wind turbines. It is understood that the larger the swept area of the wind turbine blade the more energy can be generated (shown in Equation 1, Section 2.2), therefore the larger the turbine blades the greater the energy efficiency achieved. Hence, as shown in Figure 6, there is a growing trend toward larger more efficient turbines: from 100 kW wind turbines in the 1980s with 17 m rotor diameters, to 2 MW wind turbines in the late 2000s with rotor diameters of 80 m. Current designs for future wind turbine blades look to surpass 100 m length [18, 43, 44].

In 2018, General Electric announced plans to develop the largest offshore WTB. The Haliade-X will be a 12 MW turbine with blade length of 107 m, thus having the capacity to produce 45% more energy than any current offshore turbine blade [44].

Figure 6: Development of wind turbine blades from 1980s to 2020 (predicted). Taken with permission from [45].

2.4.2. Fibre selection

Within a composite material the fibres provide the strength and stiffness, and therefore the structural performance to the material/part [45]. They are held in place by the matrix which also helps to transfer the stresses between the fibres. Many types of fibres are available in the industry, which are selected depending upon performance requirements from natural fibres (*e.g.* jute, hemp, flax [46]), polymers (*e.g.* high modulus polyethylene, such as Dyneema[TM] [47, 48], or Kevlar[TM]), ceramics [46], and more widely used carbon [49], and glass [49, 50]. The two fibres discussed herein are glass and carbon as they have been most widely exploited in the WTB industry.

There are many varieties of glass fibre, the chemical composition of the fibre can be tailored to afford it specific properties, for further details of composition and resulting fibre type and properties the author refers the reader to [51]. E-glass fibres (so called due to their high electric resistance) have been used extensively in the wind industry due to their relatively low cost, offering the best cost-performance ratio for small/mid-size current WTBs, Table 2 gives some typical E-glass fibre properties.

However, with the growing demand for larger WTBs, carbon fibres are being used more widely, as they are lighter but stiffer than glass fibres.

With increasing size, gravitational forces and inertial loads tend to dominate over aerodynamic loads [52]. Moving to carbon fibre reinforced polymer (CFRP) systems allows for potentially thinner, stiffer and lighter blades to be designed [3] compared to if these requirements were met by GFRP laminates, as shown in Table 2.

Table 2: Comparison of typical E-glass and carbon fibre properties [53, 54].

Fibre type	Stiffness/ GPa	Tensile strength/ MPa	Density/ g cm^{-3}	Cost/ $ lb $^{-1}$
E-glass	72	3500	2.54	2
Carbon	350	4000	1.77	30

Carbon fibres have already been exploited by several large wind turbine manufactures such as Vestas and Gamesa [54]. Switching to carbon fibre is reported to have enabled Vestas to increase blade length by 5 m without any additional weight gain. Vestas uses

HexPly^{TM} M79 prepreg (produced by Hexcel) in the manufacture of blades which are approaching 100 m in length, as the use of the carbon fibre results in exceptionally strong and stiff laminates which are lighter than those made with glass fibre [55].

Hybrid composites pose a very interesting alternative to either pure glass or carbon systems. To meet the same structural stiffness as GFRP laminate, by moving to carbon fibre there is a weight saving of 76%, yet the cost is 3.5 times more expensive. However, with hybrid composites 50:50 glass and carbon laminates, the increase in cost can be reduced to 2.9 times cost of the GFRP laminate but with a 58% weight saving [53]. Hybrid composites therefore offer a compromise between cost, mechanical properties, and weight.

Currently, the longest wind turbine blade, 88.4 m, is made from carbon/glass hybrid composites [56]. Hybrid composites employ carbon fibre to regions where it is needed most and all glass fibre in other areas, therefore achieving a better cost: performance ratio balance. For example, adding carbon fibres to the spar flange, where they work in one of two ways, increase the stiffness for a given weight or reduce the weight for a given stiffness. Yet keeping the spar shear web with just glass fibre as the mechanical properties in the region are lower and can be obtained with more economical glass fibre, as shown Figure 7 [58, 59].
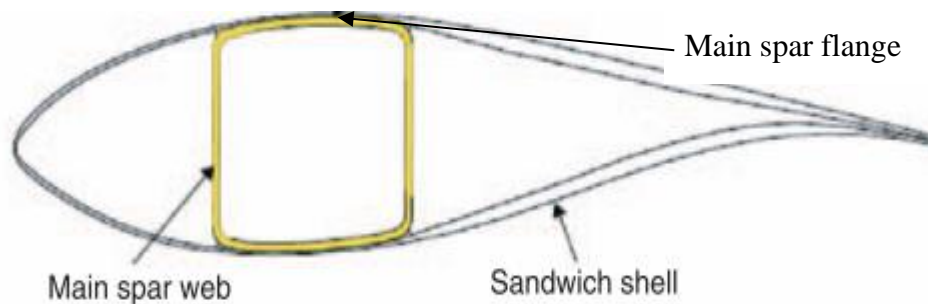
Figure 7: Wind turbine blade aerofoil cross-section, showing spar web and flange. Taken from [58].

2.4.3. Sandwich structures

Composite WTBs are often formed as a combination of monolithic (composed of only fibre reinforced polymers) and sandwich structures. Sandwich structures are formed of two thin composite laminates with a thick lightweight core material sandwiched between them. These types of composites are exploited in the industry as they offer high strength, buckling resistance and bending stiffness, yet they are lighter than a monolithic structure.

These sandwich materials may be homogeneous (*i.e.* polymeric foams and balsa wood) or non-homogeneous such as honeycomb type (Nomex[TM]) [58]. These will not be discussed in much detail herein as the project focused upon monolithic structures. However, the author points the reader to the following references [59, 60, 61].

2.4.4. Interfacial properties

For overall laminate performance the interface between the resin and fibre is critical, as poor adhesion results in poor transfer of stress between fibres. Generally, weak interfaces lead to low strength in the composite laminate. However, very strong interfaces can lead to brittle failure. In the manufacture of fibres, a thin film of sizing agent (emulsion/solution consisting of polymeric components) after surface treatment (*e.g.* electrolytic oxidation or plasma treatment) is applied. These processes occur to firstly protect the fibres from damage and improve their handleability, but also to increase the interfacial adhesion to the resin. Fibre sizing/surface treatments can be used to improve the resin/fibre interface. The stress transfer mechanism between the resins and fibres is determined by the interface, the main mechanisms of which are observed and can be exploited in thermoset composites. These are explained briefly herein.

2.4.4.1. Chemical bonding

Adhesion through chemical reactions (covalent or ionic) between the resins and functional groups on the fibre surface lead to high interfacial shear strength.

Optimising the selection of the resin and fibre which have best compatibility is vital. Developing sizing/coupling agents which promote chemical bonding between the fibre and matrix has been widely studied.

A simple example of this is in silane coupling agents, typically used on glass fibre surfaces, which have the general chemical formula $R\text{-}Si\text{-}X_3$, where X represents a readily hydrolysable group. These groups are hydrolysed within the solution to which the fibre is exposed to form a silanol, these groups compete with water to form hydrogen bonds with the fibre surface. The fibres are subsequently dried and condensation reactions occur at the silanol/fibre junction and neighbouring silanol molecules. This forms a polysiloxane layer bound to the fibre which presents functional groups (R) to the matrix, which can subsequently allow for chemical bonding at the interface [61], shown in Figure 8.

16
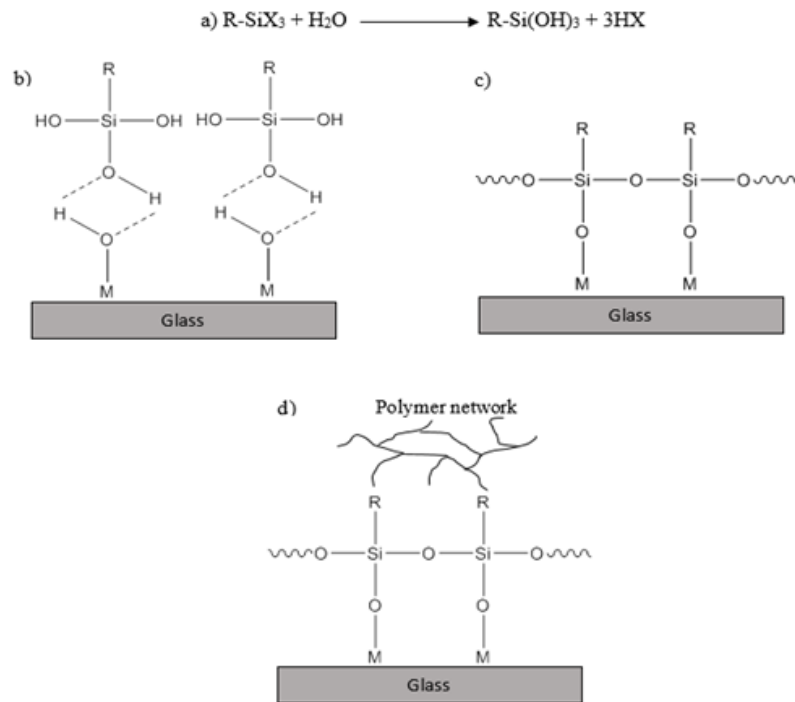
Figure 8: Silane coupling agents on glass fibre. a) hydrolysis of the organosilane to silanol, b) hydrogen bonding between silanol group and those on glass surface, c) condensation during the drying process leads to polysiloxane bonding to fibre surface and d) bonding between the functional group R of the polysiloxane and the polymer network. Reconstructed from [61].

Several recent literature references focus on optimising the carbon fibre surfaces by exploring grafting molecules to the fibre surface which can subsequently react with the polymer network on cure and thereby improve the interface between resin and fibre. There are many examples whereby chemical modification of the fibre surface has led to increased interfacial adhesion [63, 64, 65].

Henderson *et al*. [64] have developed a method to enable carbon fibres to be modified to contain desirable reactive groups. The method of modification uses click chemistry which allows the surface functionalisation to be customised to suit the chemistry of the intended resin system. Henderson *et al*. showed when the fibre was functionalised with a reactive aryl amine (at the end of the grafted molecule) there was a 220% increase in the interfacial shear strength (IFSS) over an unsized carbon fibre. It is hypothesised that this increase is achieved by the amine

17

functionalised carbon fibre reacting and covalently bonding to the epoxy resin matrix.

2.4.4.2. Mechanical interlocking

Fibre surface roughness and irregularities (*i.e.* pores) can create mechanical locking points if good wetting of the fibre surface has been achieved [66, 67]. Work by Drzal *et al*. [67] showed that fibre surface treatments which caused surface etching, thereby increasing the surface roughness, accounted for a significant increase in adhesion between the fibre and resin. A similar improvement was obtained *via* laser-induced surface structuring [68]. There are many examples of surface treatment techniques, *e.g.* plasma and etching, have been widely reported in literature to increase surface roughness and thereby increase interfacial adhesion [68–70].

It is also reported that 'fuzzy' fibres offer improved interfacial adhesion. 'Fuzzy' fibres are formed from growing carbon nanotubes (CNTs) on the carbon fibre surface. The nanotubes add to the fibre surface roughness and create mechanical interlocking points around which the epoxy resin becomes anchored [71]. Sager *et al*. [72] showed that the interfacial shear strength of epoxy/carbon fibre composites could be increased by 71% by coating randomly aligned multi-walled CNTs on to the surface of the fibre (carbon-T650) by means of thermal chemical vapour deposition.

2.4.4.3. Electrostatic attraction

Electrostatic attraction between two oppositely charged ions occurs at the interface. This is only a minor part of the total bonding strength. The effect is achieved often in the surface treatment of glass fibres. The surface of the fibre presented may be anionic or cationic depending upon the oxide of the glass and the pH of the solution used to apply the coupling agents. For example, on glass fibres ionic functional silanes may be used as coupling agents which, if anionic, would attract cationic functional groups within the matrix or *vice versa* [61].

The interfacial adhesion between the resin and fibre is critical to the mechanical performance of the composite laminate. Firstly, the effect of the anhydride structure on the interface with the commercial glass fibres supplied was determined. Secondly, as HCCL are interested in moving toward carbon fibre laminates, it was critical to assess

the effect of different carbon fibre sizings/surface treatments and recommend which would be most appropriate.

2.5.   Wind turbine manufacture

Composite WTBs are typically manufactured in two half shell mouldings. Adhesives are used to attach spar boxes or web stiffeners (if not cured within the aerofoils) and to attach the two halves together [73]. Once the adhesive cures, coatings and paint are applied to the blade. The flange and bolts are then attached to the blade root section to enable the blade to be securely attached to the rotor [74]. These main manufacturing steps are shown pictorially in Figure 9.

In the early years of composite WTBs, wet layup was used. This manufacturing technique uses paint brushes and rollers to push resin into the fibres within an open mould. The major drawback to this method is it is highly labour intensive, and the parts produced are of low quality. Low quality parts are produced as low viscosity resins must be used in order to impregnate the fibres and the process often leads to air being entrapped in the part [75]. However, with the advancement of composite manufacturing methods, prepreg and resin infusion now lead the way.
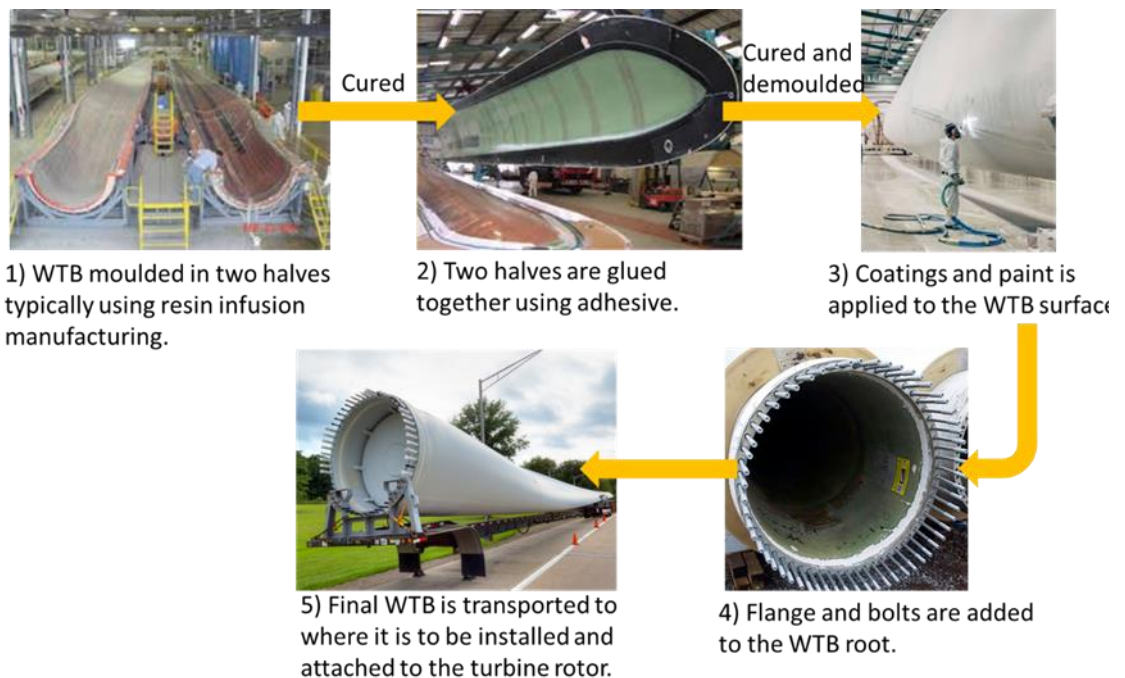
Figure 9: Pictorial representation of the major steps in the manufacture of a wind turbine blade (WTB). Diagram reconstructed from images from [77, 78, 79].

Prepreg (pre-impregnated) refers to material which is supplied with the uncured resin already combined with the fibre (fabric or unidirectional). This material is most widely used by the aerospace industry but is used by some wind turbine manufactures including Vestas and Gamesa for the manufacture of their WTBs [79]. Previously prepreg was better than infusion as it was more consistent, enabled better control of fibre orientation and thus resulted in better mechanical properties [79]. Although this statement was appropriate previously, in recent years with the advancement of infusion methods and infusible resin systems, parts of comparable mechanical properties can be produced with resin infusion [75]. However, prepreg technology could allow for higher levels of automation, for example they can be used with automated tape placement equipment. Prepreg materials are much more costly and pre-impregnated material has a shelf-life (of several months) and specific storage conditions (*e.g.* -18 °C) [79].

However, vacuum assisted resin infusion (VARI) is the process most widely employed in the industry as it is often cheaper compared to the prepreg process [79]. VARI is used by HCCL and will therefore be the technique used throughout this work and will be the focus of the following discussion.

The VARI process is conducted with the dry fabric preforms, prefabricated parts, other components and auxiliary materials being laid up on a female mould. Prefabricated parts can include blade roots and spar caps which are difficult to infuse. Other components may include sandwich structure cores or lightning protection copper meshing. Auxiliary materials are those required for the infusion process, such as resin distribution mesh and vacuum bagging materials. The rigid tooling lies on the side of the laminate which will be the outer surface of the blade with the flexible tooling on the inside (Figure 10 [22]) and uncured resin, which has been degassed, is then drawn through the part using a vacuum. Once the fabric has been fully impregnated the inlets are sealed and the whole part is cured, at the temperature and duration specified for the resin used [82, 83, 84].
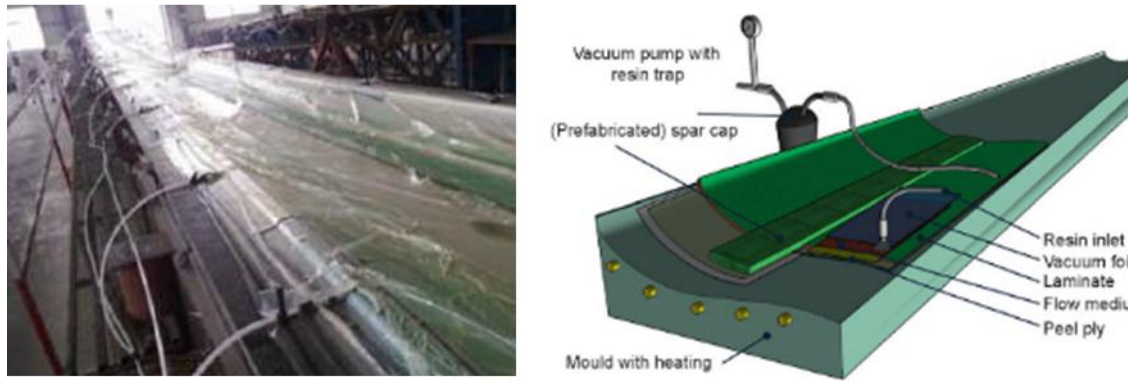
Figure 10: a) Image of infusion of wind turbine blade [81], b) Schematic of infusion manufacturing process for WTBs [22].

The speed of infusion and the nature of the cure cycle are important cost drivers with this manufacturing process. The infusion time is affected by several factors such as: the distribution mesh selected; fabric permeability, resin system used, and infusion strategy employed *i.e.* number and location of resin inlets [83, 85]. For effective infusion the resin viscosity should be below 0.5 Pa.s at the processing temperature [86, 87], and understanding the resin cure kinetics is key to ensure that the resin does not gel within the time scale of the infusion processes at the processing temperature. The number of resin inlets can be varied based on the understanding of the infusion process and the flow path distance, which is shorter for faster curing resins and hence requires more inlets. By fully appreciating all the steps of the process the fibre impregnation and fibre volume fraction can be maximised ensuring optimum laminate performance.

There are many variations of VARI methods from Seemann composite resin infusion process (SCRIMP), controlled atmospheric pressure resin infusion (CAPRI) and vacuum assisted process (VAP), to name but three, the reader can refer to [88, 89] for greater details on these methods. SCRIMP may be one of the more common variations used for WTB manufacture [90, 91], in this variation consumable distribution media and flow channels are strategically used to enable the resin to flow across the part surface and speed up the infusion processes [85].

Future developments in VARI manufacture may incorporate more automated layup techniques for fibre placement in order to speed up the manufacturing process, increase reliability and reduce fibre misalignment [89]. Zhu *et al.* [90], have developed an automated setup for laying up of non-crimp fabric (NCF) for application to wind turbine blade manufacture for preform as used in VARI manufacturing. The setup described has

21

shown that the viability of the method to laydown fabric with good accuracy and reduce fabric misalignment even when laid up over 3D-mould. With further work to increase the deposition rate to enable it to exceed the current manual layup times, it will also look to scale up to enable deposition of larger fabric panel widths.

2.5.1. Optimised curing of WTBs

As discussed, there is increased demand to increase production rates of WTBs. WTBs are large parts, in excess of 80 m in length, with complex geometries of variable thicknesses from root (50-80 mm) to tip (20 mm) [91]. Therefore, obtaining uniform temperature profiles during cure to minimise process induced stresses is critical to manufacturing.

Thermal gradients form due to two issues: (i) the external heating, be that from oven or autoclave, does not reach all internal points simultaneously, thus creating thermal gradients for the heat to be transferred to the middle of the section; (ii) in thick sections the heat generated due to the exothermic reaction of curing fails to dissipate through the part, often creating spikes in the internal temperature. If not controlled, thermal spiking can lead to run-away reactions (exotherms) which could be detrimental to the component. Even if this happens to a lesser extent, this could result in localised thermal degradation of the resin.

The thermal gradients cause a build-up of residual stresses in the laminate. The thermal gradients lead to variations in degree of cure which results in spatially varying thermal expansions. The spatial varying thermal expansions result in non-uniform chemical shrinkage, locking in residual stresses in the composite part. Ultimately, if these stresses are sufficiently large then defects such as transverse cracks and delamination are initiated, thus reducing the mechanical performance of the manufactured part [85, 95, 96]. Figure 11, shows catastrophic failure of a wind turbine blade, this failure was attributed to the presence of manufacturing defects.

Figure 11: Catastrophic failure of wind turbine blade due to manufacturing induced defects. Taken from [94].

Bogetti and Gillespie [95] examined the development of residual stresses in thick composite sections by studying the effects of the processing history (cure cycle), laminate thickness, resin cure shrinkage, and laminate stacking sequence on the incurred residual stresses. The results of this study showed that overall, the residual stresses increased with laminate thickness, cure cycle temperature ramp and resin shrinkage, thus showing the strong dependence upon the processing history.

To prevent large thermal gradients and to ensure uniform curing throughout thick composite parts, it is necessary to minimise possible exotherms and reduce residual stresses. Consequently, WTB manufacturers opt to use long, low temperature cure cycles, but inevitably this leads to increased manufacturing costs and a slow production rate [1, 2, 3]. As discussed, the industry is currently looking toward developing novel manufacturing methods or resin systems to move toward faster production of blades and overall reduction in the manufacturing costs.

Developing new manufacturing techniques, which enable optimised production of thick composite sections, is an area of research in which there is a lot of activity [102, 103]. Over the last decade many novel processes have been brought to light. These methods can be broadly split into two groups depending on the location of the heat/energy source: external or internal. The following section will review these methods and present vascular curing as a new method which will be developed within this work.

2.5.1.1. External energy source

- *Apparatus*

As blades continue to increase in size, they will soon exceed the current size limitations of both ovens and autoclaves. By directly heating the mould the thermal losses are reduced compared with oven curing which heats the surrounding environment. On mould heating utilises hot oil or hot steam to control the temperature of the mould, the hot oil/steam is circulated through channels in the mould. This method has numerous advantages including that it over comes current oven capacity limitations, saves energy and can have greater temperature control than in oven as thermocouples/infrared sensors can be used for feedback control [104, 105].

Abdalrahman *et al*. [102], looked to optimise the design of integrally-heated composite tooling, in particular assessing the effect of the heating channels shape and the layout of the elements within the tool. These channels are circulated with oil to heat the mould during the cure. They found that circular cross-sectional shaped elements laid out with a parallel arrangement resulted in better temperature uniformity over the tool surface when compared to zigzag and helical layouts or square or rectangular element cross-sections.

In the on mould heated tool reported by Marsh [101], the heating elements are positioned between two aluminium foil sheets. The foil allows the heat from the heater elements to be evenly distributed across the tool surface. The design can also allow for zonal heating, with different heating profiles being used in different areas of the tool surface. It is suggested that on-mould heating may be more desirable to in-tooling heating as on-moulding heating lies closer to the part and therefore minimises thermal losses and enables easier maintenance. It is also more flexible and could conform easily to the contours of the part geometry.

Quickstep^{TM} processing has been reported as an out-of-autoclave manufacturing technique for wind turbine blades, in which glycol-based heat transfer liquid (higher heat capacity and thermal conductivity to air) is circulated in a flexible bladder that surround the part in a pressure chamber. This system showed an improvement in cure cycle times, as the part heated up at a quicker rate, exothermic heat could be taken out and cool down was much more rapid [103].

- *Staged curing*

Staged curing works by adding plies sequentially until the desired thickness is reached. After each additional partial cure occurs, the laminate is exposed to temperature which allows the material to gel and consolidate, and for some of the exothermic reaction energy to be expended. Once the desired thickness is reached, a second cure is conducted, and in this stage the remaining exothermic reaction energy is released and the part is fully cured [104].

The main benefit of this technology is that it can be used with the current generation of materials and equipment without the need for greater investment by a company. It also mitigates two major issues with curing of thick composite sections: consolidation, and dissipation of heat generated during the exothermic reaction. Furthermore, the partial cure of the laminate after each addition means that there is little chance of thermal spiking as the exothermic reaction is controlled.

The successful use of staged curing was demonstrated by White *et al.* [104] in the layup of carbon fibre/epoxy prepreg laminates which were composed of 24 plies. The staged curing was conducted in two stages, with layup of 12 plies initially. These plies were partially cured with a 1-hour dwell at 116 °C and once cooled to room temperature the remaining 12 plies were laid up. The laminate was then subjected to either cure cycle a) 177 °C for 2 hours or b) 116 °C for 1 hour then further 2 hours at 177 °C. The staged curing was tested to see the impact of this upon interlaminar shear strength (ILSS) and void content compared to a 24-ply laminate cured with standard cure cycle (b). In the laminates which were staged cured there was reduction in void content from 3.6% (non-staged) to less than 1%, with no variation between different staging cure cycles. The reduction in void size was attributed to the staged curing allowing the resin to cool after the consolidation step which allows the voids, which developed under pressure and increasing temperature, to collapse. This in turn lead to the increase in ILSS (approximately 20%), which as a test is known to be very sensitive to void content [104].

Skordos and Kratz in 2018 [105], also studied staged curing by examining the effect of the degree of cure on the sub-laminate on the resulting laminate properties. In this feasibility study 40 mm laminates (30 plies) were made through sequential addition of sub-laminates (5 plies), which were partially/fully cured in a hot press, shown in Figure 12. In this work both simulation and experimental results were obtained, and both showed a 75% reduction in temperature overshoot in the same manufacturing time, for

the laminate composed of glass fibre/epoxy (HexPly913, Hexcel). From experimental testing to assess ILSS and mode-I fracture toughness (double cantilever beam), it was shown that, compared to conventional techniques, using this stage curing approach did not affect the mechanical performance of the laminate if pre-cure kept at 60% or less. If the resin was cured to greater extent during the staging process, the resin became too highly crosslinked to effectively bond with the subsequent sub-laminate and thus the mechanical performance was reduced. This method offers exciting possibilities, further work identified the possibility that this technology could be used in conjunction with a robotic placement head to allow for the manufacture of complex parts.
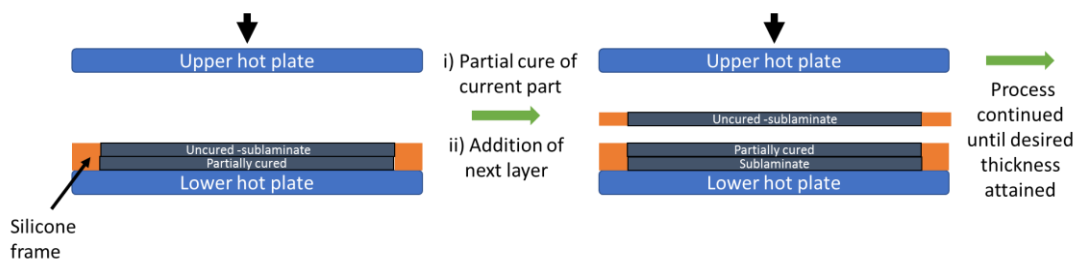
Figure 12: Schematic of Layer by Layer (LbL) process setup. Reconstructed from [105].

This method has been developed for prepreg material, where sequential layers can be easily added and consolidated on to the partially cured layers and could therefore be considered as one way to produce WTBs that are manufactured from prepreg material. However as discussed, this project is focused upon VARI manufacturing methods. The application of staged curing to this manufacturing technique does not seem to be applicable.

- *Radiation curing*

Radiation curing uses a radiation source such as gamma-rays [100, 106], X-rays [99], ultra-violet (UV) light [107–109] microwaves or electron beams (EB) [110–114] in order to activate the resin to react and cure [115]. Methods such as gamma rays and X-rays have been shown to be used to cure thick composites with thicknesses 20-30 mm, yet have the drawback of posing significant health risks and therefore cure has to be conducted with a lead shield [113, 115]. This may be more difficult and expensive for curing of larger parts like that of a wind turbine blade. UV curing on the other hand has been more widely adopted especially for 3-D printed parts [107] and for

dental composite fillings [116], yet owing to the limited penetration depth (20 mm) at these wavelengths [99], it cannot be considered in this application. These methods (EB, X-rays and UV) require cationic initiated cure mechanisms and therefore conventional thermosetting resins currently used by the industry may not be suitable. Thus, resin development for resins which are initiated in this manner may be required in order to use resin systems which offer the same performance as traditional resins [99].

Microwave curing has gained significant traction as a radiation method that could be used to cure thick composite laminates [117, 118]. It works as high-energy electromagnetic waves (microwaves) interact with the resin, which is a dielectric material, causing the dipoles (molecular/atomic) to orientate. It is the motion of the dipoles which generates electromagnetic energy in the form of heat, and subsequently cures the resin. Unlike conventional heating, this energy is transmitted through the volume of the laminate, reducing the thermal gradients which traditionally develop and instead allows for a process which cures the resin from the inside-out [117].

Li *et al.* [110] studied indirect microwave curing for thermoset CFRP laminates of 20 mm thickness and found that the peak exotherm temperature, residual stresses, and cure times were greatly reduced. The observed interlaminar performance of the cured laminate over a conventional thermal cured part was attributed to the improved internal quality brought about by the uniform cure associated with microwave curing.

Although microwave curing has been shown to use 80% less energy compared to autoclave curing and reduce cure cycle time [118]. There are some challenges for it to be readily adopted by industry. Microwave ovens can be a substantial capital investment particularly to enable cuing of large structures. Tooling currently used is not suitable for microwave curing - metal tooling is a microwave reflector; borosilicate glass however is suitable and must be used. Other process materials must also be microwave compatible *i.e.* infusion consumables [118].

2.5.1.2. Internal energy source

- *Resistive/inductive heating*

Resistive heating offers another approach to conventional curing methods, where conductive elements are embedded within the laminates. An electrical current can then be passed through these conductive elements and it can provide resistive heating on the

inside of the laminate, either in synergy with external heating or as an out-of-autoclave technique which removes this need. The main outcomes from the studies conducted show that this approach does enable the cure cycle time to be reduced and mechanical performance to be increased mainly as the conductive fibres add additional reinforcement to the laminate [117].

Lu *et al*. [119] demonstrated the use of CNT films embedded at the surface of GFRP laminates (6 plies) as a method of out-of-oven curing, when connected to an electrical power supply. The study showed laminates cured by the carbon nanotube film had comparable mechanical properties, in terms of tensile strength and modulus, to conventional oven cured laminates. This process was also shown to be more efficient than traditional oven curing by saving both time and energy (energy consumption saving of 86% compared to oven process). The CNT film can also be used post-cure as a means of de-icing the composite whilst in service. However, it was reported that although this method was effective for thin laminates, on moving to thicker (16-ply) laminates the temperature difference across the laminate was too great (15 °C) and did not enable the laminate to be cured. To enable this method to be used to cure thick composite sections it will be critical to examine the ability to embed the film within the laminate and to assess its effects on mechanical performance.

A commercial example of an inductive curing method is the Lantor PowerSHEAT. These nonwoven veils made with a polyester material with carbon additives have been showcased at the JEC Europe composites show and conference in 2015 [120, 121] These mats, in contrast to the films developed by Li *et al*. [119], are reported to be easily embedded within epoxy and polyester resin composite systems becoming an integrated part of the structure. Once connected to an external electrical power source the veils can be heated to 160 °C, thus are viable as an internal heating source to be used during cure [122, 123]. Although this has been released to market, there is little research data available on this in terms of its effectiveness compared to conventional curing and impact upon mechanical performance of the laminate. Overall, little research has been reported on conductive films for effective curing of thick composite laminates.

In carbon fibre composites, direct application of an electrical current to the fibres has enabled *in-situ* curing, without the need to embed conductive films into the laminate, using the fibres themselves as heating elements [124, 125, 126]. Hayes *et al*. [124]

examined the uniformity of heating achieved with different contact techniques (between the laminate and power supply) and evaluated the resulting degree of cure and mechanical properties (flexural strength) of the cured laminates compared to conventional oven or autoclave cured laminates. The carbon fibre/epoxy composite laminates were manufactured from prepreg material, with various thickness from 2 to 8 plies. It was observed for the 4-ply laminate that the degree of cure achieved with electrical heating (97.2%) was greater than that achieved through oven curing (94.4%). The flexural modulus was found to be very comparable matching that of oven cured laminate properties (approximately 48 GPa). Its effectiveness for thick composite laminates and the ability of this to optimise the cure cycle and reduce manufacture time and energy costs is yet to be fully examined as a viable out-of-autoclave manufacturing method for cure of large complex parts such as WTBs.

An interesting variation of inductive curing is the use of an external magnetic field to induce inductive heating [127, 128]. Ariu *et al.* [127], worked on fast cure resin systems as a potential patch repair technology. The epoxy resins used were functionalised with cobalt functionalised CNTs. These CNTs could enable the formation of through thickness networks within the resin, which increase the through-thickness thermal and electrical conductivity. As the conductive networks are part of the matrix in this way, they can accelerate the heat supply to the laminate. Formation of these conductive networks occurs in the application of external magnetic fields, which aligns the CNTs. The magnetic field in alternating current fields enables inductive heating. However, the ability for these types of systems to be used in composite laminates, especially infused systems, would be difficult. Epoxy resins containing CNTs are difficult to infuse as the loadings required to enable the formation of an effective network often create very viscous resins which cannot permeate through preforms to fully impregnate the laminate, and the CNTs can be filtered out by the fabric [128, 129]. This would have to be explored for the resin systems developed by Ariu, to assess if the networks required for effective curing could be established within infused composite parts.

- *Vascular curing*

Vascular networks are inspired by nature, as vascular networks within the body act to transport blood around the entire system, allow healing (blood clots), and enable thermal regulation. They have been exploited in composites to build functionality into cured

29

parts from self-healing [130–133], in-service thermal management tools as active/passive cooling pathways through the laminates [134] and de-icing [135, 136].

In 2016, O'Donnell *et al.* [137] modelled the use of vascules to provide a secondary heating mechanism during the cure of composite materials. In the work a finite element analysis (FEA) model was developed, using an additional Fortran subroutine (HETVAL) to calculate the heat generated and degree of cure with time. Within this work two prismatic cross-sectional geometries were modelled; rectangular and tapered (shown in Figure 13), all vascules had a radius of 5 mm.

The model utilised a gradient approach to minimise the variation from the mean cure over the cross-sectional area as a function of time, to optimise the position and temperature profile of the vascules. The results showed that for the rectangular section with one vascule in an optimised (central) location the cure homogeneity improved 28% and for tapered section with multiple vascules with optimised temperature profile the improvement would be 72%.
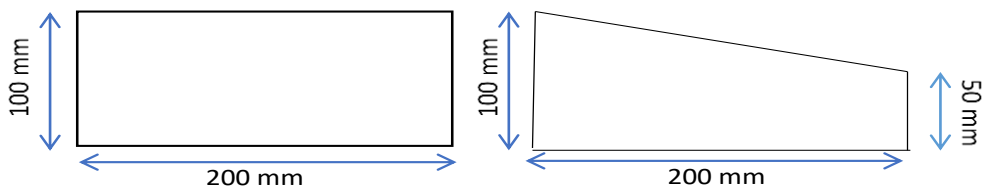
Figure 13: Prismatic section geometries used by O'Donnell *et al*. [137], a) rectangular section, b) tapered section, (figure not to scale).

This research showed the potential to improve cure homogeneity and how vascular curing could offer great advantages to the manufacture of thick composite sections. Vascular curing has not been widely studied, yet offers the unique ability to act as a secondary heating mechanism for curing thick composites and, as the vascule would remain embedded within the laminate, could be exploited post-cure for multi-functionality for applications such as those noted earlier including self-healing or de-icing. Another interesting point is that O'Donnell *et al*. demonstrated that the optimised vascule temperature profile often changed during the cure cycle with points where the temperature plateaued or increased at different rates in order to control the heat in the part, see Figure 14. Figure 14, presents some of the results from O' Donnell *et al.* [137],

showing a snapshot of the cure evolution in the FEA model for each section and the thermal profiles for both sections for the external heating and vascules. This shows how the cure can be optimised for both prismatic and wedge cross sections. Unlike other cure optimisation methods described, vascular curing could be used with currently used materials and manufacturing methods.
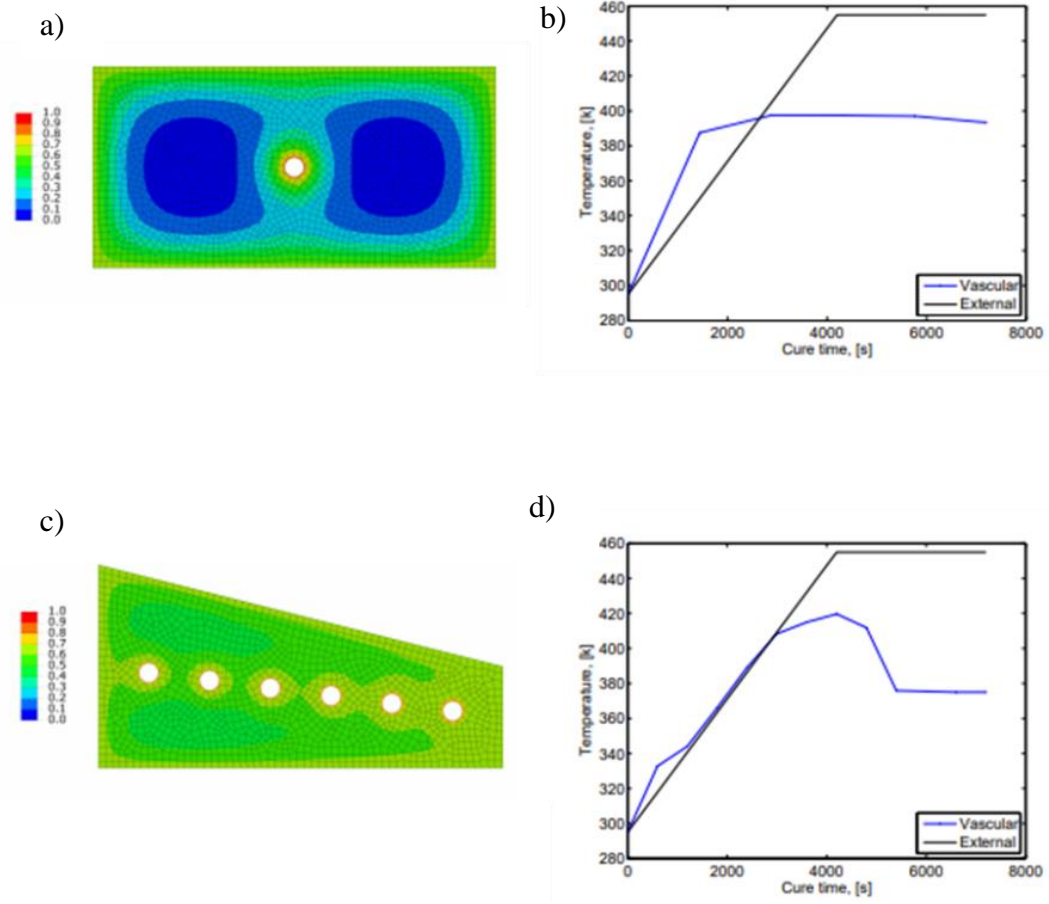
Figure 14: Vascular cure FEA modelling results from [137] a) state of cure for rectangular section mid-cycle for optimised vascule, b) temperature profile for autoclave (external) and optimised vascule for rectangular section c) state of cure for tapered section mid-cycle for optimised vascule, d) temperature profile for autoclave (external) and optimised vascule for tapered section.

However, O'Donnell *et al*. did not demonstrate the ability to embed vascules and to obtain these improvements experimentally. Within the scope of this project, an experimental setup has been developed, and a feasibility study was conducted on vascular curing as a suitable method to cure thick composite samples, such as those found at the root sections of wind turbine blades.

2.6.   Concluding remarks

As has been shown in the literature, there is growing demands in the wind turbine industry to develop material which offer enhanced performance (*i.e.* moving toward carbon fibre systems) whilst addressing the manufacturing challenges of curing such large structures, which have large thickness variability from root to tip.

Anhydride-cured epoxies are not as well characterised in the literature, yet these resins have reportedly lower reaction enthalpies and reduced residual stresses locked into the resin after cure, therefore making them very attractive to be utilised in wind turbine blades. Understanding the effect of anhydride structure on the resin properties and the interfacial adhesion to glass and carbon fibres to demonstrate if these resins systems offer the increased composite performance is desired by the industry

There are major manufacturing challenges for wind turbine blades. The literature shows that there is extensive research into novel manufacturing methods to improve cure homogeneity and thereby improve the quality of the manufactured part in thick composite structures is an area of intensive research. Vascular curing has been identified as one such method, which has been showed through numerical simulation to improve cure homogeneity and having these embedded vascular networks offer potential for multifunctionality post-cure. The vascular curing novel manufacturing method has however this had not previously been experimentally verified, within the scope of this project a proof-of-concept experimental setup was developed.

3 METHODOLOGY

This chapter will firstly provide details of the resin blend formulations used throughout this work and present the system to which these resins will be referred to as in subsequent chapters. The chapter will go onto to outline the underlying principles of several techniques which have been widely employed in this work: from resin characterisation, methods such as differential scanning calorimetry (DSC) and rheology, to the composite laminate fabrication technique of vacuum assisted resin infusion. The reader may refer to this chapter for underlying principles of these methods. Each subsequent technical chapter will include its own experimental section where the setup conditions employed to obtain the required measurements are given.

3.1. Resin formulations

3.1.1. Anhydride-cured epoxy resins

The diglycidyl ether of bisphenol A (DGEBA, **A**, approximate Epoxy Equivalent Weight (EEW) = 184 g mol^{-1}), anhydrides (mixture of 3- and 4-methyl-1,2,3,6-tetrahydrophthalic anhydride (**C**); mixture of 3- and 4-methyl-hexahydrophthalic anhydride (**D**); or methyl-3,6-endomethylene-1,2,3,6-tetrahydrophthalic anhydride (**E**)) and tertiary amine (Ancamine K54, (**B**)) were all supplied by HCCL. All monomer materials (Table 3) were used as received without further purification.

The blends were prepared by weighing the tertiary amine **B** with one of the aforementioned anhydrides **C**, **D**, or **E** into a 100 ml reaction vessel (without the lid, coated three times with mould release agent) in the desired ratio (5:85 by weight respectively) and stirring by hand at room temperature until homogenised. To this blend, the epoxy, **A** (100 by weight ratio) was added and the blend was stirred until homogenised. The formulations were prepared with an excess of epoxy, 1 mol DGEBA was reacted with 1.8 mol anhydride. The mixture was then poured into the desired mould, in which it was degassed for 15 minutes at room temperature in a vacuum chamber until no further outgassing was observed. Resin was cured in a convection oven using the

prescribed cure cycle: ramp to 75 °C at 2 °C min^{-1} and then dwell for 12 hours. The resulting blends will be referred to as **1**, **2**, and **3** as denoted in Table 4.

Table 3: The chemical structures of the component monomers used in the anhydride-cured epoxy formulations.
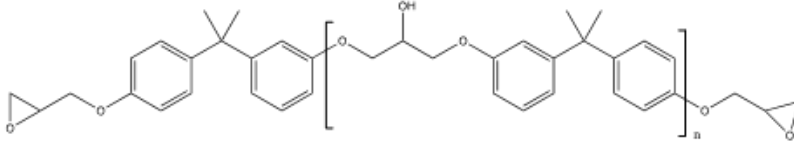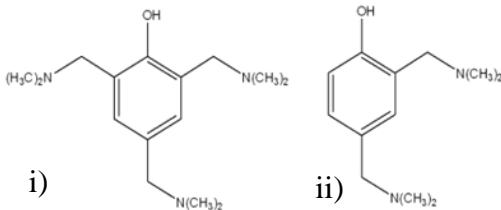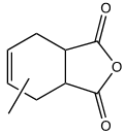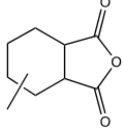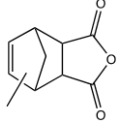
A	**(n=0-1)** bisphenol A diglycidyl ether (DGEBA)
B	Ancamine K54. Mixture of i) tris-2,4,6-(dimethylamino-methyl) phenol (90-95 wt%), ii) bis(dimethylamino-methyl) phenol (5-10 wt%)
C	3- or 4-methyl-1,2,3,6 tetrahydro-phthalic anhydride (HN2200)
D	3- or 4-methylhexahydro-phthalic anhydride (HN5500)
E	methyl-3,6endomethylene-1,2,3,6-tetrahydro-phthalic anhydride (MHAC-P)

Table 4: The assignment of blend numbers indicted by the blend conistuents.

Blend constituents	Blend number
A, B, **C**	**1**
A, B, **D**	**2**
A, B, **E**	**3**

3.1.2. Industry benchmark

Epikote^{TM} resin MGS RIMR035 epoxy resin was mixed with Epikure^{TM} curing agent MGS RIMH037 (amine curing agent) in a mixing ratio of epoxy (100): amine (28) by weight. The mixture was then degassed at room temperature until no more outgassing was observed. The cure cycle for the resin: ramp to 70 °C at 2 °C min^{-1} and then dwell for 6 hours.

3.2.   Fibres

3.2.1. Glass fibre NCF fabric

The fabric supplied was a 0°/90° Non-Crimp Fabric (NCF), LTx1240, which was biased in the 0° direction, the specification for the fabric LTx1240 is given in Table 5 [138].

H-glass was developed by Owens Cornings for applications where long fatigue life and high modulus are required, this fibre has been shown to be 20% stronger, have a 15% higher modulus, and 10 times longer fatigue life when compared to more conventional E-glass fabric, yet being substantially cheaper than carbon fibre [139]. Advantex was developed by Owens Corning, to have same mechanical properties to E-glass but minimises environmental pollutants associated with the manufacture of E-glass, hence this glass formulation is without boron or added fluorine, thus reducing polluting emissions during manufacture [140].

For the vascular cure composite laminates however, an E-glass ±45° NCF fabric was used as larger quantities of this material was available for use. This fabric, manufactured by Saertex, had a fibre areal weight (including the polyester thread stitching) of 440 gm^{-2}.

Table 5: LTx1240 Fabric Specification as provided by Owens Cornings [138].

Layer Name	1	2	3
Fibre orientation	0°	90°	Stitch yarn (Stitch type: promat, Stitch CM 4 mm/c)
Areal weight calculated / g m^{-2}	1200 ± 3%	40 ± 5%	11 ± 3%
Thread count per cm^2	4.98	3.94	2.76
Thread weight	2400	100	11
Material	WindStrand®H (H-glass)	WindStrand® 2000 Roving (Advantex)	Polyester
Manufacturer	OC_MX	OC_RC	ZE_03
Filament diameter / µm	17	13	36
Sizing compatibility	Epoxy	Epoxy	sizing free
Sizing type	WS3000	WS2000	

3.2.2. Carbon fibre fabric

An NCF carbon fibre fabric, C24k, 440, -45/+45, PB (Formax code: FCIM 359-PB), supplied by Formax (acquired by Hexcel in 2016) was used for the manufacture of carbon fibre composite laminates in this work. The fabric details here explain that the tow count was 24,000 (24k) and the fabric had a fibre areal weight of 400 gm^{-2} (including the polyester thread stitchbond).

3.3. Vacuum assisted resin infusion (VARI) processing

VARI processing has been widely used for the manufacture of wind turbine blades due to the cost-effectiveness of the technique considering the size and complex geometry of the part [141].

The fabric was cut and laid up, the details of this is presented in each chapter, as the layup (ply orientations), size and number of plies (thickness) varied depending on the test for which the laminate was being prepared for.

The double bagging method was used throughout this work. The fibre preforms were laid upon an aluminium tool plate as shown in Figure 15. The preform was placed between two layers of peel ply (PP230 aero-grade nylon-66 peel ply), peel ply prevents the infusion mesh from adhering to the laminate. Infusion mesh (FM100 infusion mesh) was used to promote resin flow over the laminate, this was placed on both the top and the bottom surface of the laminate. The mesh was cut so it its length was 3 cm short of the resin outlet, this was done to allow adequate time for the resin to infuse through the part and ensure wet out before reaching the infusion outlet tubing. At the ends of the preform (inlet and outlet) spiral tubing was placed along the width of the laminate (resin infusion spiral medium flow- outer diameter (OD) 4.5 mm). At the inlet the spiral allowed the resin to be evenly distributed across the whole width of the laminate [142].

The inner bag was then covered with breather fabric (BR180 breather layer), which was used to ensure complete evacuation of the air within the vacuum bag [142]. Two vacuum valves were placed diagonally across from one another to ensure the vacuum was evenly applied across the laminate. This was then covered with a standard vacuum bag and sealed with tacky tape- forming the outer bag. Before infusion the leak rate of the vacuum bag was checked, it was vital that the bag achieved 28 inHg and the leak rate was slower than 1 inHg per minute once the vacuum was no longer applied and the inlet/outlet tubing was clamped. All the infusion consumables were purchased from EasyComposites.

Finally, the resin inlet and outlet tubes were connected to the fluid pot and a vacuum pump, respectively. The vacuum was first applied to remove air and consolidate the fibres to the mould surface, with inlet clamped. The resin was then infused, and once fully saturated, the inlet and outlet tubes were sealed using clamps and the vacuum was

maintained on the outer bag. The laminate was cured following the prescribed cure cycle given for the resin, given in Section 3.
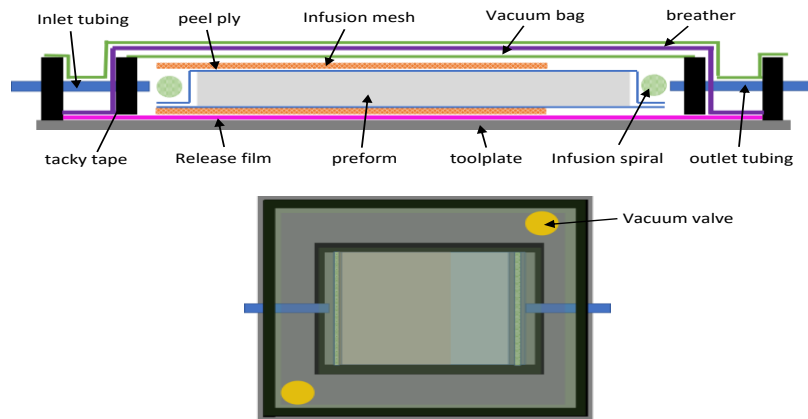
Figure 15: Schematic of VARI manufacturing process for thin laminates (<5 mm), a) side view b) top view.

However, for the infusion of thick laminates (50 mm) as manufactured for work in Chapter 7, a different infusion strategy was employed. It was found through experimental trial and error that having the inlet located at the bottom of the preform stack on one side and at the opposite end having the outlet at the top of the preform stack, as shown in Figure 16, worked best and enabled the resin to fully wet out the laminate without the formation of large dry spots. This was assessed by visual inspection the thick composite blocks once sectioned to allow the centre of the laminate to be observed.

Further details of VARI manufacturing process can be found in the following References [141–143]
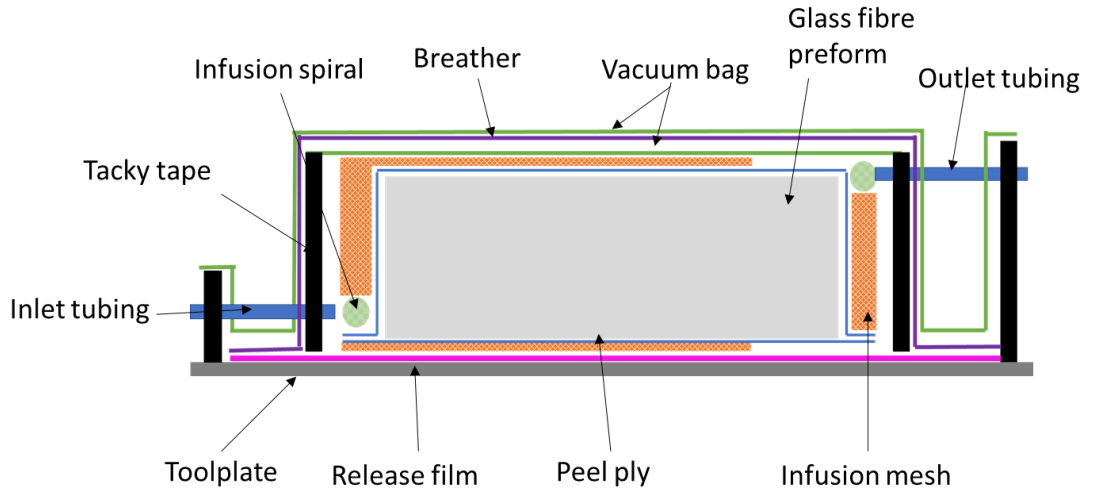
Figure 16: Schematic of VARI strategy for thick (50 mm) laminates, side view, (note outer bag also has two vacuum valves as shown in Figure 15 b).

3.4. Characterisation techniques

3.4.1. Differential scanning calorimetry (DSC)

In the DSC instrument the heat capacity of a material is recorded as it is heated or cooled with reference to an empty pan, with changes in the heat capacity recorded as changes in heat flow and thus transitions such as melts and cure reactions can be observed.

In this work heat flux DSC instruments were used, in this setup both the reference and sample pans are heated in the same cell, shown in Figure 17. The temperature differences between the two pans are recorded and converted to a power difference, from which the change in heat flow can be determined, as given in Equation 2. The difference in temperature between the reference and sample pans arises when the sample undergoes thermal processes which absorb or evolve heat, depending upon if the process is exothermic or endothermic [144].

$$\Delta P = \frac{\Delta Q}{dt} \tag{2}$$

where ΔP is the difference in power, Q is the heat flow and dt is the time step.
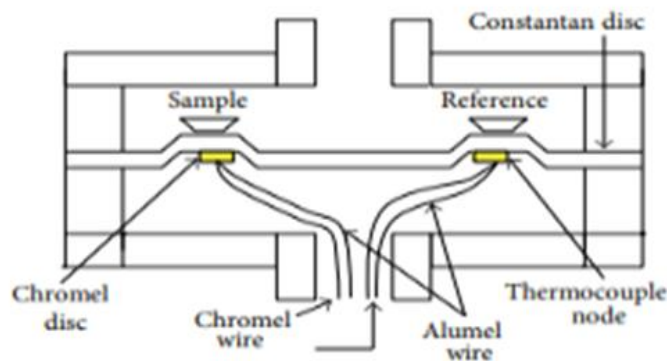
Figure 17: Schematic showing cross section of a heat-flux DSC instrument. Taken with permission from [145].

Analysing a DSC thermogram enables the materials thermal characteristics to be studied, and in the case of epoxy resins there are three key process to look for: melt, cure, and glass transition temperature (T_g). Melts can be observed as an endothermic peak in the trace as energy is taken by the samples to overcome attractive forces and allow the molecules to slip over each other. In this work no melts were observed as the resin was liquid at room temperature (temperature from which all traces were conducted). In contrast, cure is an exothermic process as energy is released by the sample as bonds form as the 3D network develops. The enthalpy of the reaction/ residual cure can be obtained by integration of the peak area. For cured/partially cured resin samples the phase transition which occurs as the sample is heated as the polymer transitions from a brittle glass to more flexible rubbery state is known as the glass transition temperature, is observed as a step change.

Modulated DSC (MDSC) was also used in this work to enable the separation of multiple thermal effects and thus allow for better interpretation of the results. MDSC works by applying a sinusoidal heating rate alongside the linear heating rate of the standard DSC [146, 147]. This was used for the analysis of partially cured resin samples as the residual exotherm peak masked the T_g, thus using MDSC allowed these processes to be separated into its reversing and non-reversing components prior to analysis.

In this work DSC has also been exploited to investigate the resin cure kinetics (*i.e.* the speed at which the polymerisation reaction progresses), using techniques commonly employed in literature and industry. Analysis of both dynamic and isothermal DSC thermograms enabled the kinetic parameters, rate of reaction and the extent of cure

40

(determined using the fractional area of the peak over the known total energy required to reach full cure plotted against time) to be obtained.

A DSC instrument was also used to determine the heat capacity of the resins, used to calculate the thermal conductivity. This was required to model the thermal properties of the resin for the vascular cure work, discussed in Chapter 7. The heat capacity was determined using the ratios method. This technique requires three experiments to be conducted over the same temperature range with the same heating rate: a. empty crucible (baseline), b. crucible + calibration (sapphire, reference) and c. crucible + sample. Figure 18, shows an example of the thermograms from each of these experiments. The specific heat capacity of the resin sample was calculated using Equation 3 [148].
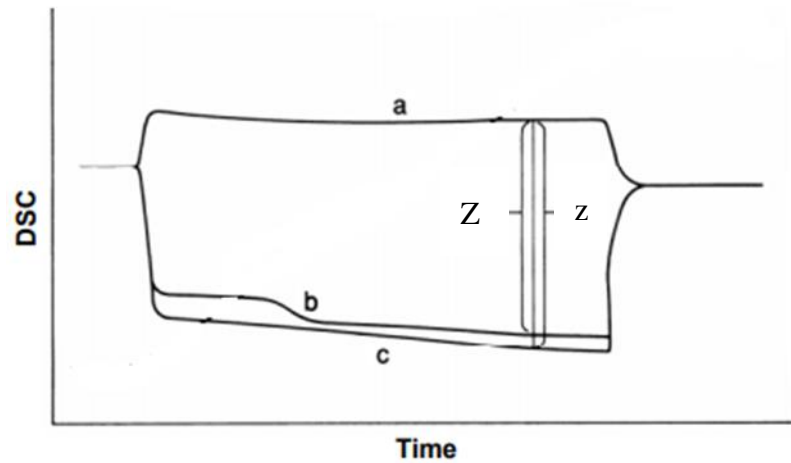
Figure 18: Representative thermogram of the three experiment setups required to determine the specific heat capacity of the sample. a) empty pan, b) sample and c) reference. Reconstructed from [148].

$$C_{p(sample)} = \frac{Z}{z} \times \frac{m_r}{m_s} \times C_{p(reference)} \qquad (3)$$

where C_p is the specific heat capacity of sample or reference, m_s and m_r are the masses of the sample and reference respectively. Z is the difference in heat flow between the sample and empty pan and z is the difference in heat flow between the mass of the reference (calibration sample) and an empty pan, as shown in Figure 18 [148].

This is a very sensitive technique and hence in each experiment the same pan was used for experiments a-c, to reduce any small effect of variation between crucibles [151, 152].

3.4.2. Dynamic mechanical analysis (DMA)

A Mettler Toledo DMA/STDA 1+ instrument was used. In this work the setup clamped the samples in tension. The cured resin sample was cut to approximate dimensions 10.5 mm x 3.3 mm x 1 mm (l x b x h) using a diamond saw. In this work, the materials response to this applied stress was characterised as a function of temperature. The extent to which the material undergoes deformation is related to its stiffness and damping, this is shown schematically in Figure 19. Resins are typically viscoelastic materials meaning that they exhibit both recoverable elastic deformation and time dependent viscous deformation when strained.

As the stress is applied sinusoidally the corresponding strain will be produced. Unless the material is perfectly elastic, the measured strain will lag the applied stress by a phase difference (δ). For a perfectly viscous material this phase difference is 90°. For viscoelastic materials, such as thermosets, this phase angle is expected to be somewhere between the two depending up temperature, time and frequency, shown schematically in Figure 19. The ratio of the peak stress to peak strain gives the complex modulus (E^*) which is composed of two components: in-phase/storage modulus (E') and the 90° out-of-phase/loss modulus (E''). The ratio of the loss and storage modulus gives the tan delta/phase angle (also referred to as damping), which is a measure of the materials ability to dissipate energy [151, 152].

In this work the DMA is used with the setup in tensile clamping mode. The method was exploited to determine the modulus of the material at its working temperature (below T_g) and as another method to assess the T_g (in this work reported as the peak in tan δ, but this could also be reported as onset in decrease in the storage modulus or peak in the loss modulus).

σ - applied stress

ε - measured strain
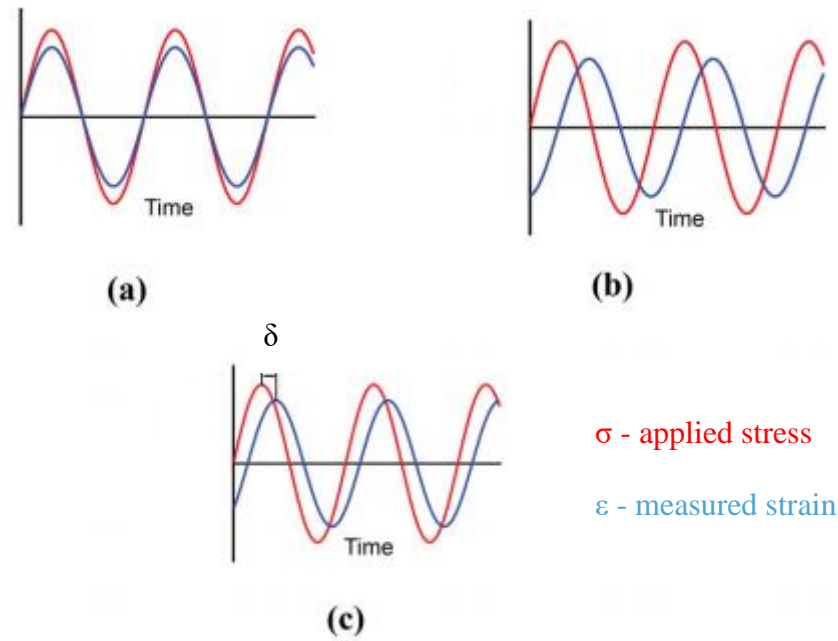
Figure 19: Material DMA responses a) elastic material, b) viscous material and c) viscoelastic material *i.e.* thermosets. Reconstructed from [152].

3.4.3. Rheology

This technique allows for the study of the viscoelastic properties of the resin. In this work a TA instruments Discovery Hybrid Rheometer HR30 fitted with 25 mm disposable parallel plates used in the oscillatory mode was utilised to monitor the rheological behaviour of the resins in isothermal conditions. The sample was subjected to shear whilst sandwiched between the two parallel plates (test gap set to 0.3 mm), with the top plate rotating whilst the lower plate is fixed, shown in Figure 20. The sample was strained as the top plate moved and the sample response determined how much torque was transmitted to the transducer (attached to the fixed plate).

To assess how the development of the 3D-network during cure affects the moduli and the complex viscosity of the resin the rheology experiments were conducted under isothermal temperature conditions at the resins prescribed cure temperature.

43
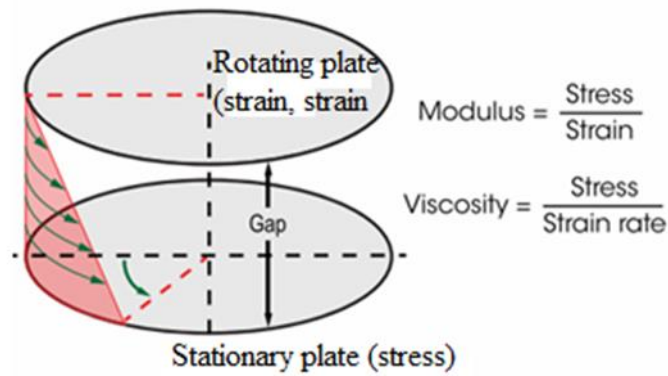
Figure 20: Diagram of rheometer setup. Reconstructed from [153].

It was vital that the strain applied to the resin was within its linear viscoelastic regime (LVR), the range of strain rates where the properties of the polymer are time-independent, thus stress and strain are proportional. This was determined by conducting a strain sweep at room temperature from 0.01% strain to 100% strain on resin blend **1**, shown in Figure 21. It was clear that the resin was in its linear regime between 1-100%, 1.5% was used in all subsequent isothermal rheology experiments (for all resins) as this seemed to be best experimentally, when higher strain rates were used when the resin was in a more cured state, and equipment became too overloaded and stopped running.
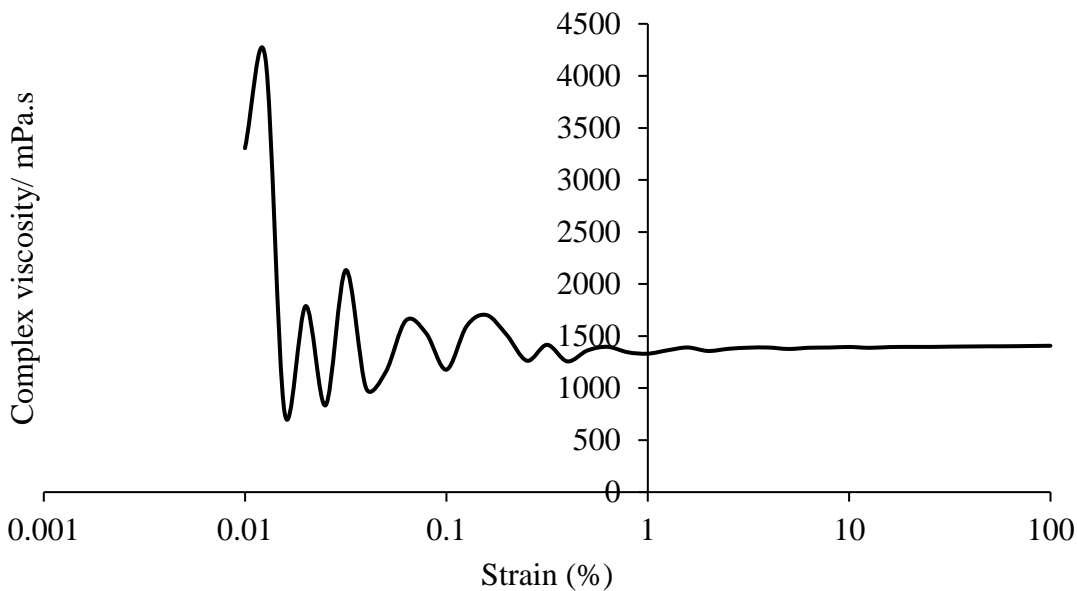
Figure 21: Results from the strain rate sweep used to assess the linear viscoelastic regime (LVR) of resin blend **1**.

From the small amplitude of deformation applied to the polymer in its linear viscoelastic regime leads to stresses which change following the given relationship in Equation 4.

$$\sigma = \gamma_0 [G' \, sin(\omega t) + G'' cos \, (\omega t)] \tag{4}$$

where, σ is the stress, γ_0 is the amplitude of the harmonic oscillation of deformations, G' is the dynamic storage modulus, G'' is the loss modulus, ω is the oscillation frequency and t is time [154–156].

G' and G'' can be calculated form the phase lag, δ between the applied stress, σ_0 and torque, γ_0 due to the viscoelastic nature of the resin. This in turn is related to respective viscosity, η' and η'', Equations 5 and 6 [154–156].

$$G' = \left(\frac{\sigma_0}{\gamma_0}\right) cos \, \delta = \eta'' \omega \tag{5}$$

$$G'' = \left(\frac{\sigma_0}{\gamma_0}\right) sin \, \delta = \eta' \omega \tag{6}$$

The complex viscosity, η^*, is given by Equation 7. Complex viscosity is the frequency dependent viscosity which is observed by subjecting a viscoeleastic material to oscillatory shear stress.

$$|\eta^*| = \sqrt{(\eta')^2 + (\eta'')^2} \tag{7}$$

The manner in which the complex viscosity develops, and the changes in moduli give great insight into the cure process and therefore rheology has been employed in this work to assess the processing of the resin in terms of the available processing window with which to infuse the part [154–157].

3.4.4. Thermogravimetric analysis (TGA)

Thermogravimetry (TG) is used to assess the degradation of the resin at elevated temperatures. A Netzsch simultaneous thermal analysis (STA) 449F3 instrument was used. In the instrument two crucibles (one containing the sample; the other an empty reference) are weighed during the experiment, and the mass loss as a function of temperature was recorded as the sample is subjected to a controlled temperature programme: equilibrium at 30 °C, ramp to 600 °C at 10 °C min^{-1}, dwell at 600 °C for 40 minutes. Mass loss was observed if a process occurred whereby a volatile component was released, *e.g.* thermal degradation [158]. This was used in Chapter 4 to assess the degradation of the four resin blends (resin blends **1-3** and industry benchmark), assessing

the resin degradation and determination of the char yield (*i.e.* the residual mass remaining after thermal degradation in an inert atmosphere at 800 °C).

TGA was also used determine the fibre volume fraction (v_f) of the carbon fibre composite laminates, Section 6.2.4.1. Carbon fibres can be oxidised when burn off is conducted in a furnace in air, which can affect the reliability of the results, using the TGA instrument allowed the burn off to be conducted under an inert nitrogen atmosphere thus preventing oxidation of the carbon surface. However, this technique is limited as small sample sizes (~10 mg) were analysed, so there may be larger variation in the local fibre fraction between samples cut from the laminate [159].

3.4.5. Thermal conductivity

Thermal conductivity can be measured using several techniques but can be grouped into two types: steady-state or transient. Steady-state methods measure the thermal properties of the sample by establishing a temperature difference that does not change with time, between the two surfaces from where heat is applied to the heat sink, *e.g.* absolute technique, Figure 22

In contrast, transient techniques such as pulsed-power technique, hot-wire method or laser flash analysis (LFA), measures time-dependent energy dissipation through the sample [160, 161]. LFA was used in this work.

LFA is a non-contact, non-destructive technique and thus offers an advantage over other methods which experience thermal resistance at the contact between the heat source and sample. The LFA method worked by using a laser to heat one side of the sample and a detector at opposite face measuring the time-dependent temperature rise. Schematic of LFA setup is shown in Figure 22. Equations 8 and 9 show the theory behind the technique, as given in both [161] and the ASTM standard E1461 [162].

$$\propto_D = \frac{0.13879h^2}{t_{1/2}} \tag{8}$$

where α_D is the thermal diffusivity; $t_{1/2}$ is the time taken for the sample to heat to one half of the maximum temperature on the rear surface; and h is the sample thickness.

The thermal conductivity, κ, was calculated using Equation 9.

$$\kappa = \propto_D \rho\, C_p \tag{9}$$

where p is the density and Cp is the specific heat capacity of the sample.
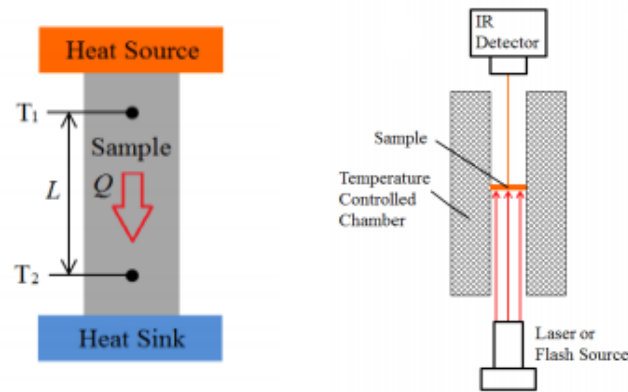
Figure 22: Schematic of two methods for testing thermal conductivity a) steady state absolute method b) transient LFA method. Reconstructed with permission from [160].

The main benefit associated with this method was that it was a fast test and used on small samples of cured resin. However, as density and specific heat capacity were calculated in separate experiments it may impart larger errors in the overall test [160].

3.4.6. Short beam shear (SBS) testing

To assess the interlaminar shear strength (ILSS) of both the GFRP and CFRP laminates manufactured in this work, short beam shear testing was conducted in accordance with ASTM standard D2344 [163].

The samples were loaded in three-point bending. To load the specimens a Shimadzu Autograph AGS-X test machine with 10 kN load cell was used, fitted with a three-point bend test fixture. The fixture had a 6 mm diameter loading nose and 3 mm diameter supports. The specimens were cut oversized using a diamond saw and polished to exact dimensions to meet the two following requirements:

- Specimen length = specimen thickness x 6.0
- Specimen width = thickness x 2.0

The test fixture span (distance between supports on three-point bend test fixture) was adjusted so that the span to measured thickness ratio was 4. Note that for the SBS testing of GFRP laminates the fixture used had a fixed span length of 26 mm. Therefore, the length was cut so there would enable the overhang over the supports of at least 2 mm. For CFRP laminate testing another fixture was sourced which enabled the span length to be adjusted.

47

The samples were positioned on the test fixture to be centrally loaded, with longitudinal axis perpendicular to the loading nose and supports. The machine was zeroed (both load and crosshead displacement) with the loading nose almost touching the sample. On the start of the test the crosshead was displaced at rate of 1 mm min^{-1}. The sample was loaded until at load drop of 30% was measured. The load *versus* crosshead displacement was recorded during the testing. The failure mode was also noted, in all tests interlaminar shear failure was observed.

3.4.7. Interfacial shear stress evaluation- microbond testing

This section will discuss the methods which can be used to assess the interfacial bonding between resins and fibre and explain the reasoning of why in this work microbond testing was selected for use. The test setup used in this work will be presented in Section 6.1.2, outlining how the test procedure was established during the project.

3.4.7.1. Methods to evaluate IFSS

To quantify the interfacial adhesion (interfacial shear strength, IFSS) between the resin and fibre, several methods have been discussed in literature, yet no standard currently exists. These methods include: fibre push-out [164, 165], single fibre fragmentation (SFF) [165, 166], fibre pull-out [167] and microbond [168–171]. These methods will be briefly outlined and critically reviewed. As the microbond test was used in this work, greater detail will be given of this method.

- *Fibre push-out/push-in*

A schematic of the debonding process by means of fibre push-out test is given in Figure 23. The push-out test works as an individual fibre on a thin composite laminate is loaded until the fibre/matrix interface fails and the fibre is pushed out. In contrast, in the push-in test, the fibre is loaded until interface fracture occurs, therefore there is no limit to sample thickness [164]. These tests are conducted using atomic force microscopy (AFM) fitted with a flat indenter, during the test the applied load and indenter tip displacement are monitored [165]. The methods were shown by Medina *et al.* [164] to display comparable results between both tests, indicating that choice of test method will depend on ease of sample preparation as the preparation of thin composite sheet required for push-out testing may be much more difficult.
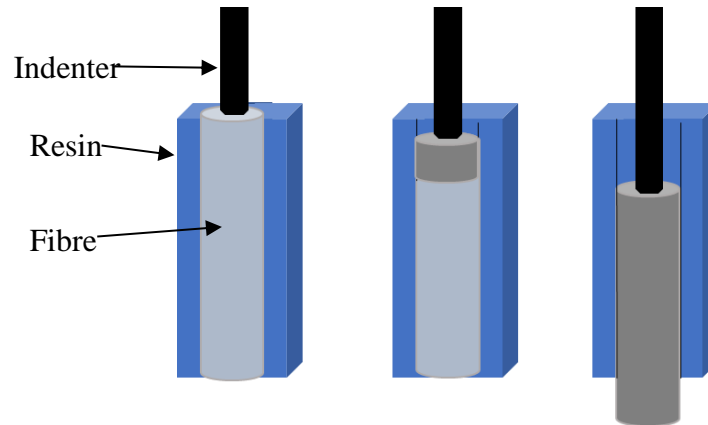
Figure 23: Micro-indentation process. Reconstructed from [165].

The one major advantage this method has over the other techniques that will be discussed, is that the IFSS is measured from an actual composite sample and not from a sample specifically prepared for the technique. Therefore the sample has representative local fibre volume fraction, thermal residual stresses and polymer crosslink density that would be seen in the final laminate, variations in these properties can affect the interfacial properties observed [164]. However, there are disadvantages of this test including: crushing of fibres which is commonly observed during testing, and the polishing of the sample surface prior to testing can induce defects [172], both of which affect the observed IFSS value.

- *Single fibre fragmentation test*

The single fibre fragmentation (SFF) test was developed by Kelly and Tyson [172]. In this method a single fibre is embedded in a dog-bone cured resin specimen. The specimen is loaded under tension, gradually the fibre breaks into increasingly smaller fragments at locations where the fibre strength is reached. When the fibre breaks the tensile stress reduces to zero. At higher axial strain, the number of fragments will increase until the fragment length becomes too short to transfer enough stress to the fibre to cause any further fibre breakage [173]. This process is shown in Figure 24. To observe the fragmentation process, the tensile test is conducted under an optical microscope with polarised light. This method assumes the fibre diameter and shear stress along the interface is constant. The IFSS (τ) is determined from Equation 10.

$$\tau = \frac{\sigma_f}{2}\left(\frac{d_f}{l_c}\right) \tag{10}$$

where d_f is fibre diameter, σ_f is the fibre strength at critical length and l_c is the critical fragment length of the fibre (calculated as four thirds of the average fragment length [166]).
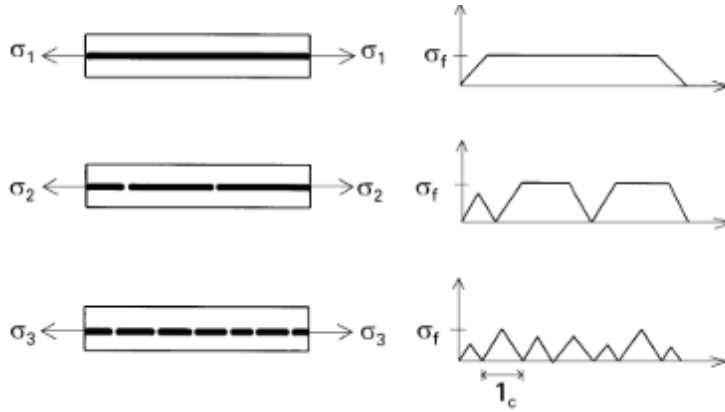
Figure 24: Single fibre fragmentation process. Taken with permission from [166].

Despite the fact this method has been used by many researchers to determine IFSS of composite systems, its main disadvantage is the difficulty of specimen preparation. The fibre must be held pre-strained within the moulds holding the fibre at the centre of the dog-bond specimen. The resin must be added in a manner that prevents the fibre being disturbed and to account for resin shrinkage further resin should be added post gelation. The specimens should be polished post-cure so that the resin is transparent, and the fibre is visible [173]. It is also vital that the matrix has a strain to failure three times higher than the fibre and it is sufficiently tough to resist fibre-fracture induced failure, this can be make using inherently brittle epoxy resins challenging to use [172]. The method assumes complete debonding occurs at the fibre/matrix interface and it is not possible to distinguish between the frictional shear strength and the interfacial bond strength [173]. Due to the complexity of sample preparation this method was not selected.

- *Fibre pull-out test*

Single fibre pull-out testing measures the force required to extract a single fibre from a thin resin disk, as shown in the schematic in Figure 25.

For this test to be successful the pull-out force must be lower than the fibre tensile strength. In practise this has led to difficulty in testing fine fibres (diameters <10 μm) as for the pull-out force to be smaller than tensile strength of fibre the embedment length must be very small (40-50 μm), which can be difficult to achieve.

To overcome this, Miller *et al.* [168] developed a modified fibre pull-out test known as the microbond test discussed in the following section.
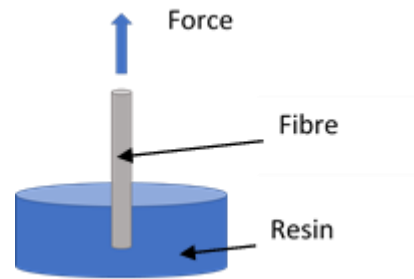
Figure 25: Schematic of pull out test.

- *Microbond test*

The microbond test method works by pulling a fibre with a cured resin droplet through a microvise gap. As the gap is too small to pull the droplet through, the interface de-bonds as the fibre is pulled through. The force required to pull the fibre through the microvise gap is recorded during the testing. A schematic of the microbond test procedure is shown in Figure 26.
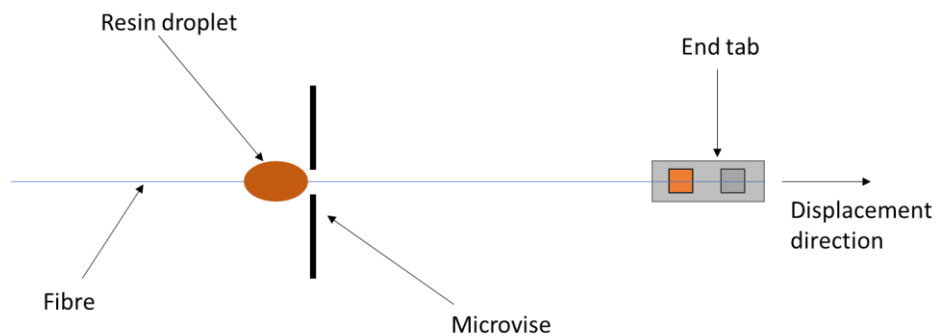
Figure 26: Schematic of microbond test procedure. Taken with permission from [174].

The droplet of the resin on the fibre is applied to the fibre and cured, on curing the droplets form concentrically around the fibre in an ellipsoid shape [169], as shown in Figure 27. The parameters are given as: d_f is the fibre diameter, θ is the contact angle of the meniscus to the fibre surface, l_e is the embedment length of the droplet along the

fibre, and d_m is the maximum droplet diameter, and are measured *via* optical microscopy prior to testing.
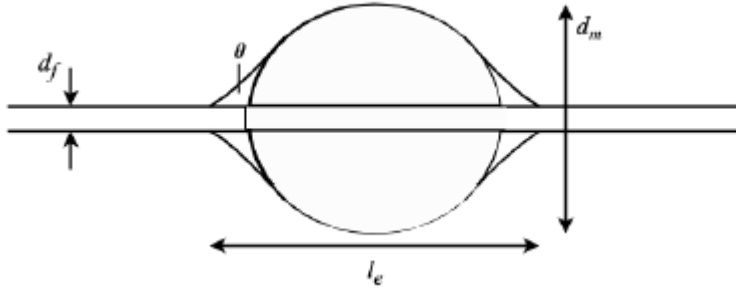
Figure 27: Schematic indicating the droplet parameters. Taken with permission from [174].

The IFSS (τ) is determined using the relationship described by Equation 11.

$$\tau = \frac{F}{\pi d_f l_e} \tag{11}$$

where, τ is the IFSS (MPa), F is the maximum force observed during the microbond test (debonding force) (N), d_f is the fibre diameter (mm) and l_e is the embedded length of the fibre (mm).The microbond test assumes that the shear stress distribution is uniform along the interface of the fibre and resin, which has been shown not to be true by finite element analysis [175] and Raman experiments [176, 177].

Microbond testing suffers from large data scatter [175], this is explained as the test setup has many setup parameters from droplet size, microvise gap, fibre diameter and test environment. As there are so many experimental parameters it is well known that inter-laboratory scatter is a problem and a round robin programme [178] suggested the need for standard procedures to be developed in order to reduce this variation which currently prevents quantitative results being directly compared between those obtained and literature values. It was shown that intra-laboratory scatter was minimal as testing configurations are kept constant and there was no notable difference between operators [178].

Many studies have evaluated that to obtain consistent reliable IFSS results in-house, test parameters should be kept constant. Miao *et al.* [179] conducted a series of finite element simulations and microbond tests, to assess how test parameters affect the IFSS, the tests showed that using thinner fibre, shorted embedment length and greater distance between

the fibre and microvise edge can increase the observed IFSS. Fukuda *et al.* [171] showed that the microvise gap and shape affect the IFSS, as both these conditions affect the stress distribution at the resin/fibre interface. The results from Fukuda's experiments suggests that a blunt-type microvise is better than sharp-type, as it does not create a stress concentration on the microdroplet which can cause a reduction in measured IFSS, shown in Figure 28.
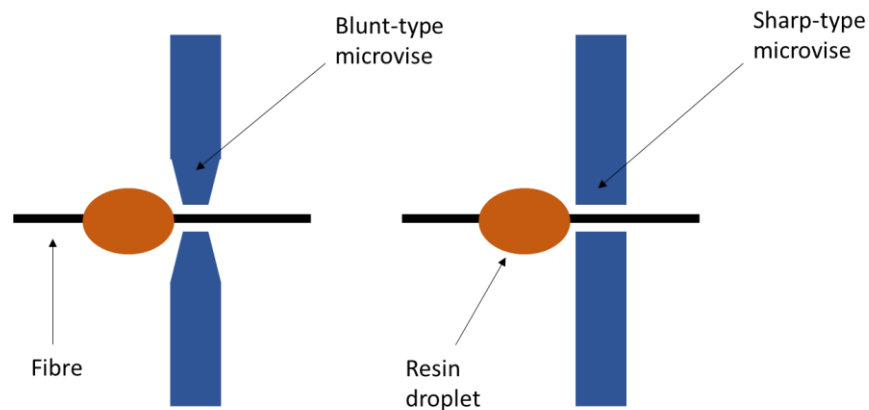
Figure 28: Schematic showing the effect of microvise edge shape on the microbond test.

Nishikawa *et al.* [180], studied the effect of the microvise gap on the interfacial debonding. It is shown that depending upon the location of the microvise with respect to the fibre surface different failure mechanisms can be observed. When the microvise edge lies close to the fibre surface the crack reached the fibre/matrix interface. However, if it was further from the fibre surface (twice the fibre diameter) then the interfacial crack occurred in the meniscus region, as shown in Figure 29. Miller *et al.* [168] identified that at the meniscus the resin coating is thinner and therefore can fail prior to debonding, leaving a cone of resin on the fibre surface, cohesive failure observed prior to interfacial debonding. This does not invalidate the result but does mean the true embedded length should be measured after testing. Miller *et al.* [181] suggests that the microvise should be placed close to the fibre surface, this is further iterated by Wu and Claypool [182], they also studied the effect of the microvise gap. Wu and Claypool [182], suggested that the microvise should lie as close to fibre diameter as possible. From Raman analysis of the microbond test performed by Day and Rodrigez [176], it showed that the microbond tests analysed conventionally showed lower average IFSS compared to the maximum shear stresses observed *via* Raman spectroscopy. This highlighted that the microvise gap is critical to the observed IFSS, if using conventional analysis then consistency of the

test parameters is more important to enable the value of IFSS determined to be used for comparative analysis.
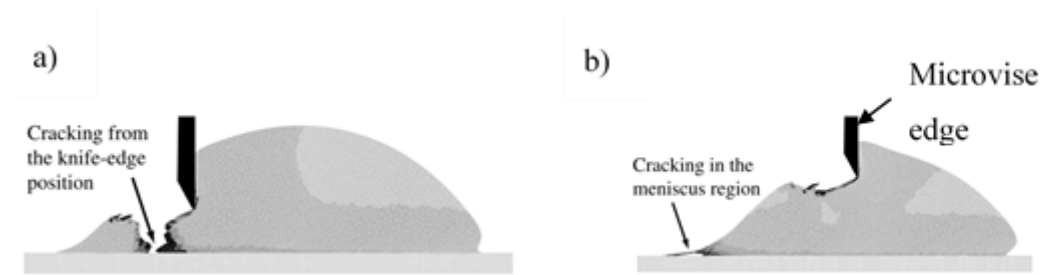
Figure 29: Effect of microvise distance from fibre surface effect on debonding mechanism: a) microvise gap only just wider than fibre diameter, b) microvise gap larger and therefore edges sit further away from fibre surface. Reconstructed with permission from [180].

The microbond test has been successfully used by many researchers to assess the many fibre-matrix combinations due to its simplicity and versatility [183], from assessing the IFSS of epoxy resins on natural flax fibres [184] to silkworm fibre (an especially thin and fragile fibre) [185]. Microbond techniques has been used extensively for evaluating IFSS of epoxy resins on glass [186] and carbon [187] fibre systems which will be explored in this work.

- *Validity of micromechanical testing*

In literature it is well documented that all these micromechanical tests have setbacks and although IFSS is measured by all, the values cannot be compared between tests. Zhou *et al.* [165] conducted SFF and fibre push-out tests on the same fibre/matrix system (E-glass/ epoxy resin), it was found that the although the absolute IFSS value determined in each case was substantially different (30 MPa SFF and 43 MPa for push-out testing, for unsized E-glass fibres), however the relative improvement between unsized and sized fibres (150%) was the same in both test methods.

As highlighted the methods suffer from large data scatter as there are so many variables not only in the testing but also in the fibre surface, therefore large sample sets are required. Round robin experiments using the same test and sample have shown that the same experiment conducted in different laboratories result in different IFSS values being obtained due to very slight difference in setup or operator use [178]. The IFSS of each

fibre/matrix system of interest should be examined using the same experimental setup and understanding of what is being measured and the limitations of the test selected should always be accounted for when drawing conclusions.

In this work the microbond technique was used selected as there was equipment within the department with this capability, and it was determined that the sample preparation could be done with relative ease. It was used in this study to rank order the IFSS performance of four resin blends on both glass and carbon fibre. The main objective was to establish if the anhydride-cured resins had a significant increase in the observed IFSS over the amine-cured industry benchmark and if so, was this translated to carbon fibre systems.

3.5.   Microscopy

In this work all optical micrographs were obtained using a Zeiss Axio upright light microscope, the images were captured with a camera (AxioCam). Scaling and measurements were attained using the AxioVision software. The optical microscope had several different magnification lenses, x5, x10 and x20, which were varied depending on the sample being observed.

Scanning electron microscopy (SEM) was also utilised in this work to visualise the microbond droplets after testing. Throughout the work a tabletop Hitachi SEM microscope TM3030 plus was used. This instrument enabled accelerating voltage of either 5, 10 or 15 kV to be used and either secondary or back scattered electrons to be used (or mix of both). The settings were varied during imaging to improve clarity of the image obtained. The photographic magnification achievable with this equipment was between x10 to approximately x100,000.

3.6.   Summary

This Chapter has outlined some of the underlying principles to methods used extensively in this work from resin characterization techniques to VARI used in laminate manufacturing, from ILSS and IFSS testing methods to the details of microscopes used. This chapter will be referred to in the experimental section of all subsequent chapters when used.

4 RESIN CHARACTERISATION

In this chapter the anhydride-cured epoxy resins will be evaluated against the amine-cured industry benchmark. Evaluating their suitability to WTB applications by assessing how well these resins perform in terms of their thermal, mechanical, and rheological properties. A preliminary study on the susceptibility of the anhydride-cured epoxies to moisture ingress is also presented, over the course of a WTBs lifetime it is exposed to harsh conditions and this study highlights that there is further work required to ensure the resin is protected to prevent moisture ingress which would affect the mechanical performance of the laminate.

Further to this as discussed in Chapter 2, there is some discussion around the mechanism of the cure reaction of anhydride-cured epoxies which are initiated by a tertiary amine. To probe this in this study, infrared spectroscopy was used to assess the chemical bonds present during the cure.

For the work to be presented in Chapter 7, some further material characterisation of resin blend **1** was required for the material inputs for the finite element model to predict the heat evolution during the cure. These properties included: density, thermal conductivity, and specific heat capacity.

The material presented herein has contributed to a journal submission published in Reactive and Functional Polymer Journal in 2019 [188].

4.1.   Experimental

The following section outlines the experimental procedures followed in this chapter to enable characterisation of the resin blends **1**, **2**, **3** and the industry benchmark, the formulations were presented in Section 3.1. The characterisation techniques are varied; allowing properties from viscosity (using rheology) to degradation (using thermogravimetric analysis) to be determined. Depending on the property being assessed either uncured or cured resin samples were used. The underlying principles behind some of these techniques are given in Chapter 3.

4.1.1. Characterisation techniques

4.1.1.1. Differential Scanning Calorimetry (DSC)

DSC experiments were performed using a TA DSC Q2000. Hermetically sealed Tzero aluminium pans were used, samples (both cured and uncured) of masses between 6-10 mg. Sealing was required to prevent evaporation or sublimation from the pan.

For dynamic DSC scans of uncured resins, samples were equilibrated at 30 °C and then heated to 250 °C at a heating rate of 10 °C min^{-1}, unless otherwise stated, with the sample cell kept under a constant nitrogen flow of 50 cm^3 min^{-1}.

Residual curing exotherms and T_g's for partially/fully cured resins were identified by modulated DSC (MDSC) thermograms. The temperature was swept from 25-250 °C with a ramp rate of 3 °C min^{-1}. The modulation period selected was 60 s with a modulation temperature amplitude of +/- 1 °C.

To measure specific heat capacity a Netzsch DSC 404 FI was used. The resins samples (8-10 mg) were weighed into aluminium crucibles and loaded into the DSC. The temperature was held isothermally at 40 °C for 20 minutes before ramping to 90 °C with ramp rate of 5 °C min^{-1}. The sample cell was kept under a constant nitrogen flow of 50 cm^3 min^{-1} throughout the experiment.

4.1.1.2. Rheology

A Discovery HR30 hybrid rheometer (TA Instruments) equipped with a parallel plate fixture was used to assess the uncured resins rheological behaviour. Disposable aluminium plates (25 mm in diameter with a gap of 0.3 mm) were used. To assess the time to gelation and the viscosity changes over the cure cycle, isothermal experiments were conducted at 75 °C. The chamber was equilibrated at 75 °C before the sample was loaded on to the plates. The strain frequency used was 1 Hz and an oscillation amplitude of 1.5% was selected as this fell well within the linear viscoelastic regime, which was determined from conducting a strain sweep test on the uncured resin system as shown in Section 3.4.3.

4.1.1.3. Dynamic Mechanical Analysis (DMA)

DMA experiments were performed in tensile mode with a Mettler Toledo DMA/STDA 1+. Cured resin samples of cuboidal geometry: thickness 0.76 (+/- 0.1) mm; width

3.3 (+/- 0.1) mm; and gauge length 10.5 mm were machined. Samples were equilibrated at -50 °C before ramping at 5 °C min^{-1} to 170 °C. The displacement amplitude was 5 µm and frequency 1 Hz, with force 1 N and static (pre-tension) force of 1.5 N.

4.1.1.4. Thermogravimetric Analysis (TGA)

A Netzsch simultaneous thermal analyser (STA) 449 F5 was used to obtain the TGA data for the cured resins samples. Samples (~18 mg) were weighed into aluminium crucibles, using an autosampler, the crucibles were loaded into the furnace and exposed to the following temperature profile: equilibrated for 10 minutes at 25 °C, ramped at 10 °C min^{-1} to 800 °C, before cooling to room temperature. All experiments were conducted under a constant flow of nitrogen (50 cm^3 min^{-1}).

4.1.1.5. Fourier Transform Infrared (FTIR) Spectroscopy

FTIR spectra were obtained over the wavenumbers 4000-600 cm^{-1} using a Perkin Elmer Spectrum 100 with universal attenuated total reflection (UATR) detector, with a resolution of 4 cm^{-1} and a scanning accumulation of 4 scans. This was done for both uncured and cured resins. As the contact of the crystal with the sample is much poorer for cured resin, the amplitude of the peaks cannot be accurately used to determine the degree of cure. The wavenumbers, however, can still be used to infer the bonds present in the sample and thus can be used to gain information regarding the reaction mechanism. Spectrum software was used for the collection and analysis of IR spectra.

A Specac heated Golden Gate ATR accessory was utilised to conduct an FTIR study during cure. The uncured resin sample was heated from 50 °C to 200 °C at 10 °C min^{-1}, every 20 °C the ramp was paused and the temperature maintained for 2 minutes to allow for the FTIR spectrum to be obtained in the same manner as described above. This enabled the cure mechanism to be probed as the chemical bonds present at stages as the resin cured were assessed.

4.1.1.6. Water uptake

Cured resin samples (2 mm x 10 mm x 35 mm) of both resin blend **1** and industry benchmark, were condition under vacuum at 40 °C for 48 hours to ensure they were completely dry. The samples were then individually submerged in distilled water (100 cm^3) in round bottom flasks housed in a reaction carousel heated mantle. The

temperature of the water was maintained at 50 °C during the experiment using the heated mantle. The samples were weighed at the start of the experiment and then periodically throughout the 42 days for which they were submerged. To do this the sample was removed from the round bottom flask using tweezers, the surface of the sample was wiped using a paper towel and the weight was recorded in grams to four decimal points. For each resin blend, six samples were tested. This test was conducted following the procedure outlined in the ASTM standard D570-water absorption of plastics (immersion at 50 °C) [189].

4.1.1.7. Cured resin density

The density, ρ, of the cured resin samples was determined using the immersion method (ASTM D792-13) and Mettler Toldeo density kit. This method utilised Archimedes' principle by weighing the sample in air and again when immersed in deionised water, the density is calculated using Equation 12.

$$\rho^{23C} = \frac{a}{(a-b)} \times 0.995 \tag{12}$$

where, a is the apparent mass of the sample in air; b is the apparent mass of sample completely submerged; ρ^{23C} is the density of the sample at 23 °C (deionised water temperature is monitored to ensure it is 23 °C); and the density of deionised water is 0.995 g cm^{-3}.

4.1.1.8. Rod dilatometry

A Netzsch 402 Dilatometer was used. Adhering to ASTM standard E228-11 [190], the linear thermal expansion of the cured resin sample was measured using a push-rod dilatometer. Samples (2.3 mm x 10 mm x 10 mm (+/- 0.1 mm)) were loaded into the instrument with the rod touching the sample. The sample cell was subsequently purged with nitrogen and then heated from 20 °C to 90 °C at 5 °C min^{-1}. The thermal expansion of the cured resin sample caused the rod to be displaced as it was heated, this displacement was recorded during the experiment.

4.1.1.9. Laser Flash Analysis (LFA)

A Netzsch NFA 427 instrument fitted with an indium antimony (InSb) detector and high temperature furnace was used to conduct the experiments. Cured resin samples (2.3 mm x 10 mm x 10 mm (+/- 0.1 mm)) were coated with a thin graphite layer. An
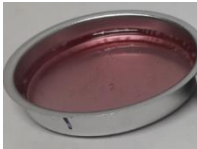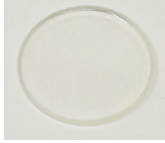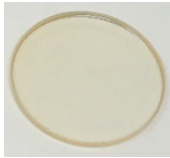
aerosol spray, Graphit 33, was used to deposit this thin graphite layer, this ensured that the samples were opaque and therefore only heat transfer was measured. The laser voltage was set to 450 V and pulse width to 0.5 ms. The three flashes were administered at three temperatures (50 °C, 75 °C, and 90 °C) for each sample. The sample cell was purged and kept under a nitrogen atmosphere with flow rate of 100 cm^3 min^{-1}.

4.2. Results and discussion

4.2.1. Visual appearance of anhydride-cured epoxy blends

The preparation of the three anhydride-cured epoxy resins blends resulted in obvious differences in the appearance of the blends observed both in their cured and uncured state. The most vibrantly coloured of these was blend **1,** in its uncured state it was bright pink, due to the charge transfer state formed from the mixing of the tertiary amine (Ancamine K54) and anhydride **C** (Table 3). On curing, a yellowish transparent plaque was formed. The three blends in their cured and uncured states can be observed in Table 6.

Table 6: Photographs of the anhydride-cured epoxy resin blends **1**, **2**, and **3** in their uncured and cured states. Images not to scale.

Blend	Uncured	Cured
1		
2		
3		

This was compared to the industry benchmark resin, which when uncured was blue (from the colour of the curing agent) and following cure, the plaque retained a blueish hue. It should be noted that the industry benchmark and resin blend **1** are much easier to infuse compared to resin blends **2** and **3** as the colour stands out and therefore the progress of the resin through the preform and bagging material can be observed. Patents show that some coloured resins (even those coloured by use of doping agents) not only allow for the flow front to be observed during the infusion processing, but also enable use of colorimetry which can be used as an analytical techniques to monitor the mix composition and evolution of cure [191, 192], thus allowing for better process control and potential to optimise the cure cycle.

4.2.2. Examining the processability of the blends

The intended application of these resins is in the production of wind turbine blades. And so, as discussed in Chapter 2, the principal manufacturing route used is vacuum assisted resin infusion (VARI). This process draws uncured resin though a preform of dry fabric. The infusion process is affected by several factors including: the resin viscosity (ideally below 500 cps (0.5 Pa.s)) [83], fabric permeability, and the infusion strategy chosen (number and location of resin inlets). Thus, understanding the relationship between the resin viscosity, gelation time, and polymerisation kinetics is necessary.

The evolution of the complex viscosity for each of the three anhydride-cured epoxies and for the industry benchmark was measured, and is shown in Figure 30. The resins' viscosity impacts the ability of the resin to infuse and fully wet out the fibre preform. Key data from these plots are given in Table 7. All resin blends assessed displayed similar initial viscosities (at isothermal cure temperature) prior to onset of cure. The time taken for the complex viscosity of each blend to exceed 1 Pa.s (and thus become no longer processable using infusion) was similar for the anhydride-cured resins, regardless of the anhydride structure. In contrast the amine-cured industry benchmark exceeded 1 Pa.s in a slightly shorter time frame (Table 7).
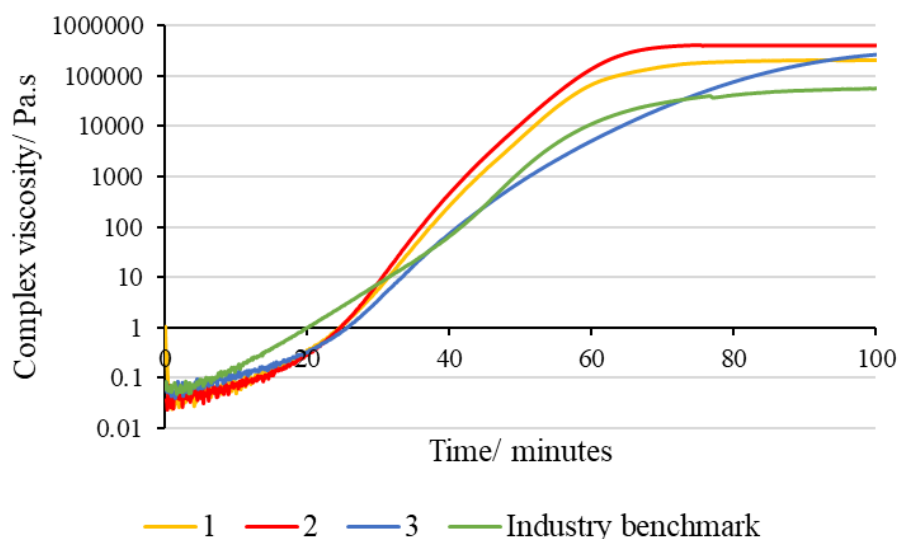
Figure 30: Complex viscosity data for each of the three anhydride-cured resin blends, **1**, **2**, and **3** at 75 °C and the complex viscosity data for the industry benchmark resin at 70 °C. These temperatures correspond to the respective cure temperature of the resins.

Table 7: Gelation behaviour measured at the cure temperature for each of the anhydride-cured epoxies (**1-3**) compared to the industry benchmark.

Resin blend	Initial complex viscosities (mPa.s)	Time at which the complex viscosity reaches 1 Pa.s (min)	Time to gelation (min)
1	44	27	56
2	36	26	63
3	58	26	73
Industry benchmark	50	21	51

The data shown in Figure 30 and Table 7 demonstrate that the anhydride structure does influence the rheological behaviour of the resin in the later stages of the reaction. Blends **1** and **2**, containing the more structurally similar anhydrides (varying only in the degree

of unsaturation), display very similar profiles of complex viscosity throughout the reaction. In contrast the influence of methyl-3,6-endomethylene-1,2,3,6-tetrahydrophthalic (MHAC-P, resin blend **3**) anhydride was more profound. This is highlighted in the difference in gel times, which was determined from the cross over in storage and loss moduli. The time to gelation is much longer for resin **3** taking some 73 minutes to gel, compared with 56 minutes for the blend **1** (containing 3- or 4-methyl-1,2,3,6-tetrahydrophthalic anhydride). This is hypothesised to be due to the MHAC-P anhydride having a more sterically hindered structure than the other anhydrides, leading to a delay in the reaction propagation, and therefore slowing the development of crosslinked network, thus reaching gelation later.

Comparing the anhydride-cured epoxies (resin blends **1** and **2**) to the industry benchmark there is little apparent difference between the resins. It should be noted that the industry benchmark resin has a different prescribed cure cycle, thus the rheological properties were measured at 70 °C and not 75 °C as had been used for studying the anhydride-cured epoxies. There is a slight increase in time to gelation of resin blend **1** compared to the industry benchmark, indicating it would have a marginally longer pot life and remain infusible (< 1 Pa.s) for a slightly longer time (*c.a.* 5 minutes), but this difference is marginal and not extremely significant. The key characteristic is that initial viscosity is lower. As infusion is conducted at lower temperature than cure (room temperature) this lower viscosity would enable the resin to percolate through the fibre much more easily and thus may result in better wet out of the preform.

4.2.3. Examining the thermal polymerisation of the blends

It was essential to characterise the thermal properties of the resin. DSC was used to determine the onset of reaction, exothermic peak (the temperature at which the exothermic rate is maximal) and the enthalpy of reaction for each anhydride-cured epoxy and the industry benchmark resin. This also assessed the effect of the anhydride structure upon these properties.

Figure 31 shows the DSC thermograms for each of the three blends, which were obtained from dynamic experiments conducted at 10 °C min^{-1}, with the hatched line representing one repeat run, to show the repeatability of the data.
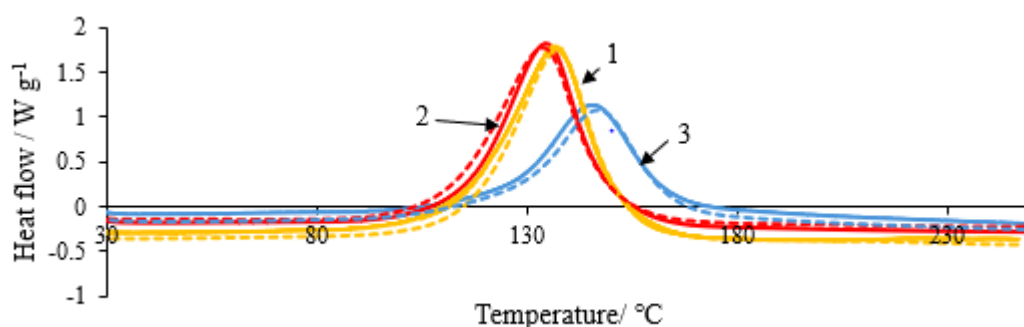
Figure 31: Thermal analysis of the uncured blends **1**, **2**, and **3** using DSC. Broken lines denote repeat analyses.

Table 8, shows the key data obtained for both uncured resin (Figure 31) and the cured resin (rescan of sample cured from dynamic DSC scan). Resin blends **1** and **2** yielded very similar temperatures for the onset of polymerisation and exothermic peak maxima, with the less reactive blend **3** showing a more delayed thermal event in a higher temperature regime (*e.g.* peak maximum some 10 °C higher) and lower reaction enthalpy, due to the resin have a more sterically hindered anhydride structure.

Table 8: DSC data for the uncured and cured (rescan of DSC sample) resin blends **1**, **2**, and **3**.

Resin blend	T_o (°C)	T_{max} (°C)	ΔH_c (J g^{-1})	ΔH_c (kJ mol^{-1})	$T_{g(ult)}$ (°C)
1	115	137	327	105	100
2	113	134	301	97	107
3	124	147	242	78	117

Key: T_o = Temperature of onset of polymerization, T_{max} = Peak exotherm temperature, ΔH_c = Reaction enthalpy. $T_{g(ult)}$ = Glass transition temperature determined from rescan DSC thermogram (fully cured).

Modulated DSC (MDSC) was used to obtained DSC thermograms of samples cured in the oven or those cured in the DSC by isothermal means. As the resin is exposed to lower temperature than in a dynamic scan, full cure is not obtained, it is vital to characterise the T_g and degree of cure obtained when the resin is cured using the prescribed cure cycle. A MDSC thermogram from resin blend **1** is given in Figure 32, which shows how the residual cure masks the phase transition associated with T_g, if just heat flow was recorded.
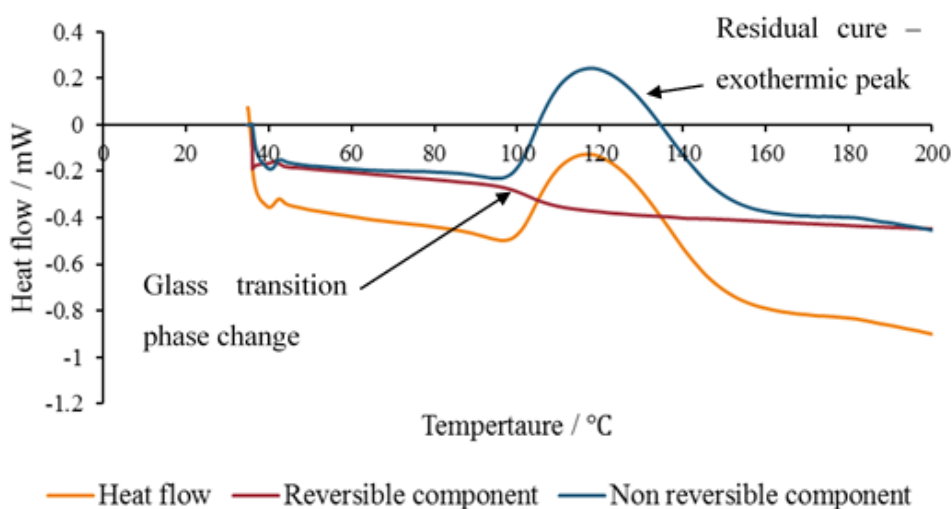
Figure 32: MDSC thermogram obtained for resin blend **1** cured in oven with prescribed cure cycle.

Using MDSC thermograms, the degree of cure (α) was calculated for all blends, which had been cured using the same prescribed oven cure cycle, using Equation 13. Pertinent data is also presented in Table 9.

$$\alpha = 1 - \frac{\Delta H_{pc}}{\Delta H_c} \tag{13}$$

where ΔH_c is the enthalpy of the cure reaction (see Table **88**), ΔH_{pc} is the residual cure (see Table **99**).

From the MDSC scans the residual cure for blends **1** and **2** are very comparable, at 89% and 88% respectively. Resin blend **3** has a lower degree of cure at 83%, this is again hypothesised to be due to the anhydride structure being more sterically hindered thus limiting the reaction proceeding further. There is a difference in the T_g measured from the rescan of the resin cured in the DSC ($T_{g(ult)}$), Table 8, which was ostensibly fully

cured, (since no measurable residual cure was observed) and the T_g observed from the MDSC, of a resin sample cured following the prescribed oven cure cycle. The lower T_g was recorded from the MDSC due to the lower conversion achieved with the prescribed oven cure cycle.

Table 9: MDSC data for the oven cured resin blends **1**, **2**, and **3**.

Blend	ΔH_{pc} (J g^{-1})	α	T_g (°C)
1	37	0.89	102
2	38	0.88	103
3	48	0.83	100

The key data for the industry benchmark resin are given in Table 10. Notably the exotherm occurs over a much wider temperature range with greater enthalpy of reaction compared to the anhydride-cured epoxies. Following MDSC analysis of an oven cured resin plaque, the T_g (78 °C) was observed to be lower that the T_g of the anhydride-cured resins (approximately 100 °C), thus showing its operational temperature would be some 20 °C lower than that of any of the anhydride-cured resin blends. The residual cure peak was not discernible on the MDSC thermogram (though the changing baseline may have masked this) and hence the degree of cure is assumed to be 1.

Table 10: DSC data for the industry benchmark.

T_o (°C)	T_{max} (°C)	ΔH_c (J g^{-1})	ΔH_{pc} (J g^{-1})	α	$T_{g\,(ult)}$ (°C)	T_g (°C)
40	120	377	-	~ 1	84	78

4.2.4. Thermomechanical analysis

Dynamic mechanical analysis (DMA) of cured resin samples was conducted. The storage modulus and loss factor as a function of temperature for the three resin blends and the industry benchmark are shown in Figure 33. It is apparent that the storage moduli, below T_g, are very similar for all resin blends, at 3.5 GPa (Figure 33a). Figure 33b shows the tan delta peaks for all resin blends, it can be seen that the T_g for all three anhydride-cured resins are similar (**1** - 97 °C, **2** - 98 °C, and **3** - 95°C, which corresponds

well with DSC findings in Table 9). As expected, the T_g is much lower for the industry benchmark with peak in tan delta at 69 °C, which again corresponds well to findings from DSC analysis (Table 10).
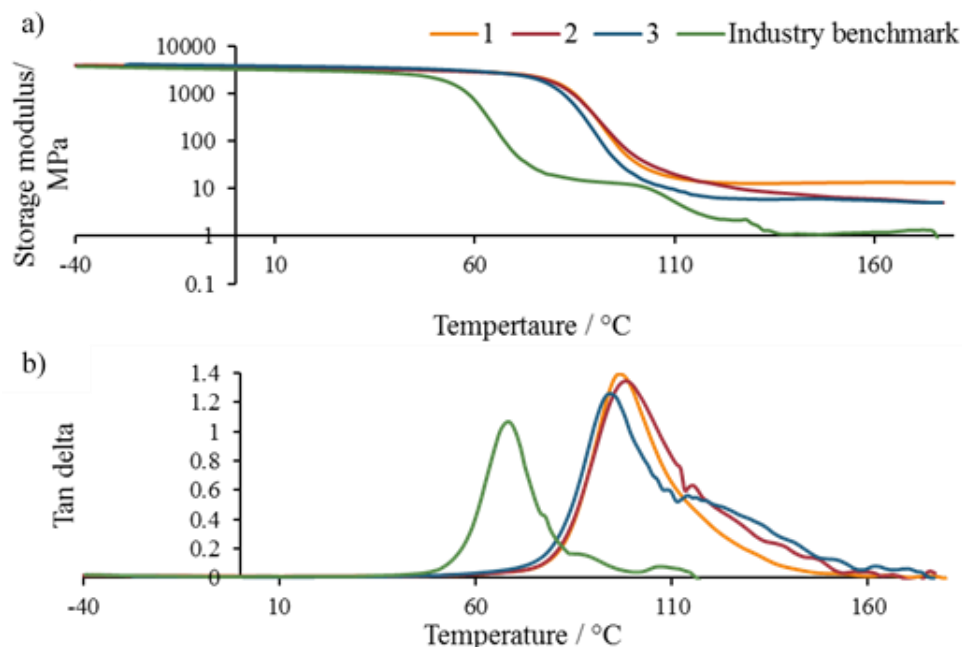
Figure 33: DMA data for cured resin blends **1**, **2**, and **3** and industry benchmark, (a) storage modulus and (b) tan delta.

From the DMA testing the difference in the three anhydride-cured resin blends was apparent from the magnitude of the rubbery modulus. Figure 33(a) shows resin blend **1** displayed the most rigid behaviour above T_g. Figure 33(b) shows that blends **2** and **3** (more so) exhibit a secondary peak at approximately 115 °C. This behaviour is likely due to the resin post-curing at these higher temperatures. From DSC analysis, Table 9, resin blends **2** and **3** were showed to achieve lower conversions using the prescribed cure cycle, with resin blend **3** showing the lowest conversion due to steric effects. The higher temperatures to which the sample were exposed to during DMA testing could enable post-cure and thus may explain the presence of this secondary peak in Figure 33(b).

For the industry benchmark, there is an interesting response as the drop in the rubber modulus was not continuous but stepped (Figure 33a). This could indicate that at elevated temperature there is some increase in the rigidity of the polymer as it is further cured and therefore a plateau in the storage modulus is initially observed before the

polymer undergoes its glass transition to its rubbery state. On the other hand, it may indicate the sample has slipped from the grips as it entered its rubbery phase and therefore data beyond this point is invalid.

The crosslink density of a lightly crosslinked material can be determined using Equation 14, [193, 194] from the statistical theory of rubber elasticity. Ishida and Allen [193], and Hamerton *et al.* [194], have successfully used this equation to assess qualitatively the crosslink density of polybenoxazines. They showed the equation worked well for homologous series, and therefore the same approach was adopted herein.

$$G' = \phi\nu RT_e \qquad (14)$$

where, G' is the storage modulus in the rubber region (T_e), ϕ is the front factor which is 1 for ideal rubbers, R is the gas constant (8.314 J K^{-1} mol^{-1}) and T_e is the absolute temperature ($T_g + 50$ °C) and ν is the crosslink density of the material.

Table 11: Crosslink densities for the anhydride-cured epoxy blends (**1-3**) and the industry benchmark resin.

Blend	T_g (K)	T_e (K)	G' at T_e (MPa)	ν (x10^{-3} mol cm^{-3})
1	370	420	11.9	3.42
2	371	421	8.0	2.30
3	368	418	8.2	2.37
Industry benchmark	341	391	13.0	4.00

Key: T_g = Glass transition temperature, T_e = Absolute temperature (T_g +50 °C), G' = Storage modulus at T_e and ν = Crosslink density.

Using Equation 14, the crosslink density of the cured epoxy resin blends was calculated, Table 11. Of the anhydride-cured systems, resin blend **1** presented the most highly crosslinked network, while resin blends **2** and **3** had comparably lower crosslink densities. The industry benchmark was shown to be more highly crosslinked, which corroborated the DSC data which showed it had a higher degree of cure. However, it should be noted that above the T_g the data from all samples suffers from noise which may be due to slippage of the samples in the DMA grips when the resin was in its rubbery

state. Thus, the reliability of the data is subjective, but it is good as a qualitative analysis to allow rank ordering of the samples.

4.2.5. Thermal stability of the cured resin blends

Thermogravimetric analysis (TGA) was employed to examine the thermal stability of the cured resin blends, Figure 34. Table 12 , presents the measured temperature for the mass loss, and residual char yield for each of the three anhydride-cured epoxy blends and the industry benchmark. The cured resins showed distinctly different degradation behaviour. Resin blends **1** and **2** displayed identical char yields, 5%, despite the disparity in the crosslink densities, shown in Table 11. But from onset, resin blend **1** displays slightly poorer thermal stability, as degradation occurred slightly quicker, over the temperature range (350 to 425 °C).

Most notable was the behaviour of cured resin blend **3**, which was observed to have a two-stage degradation process. The greatest mass loss had onset temperature at 372 °C, however a smaller mass loss was observed prior to this point with onset around 200 °C (Figure 34). It is proposed that at this temperature, a pericyclic retro-Diels-Alder reaction occurs in the norbornene moiety of anhydride **D**, leading to the elimination of a methylated cyclopentadiene species from the norbornene structure [188, 195–197] which would correspond to the initial mass loss, before the resin degrades in a similar manner to the other resin blends **1** and **2**. The higher char is assumed to be due to the different ratios of $sp^3 : sp^2$ carbons, as it is well known in literature that high aromaticity and cyclic structures lead to higher char yields [198].
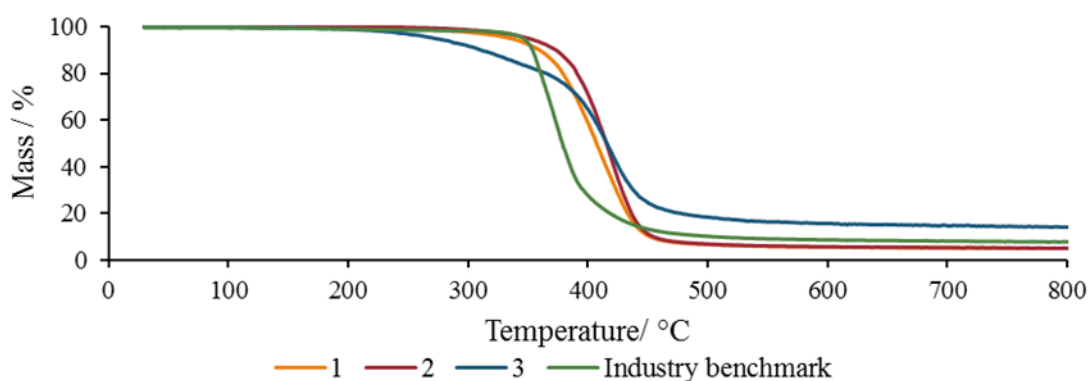
Figure 34: Thermogravimetric analysis data for the three cured resin blends **1**, **2**, **3** and the industry benchmark.

In contrast the industry benchmark seems to have comparable onset of degradation temperature with 5% mass loss at 347 °C. However, it loses mass at much greater rate than the anhydride resin blends, the temperature range over which it loses 40% mass is 26 °C compared to resin blend **1** which is 70 °C. Indicating the more complex, slower degradation process of the anhydride-cured epoxies may result in a more thermally stable resin compared to the industry benchmark.

Table 12: Degradation of resin blends **1**, **2**, **3** and the industry benchmark.

Blend	Temperature (°C) at which % mass lost				Y_c (%)
	$T_{5\%}$	$T_{10\%}$	$T_{20\%}$	$T_{40\%}$	
1	328	356	377	398	5
2	348	372	390	408	5
3	273	310	365	405	14
Industry benchmark	347	354	361	373	8

Key: $T_{x\%}$ = Temperature (°C) at which % mass is lost, Y_c = Char yield remaining at 800 °C.

4.2.6. Examination of network formation using FTIR spectroscopy for anhydride-cured epoxy resin blends.

As discussed in Chapter 2, there is some dispute in the literature as to the reaction mechanism of the tertiary amine-initiated anhydride-cured epoxies [39-42]. To probe the reaction mechanism FTIR spectroscopy was used to determine the bonds present in both uncured and cured resin samples. As the reaction mechanism is the same for all three blends, only resin blend **1** was assessed.

The FTIR spectra for resin blend **1** in both its uncured and cured state are given Figure 35. For uncured resin blends the main peaks of interest observed in the spectra were those at 1775 cm^{-1} and 915 cm^{-1}, which correspond to the bond frequencies of the carbonyl bond of the anhydride ring and the epoxide ring, respectively. In the cured resin spectra these bonds are either not present or significantly reduced and there is a new peak of interest at 1732 cm^{-1}. This peak corresponds to the alkanoate ester, formed

following the epoxide ring opening *via* the reaction of the epoxy with the anion formed from the pre-reaction of the anhydride and the tertiary amine.
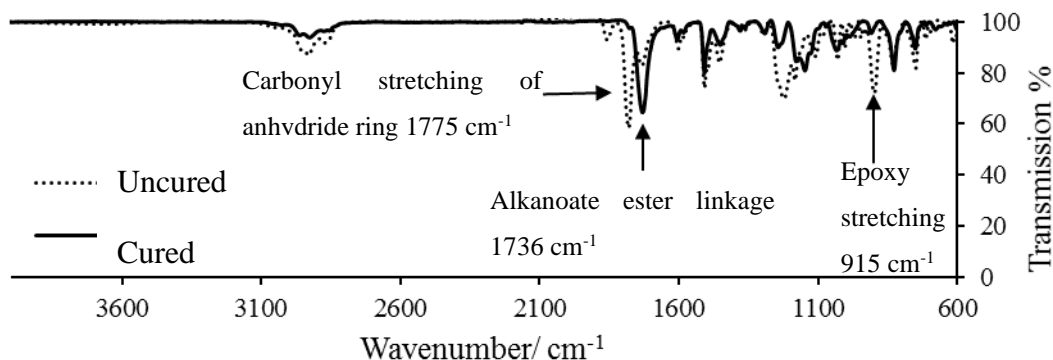
Figure 35: FTIR transmission spectra for resin blend **1.**

To further assess this and to observe how the reaction proceeds during cure, an FTIR study was conducted whereby the sample was cured *in situ* on the FTIR cell. The uncured resin was heated with ramp rate matching that of the dynamic DSC (10 °C min^{-1}) from 25 °C to 200 °C, with spectra taken at several temperature intervals throughout the ramp, shown in Figure 36. From Figure 36, it is clear than the peaks at 1775 cm^{-1} and 1736 cm^{-1} corresponding to the carbonyl of the anhydride ring and the alkanoate ester linkage respectively are important for monitoring the cure. Therefore this area of interest from Figure 36 is expanded and shown more clearly in Figure 37.
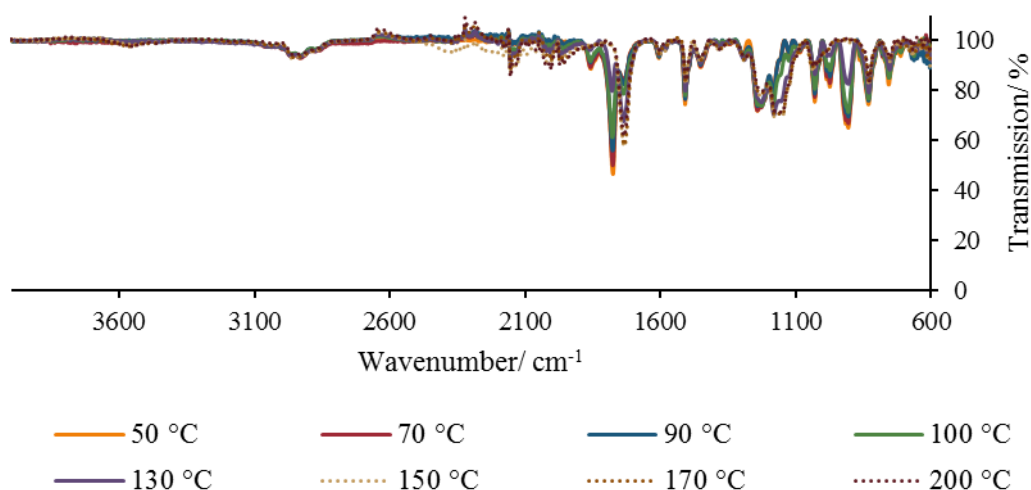
Figure 36: FTIR spectra for resin blend **1** through dynamic temperature ramp.
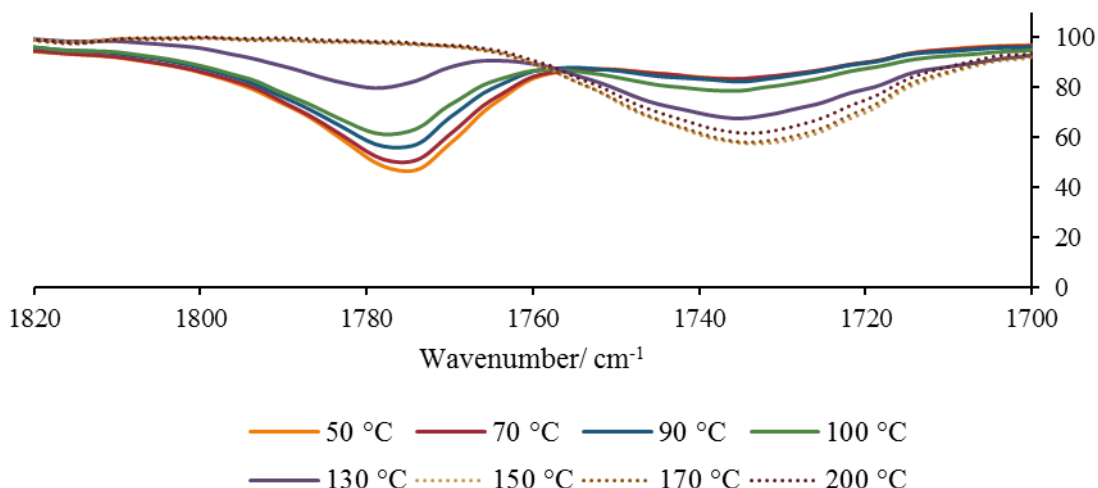
Figure 37: FTIR spectra at wavenumbers 1820-1700 cm^{-1} for resin blend **1** through a dynamic temperature ramp.

From Figure 37 it is clear that during cure, the peak at 1775 cm^{-1} decays at the same rate the peak at 1732 cm^{-1} emerges, which is in good agreement with Figure 35, and corresponds to the carbonyl bond of the anhydride ring and alkanoate ester respectively. This confirms the anhydride ring opens and the alkanoate ester is formed upon the reaction of the resulting anion and the epoxy ring. Owing to the complexity of the spectral data, principal component analysis (PCA) was used to identify the peaks which are changing during the cure. Principal components (PCs) can be used to help identify which peaks decay or emerge (PC1), shift (PC2) and the rate of change (PC3). In this data set there is little information gained from PC2 and PC3 in this experiment, as there was no shift in peaks or differences in rate of change to be observed. However, PC1 can be used to clearly show the changes in the peaks as bonds break and form during cure, shown in Figure 38. A positive peak in PC1 shows a trend that peak intensity decays through the cure. In contrast, a negative peak in PC1 indicates that during the cure the peak intensity increases, thus these bonds form during cure.
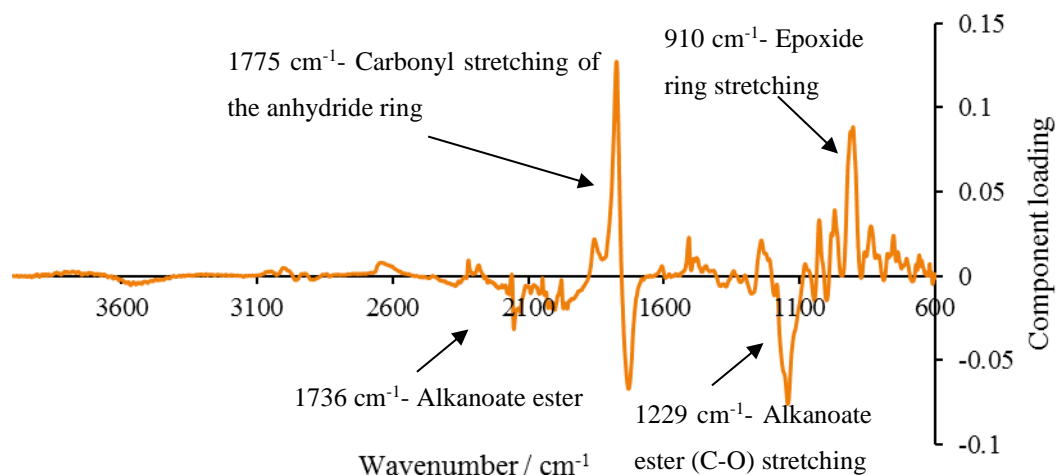
Figure 38: Principal Component 1 (PC1) for FTIR data obtained during dynamic cure of resin blend **1**.

The peaks in PC1 agree with the key peaks identified previously in Figures 35 and 36. These peaks (as previously highlighted) emphasise that the anhydride ring breaks as the alkanoate ester forms. In the spectrum, Figure 37, for the uncured resin (initial scan at 50 °C) there is a large peak at 1775 cm^{-1} and a very slight peak at 1736 cm^{-1}, thus showing large concentration of anhydride ring in the blend. In the cured (200 °C) spectra there is no observable peak at 1775 cm^{-1} but a prominent peak at 1736 cm^{-1} which shows the anhydride rings have been opened and reacted with the epoxide rings. The epoxy peak at 910 cm^{-1} also decays at similar rate to 1775 cm^{-1}, to form the alkanoate ester [199].

This FTIR study therefore agrees with the published mechanism by Fischer [39], whereby the reaction is initiated as the amine is pre-reacted with the anhydride, thus forming the anion which is then able to react with the highly-strained epoxide group, causing ring opening. The homopolymerisation reaction can then proceed leading to the development of the highly crosslinked, three-dimensional network during the cure cycle. The general reaction mechanism was shown in Figure 5, Section 2.4.

4.2.7. Moisture uptake

The uptake of moisture can degrade resins in several ways including plasticisation, crazing, hydrolysis, and swelling. In plasticisation the water molecules interact with the polar groups of the resin and can supress the T_g, unlike the other methods, plasticisation

is considered reversible [200–202]. Crazing leads to the formation of voids within the polymer network, and hydrolysis causes the scission of polymer chains. All these mechanisms ultimately degrade the polymer and reduce the mechanical performance of the composite laminate [203–207]. Epoxy polymers are hydrophilic and therefore are susceptible to moisture uptake. Depending on the nature of the polymer blend the equilibrium moisture uptake can be in the range 1-7% [208]. Wind turbine blades are exposed to harsh conditions from rain and humidity and they are expected to have a long service life of 20-30 years [209]. Therefore, minimising the potential for water ingress, which can lead to hydrolysis and polymer degradation is essential to maximise service life.

Acid anhydrides are notoriously affected by moisture in their compound states as water attacks the anhydride ring to form carboxylic acids [210]. Careful storage in sealed containers is required to prevent the anhydride reacting with moisture in the air. To assess if these anhydride-cured epoxy resins developed by HCCL are more susceptible to moisture ingress than an amine-cured industry benchmark a small study has been conducted, of the anhydride-cured epoxies only one was testes, resin blend **1**, as it was hypothesised that the other anhydride resins (resin blends **2** and **3**) would display similar response, if not be more susceptible due to their lower degree of conversion.

Moisture uptake is usually studied by placing samples in temperature and humidity-controlled chambers for extended periods of time (6 months or more). Due to time constraints, the method outlined in Section 4.1.1.6 was used. The percentage mass increase normalised by sample thickness over time for resin blend **1** and industry benchmark, are shown in Figure 39.

The average percentage mass increase for resin blend **1** was 2.6% (standard deviation (SD) 2.4) compared to 0.9% (SD 0.08). This suggests that this anhydride-cured resin system was more susceptible to moisture uptake than its amine-cured counterpart.

It should be noted that the plots of water uptake are not straight during the initial phase of water absorption. This suggests that Fickean behaviour was not being followed, this may be due to a non-uniform initial water concentration. Although drying the samples for 48 hours is standard it may not have been enough time to remove all the water. If this testing were to be repeated drying for a longer period whereby the weight was

monitored to ensure the sample was completely dry prior to submersion would be recommended.
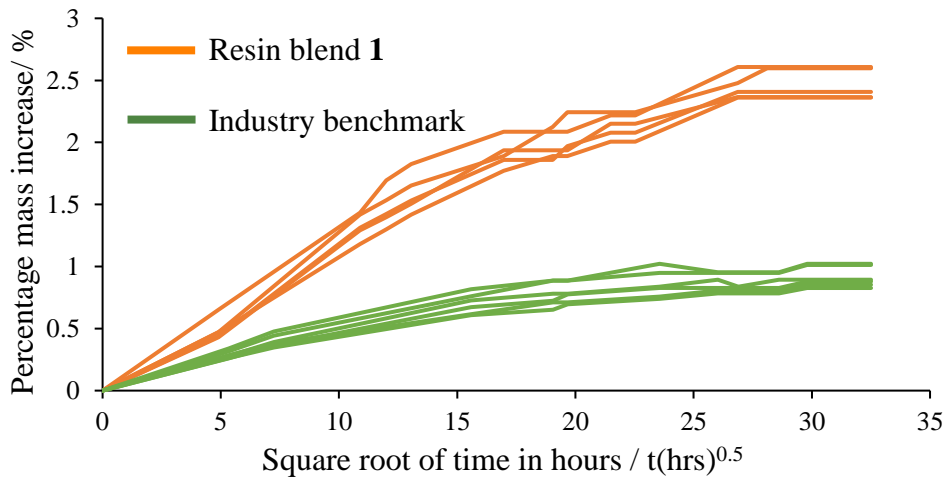
Figure 39: Percentage mass increase of resin blend **1** and industry benchmark over a 42 day period as samples are submerged in 50 °C.

In 1981 Wright [203] studied the effect of moisture on epoxy CFRP laminates and concluded, that for every 1% by weight of moisture absorbed the T_g would decrease by 20 °C as a rough estimate. To assess the impact of the moisture absorbed on the T_g of the anhydride-cured resin system, a MDSC thermogram was obtained for the resin sample following 42 days submerged in water, shown in Figure 40. It showed the T_g of the resin was 82 °C, which was 20 °C lower than had been observed for the samples after cure (previously shown in Table 9).
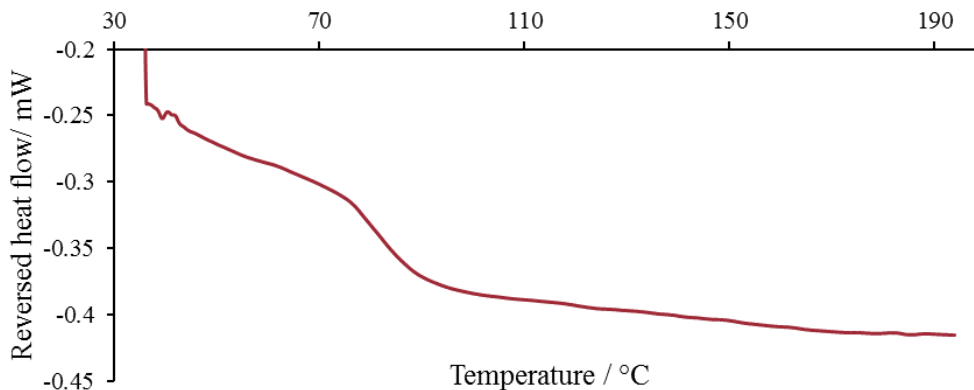
Figure 40: Reversed heat flow from MDSC thermogram of resin blend **1** after submersion in 50 °C for 42 days.

Although no further assessment of the reduction in mechanical performance due to moisture absorption was conducted, this is discussed in literature [203–207].

As this study shows that the anhydride-cured epoxies are more susceptible than the industry benchmark, methods to reduce the susceptibility of the resin to moisture ingress could be studied in further work.

Hamerton *et al.* [211] showed that polyhedral oligomeric silsesquioxane (POSS) nanocomposites dramatically reduced water uptake in anhydride-cured epoxy resins. It was shown that incorporating 1 wt% POSS reduced the moisture uptake by 25% at 75% relative humidity and as a result the T_g only decreased by 10 °C, compared to the neat resin which dropped by 31 °C following the same exposure.

Further to this, a study by Glaskova e*t al.* [212], has shown that nanoclays could offer improved resistance to moisture degradation. It is hypothesised that these nanoclays act as barriers preventing the transport of water molecules through the matrix due to the nanoclays having high shape anisotropy, and having an exfoliated surface effectively lengthening the path of these diffusing molecules. It was shown that a 1% addition of an octadecylamine-modified montmorillonite based nanoclay reduced the effects of moisture absorption for the epoxy resin. Kini *et al*. [213], have also studied the effect of montmorillonite nanoclays as a means to mitigate the effect of hydrothermal aging on epoxy resins, in this work samples were soaked in cold water or boiling water for different periods of time. The addition of 2 wt% nanoclay helped to retain the mechanical performance of the resin over the unmodified resin. For example, for the unmodified epoxy sample the flexural strength reduced by 24% after soaking in cold water. The addition of 2 wt% nanoclay to the epoxy reduced the impact of moisture absorption as flexural strength only decreased by 14%.

However, the addition of additives may not be desirable as this may affect the viscosity of the resin and may affect its processability for the intended manufacturing process. Methods to prevent moisture ingress more typically used by the WTB industry involve the use of coatings, which form a barrier to the environment. There is some work in this field to develop coating which are more hydrophobic than those currently used which offer an enhanced ability to prevent moisture ingress. For example Gou *et al.* [214] showed that POSS-g-CNF (POSS grafted onto a carbon nanofibre) formed a paper which could subsequently be incorporated to the laminate as the paper is laid up on the preform stack which is subsequently infused *via* resin transfer moulding (RTM). The

POSS-CNF nano-paper demonstrated stable hydrophobicity even after exposure to a high-humidity environment for several weeks.

4.2.8. Thermal conductivity

The thermal conductivity, thermal diffusivity, and specific heat capacity collectively define the ability of the material to transfer heat. The thermal conductivity was determined for resin blend **1** and the industry benchmark. The other two anhydride cured epoxies were not assessed as it was deemed that these would likely be comparable to resin blend **1**.

The thermal conductivity, κ, was determined using Equation 15:

$$\kappa = \alpha_D \; \rho \; C_p \tag{15}$$

where α_D is thermal diffusivity, ρ is density, and C_p is the specific heat capacity of the material.

4.2.8.1. Density

The cured densities for resin blend **1** and the industry benchmark were determined using the method outlined in Section 3.4.5. For resin blend **1** and the industry benchmark this was calculated to be 1.214 g cm^{-3} and 1.14 g cm^{-3} respectively. The density of GFRP laminate infused with resin blend **1** also determined to be 2.15 g cm^{-3}.

4.2.8.2. Specific heat capacity

Specific heat capacity (C_p) is the amount of heat energy required by the sample to raise its temperature 1°C per unit of mass. C_p was determined using DSC analysis as described in Section 4.1.1.1. The DSC thermogram for resin blend **1** and the industry benchmark is given in Figure 41 and shows the C_p for the anhydride-cured epoxy is lower than that of the industry benchmark and goes through less variation over the studied temperature range, 40-90 °C. This again is due to the lower T_g of the industry benchmark which results in the transition seen at 70 °C. It can be seen in the resin blend **1** trace, that the increase in specific heat capacity increases at 85 °C which corresponds to the onset of its T_g. The C_p below its T_g is constant and the values for both resin systems are comparable at 60 °C at 0.98 J g^{-1} K^{-1}.
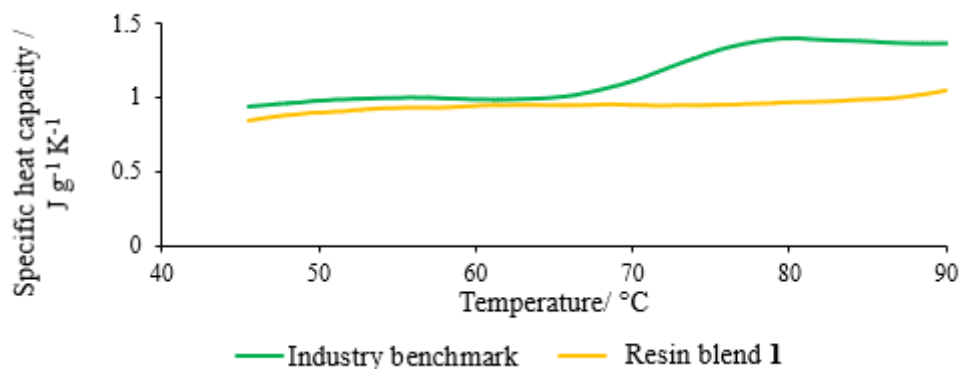
Figure 41: Specific heat capacity variation with temperature for both resin blend **1** and the industry benchmark.

4.2.8.3. Linear thermal expansion

A rod dilatometer, as described in Section 3.4.5, was used to measure the linear thermal expansion of the resin (CTE) and the data from both resins are given in Figure 42. It was observed that the industry benchmark undergoes the following transitions:

- As the sample is heated to 40 °C a β-transition is observed (this corresponds to movement of localised groups within the network before the T_g is reached [215]).

- Between 40 °C and 70 °C a linear response is observed. As it is heated to 85 °c a more rapid expansion is observed.

- At 85 °C there is a dip in the linear expansion as the resin enters its rubbery phase.

In contrast, resin blend **1** has a much more linear response, as its T_g is slightly higher (102 °C) and so no onset of T_g is discernible in this temperature range. Comparing the two resins, the anhydride-cured epoxy resin (resin blend **1**) showed less expansion over the same temperature range as the amine-cured resin. This may be due to its inherently more brittle and rigid structure as shown by DMA, likely due to higher degree of cure and hydrogen bonding within the polymer network. The linear thermal expansion for resin blend **1** and the industry benchmark are 60 x 10^{-6} K^{-1} and 100 x 10^{-6} K^{-1} respectively. This compares with a literature value of DGEBA epoxy resin cured with

hexahydrophthalic anhydride (HHPA) hardener which had a reported linear expansion coefficient of 70×10^{-6} K^{-1} [216].
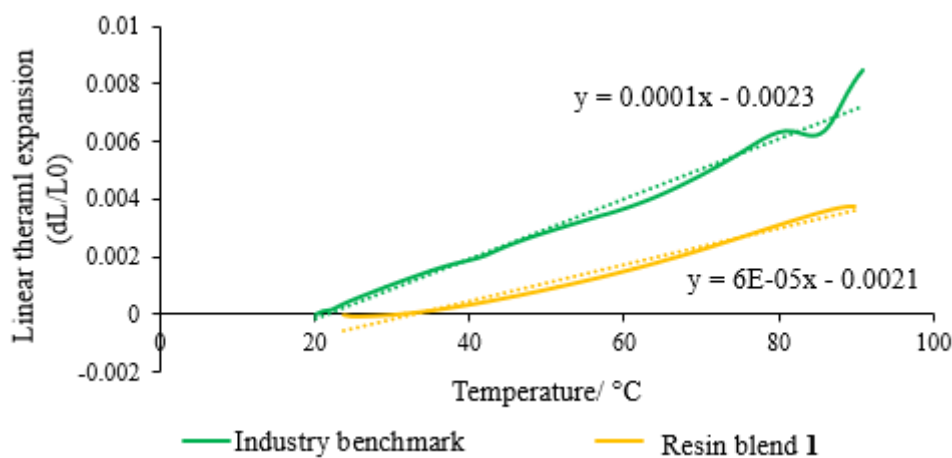
Figure 42: Linear thermal expansion for resin blend **1** and the industry benchmark as measured using rod dilatometry.

4.2.8.4. Thermal diffusivity

Thermal diffusivity of a material is a measure of the speed of heat transfer *via* conduction through the sample. In this work laser flash analysis (LFA) was used to determine this for the two resin systems and this method is described in Section 3.4.5 and the experimental setup in Section 4.1.1.9.

The average thermal diffusivity data for the two resins at three set temperatures are given in Table 13.

Table 13: Thermal diffusivity for resin blend **1** and the industry benchmark.

Blend	Thermal diffusivity (mm^2 s^{-1})		
	50 °C	75 °C	90 °C
1	0.11 (0.01)	0.10 (0.00)	0.10 (0.01)
Industry benchmark	0.13 (0.01)	0.11 (0.01)	0.10 (0.01)

N.B. number in brackets = standard deviation.

4.2.8.5. Thermal conductivity

The data obtained for cured resin density, C_p and CTE were used to calculate the thermal conductivity using Equation 9 (as described in Section 3.4.5) at each of the three temperatures where thermal diffusivity was measured in the LFA experiment. The thermal conductivity for both resin blend **1** and the industry benchmark are given in Table 14.

Table 14: Thermal conductivity for resin blend **1** and the industry benchmark.

Blend	Thermal conductivity (W m^{-1} K^{-1})		
	50 °C	75 °C	90 °C
1	0.12 (0.01)	0.12 (0.00)	0.11 (0.02)
Industry benchmark	0.14 (0.01)	0.16 (0.01)	0.14 (0.01)

N.B. number in brackets = standard deviation.

4.3.   Summary

The cure of DGEBA, a difunctional epoxy resin, has been studied in the presence of three carboxylic anhydrides, with different cycloaliphatic moieties. Data from rheological and thermal analyses confirm that all three anhydrides form suitable blends for infusion, each displaying low viscosity and favourable cure behaviour at moderate temperatures. Anhydrides with similar chemical structures (*i.e.* **1** and **2**) yield cured blends with similar dynamic mechanical properties (*i.e.* modulus and T_g) and thermal stability. The inclusion of norbornene moiety in blend **3** raised the viscosity of the blend significantly and led to a slower reaction and a marginally lower conversion, despite displaying a similar activation energy and collision factor to the other blends. The resulting cured polymer blend for this anhydride displayed lower thermal stability (postulated as being due to a retro-Diels-Alder mechanism), but a higher char yield when compared to the other cured blends.

The resin blends have been compared to a widely used commercial wind turbine blade resin. The properties of the anhydride resins compare well to the amine-cured industry

benchmark, showing favourable thermomechanical properties such as higher T_g, increased thermal stability and a lower enthalpy of reaction.

As resin blend **1** was used to evaluate vascular curing as a manufacturing method (Chapter 7) therefore further characterisation of the thermal properties such as thermal conductivity, specific heat capacity and density was required in order to have material inputs for the computer simulation of cure.

The next chapter (Chapter 5) will look to examine the cure kinetics, using Kissinger and Ozawa kinetics as simple methods to study differences between the four resin blends (**1**-**3** and the industry benchmark), assessing the effect of anhydride structure and resin chemistry upon this. As resin blend **1** is used for vascular curing a more detailed analysis of the cure kinetics was required and this will also be presented in the following chapter.

5 RESIN CURE KINETICS

DSC analysis is the most common method employed to assess the reaction kinetics, which can be conducted in either non-isothermal or isothermal modes.

In this chapter, non-isothermal DSC methods will first be used to assess the effect of the anhydride structure upon the kinetic parameters and compare this to the parameters observed for the industry benchmark. Kissinger and Ozawa models are used to derive the activation energy and pre-exponential factor for each reaction. They have been shown to be effective models for both n-th order and autocatalytic reactions, and have been used in literature to characterise both amine-cured [217] and anhydride-cured epoxy resin [218].

These models are somewhat limited as they reduce the complexity of the cure reaction (Chapter 4) to a single step by ignoring the reaction order therefore calculated parameters can only be considered approximate values [42].

As resin blend **1** was used for assessing the vascular cure manufacturing method further characterisation was required, a cure kinetic model was needed to enable the extent of the chemical reaction to be tracked during a given cure cycle [219]. Isothermal DSC methods were used to determine a cure kinetic model which was most appropriate to be used in the vascular cure work.

The non-isothermal cure kinetics for the anhydride-cured epoxies presented herein has contributed to a journal submission published in Reactive and Functional Polymer Journal in 2019 [188]. The cure kinetic model fitting for resin blend **1** contributed to work presented in the conference proceedings at Thermosetting resins conference, 2018 [220].

5.1. Experimental

5.1.1. Resin

Resin blends **1**-**3** and the industry benchmark were formulated with mixing ratios and methods outlined in Section 3.

5.1.2. Differential Scanning Calorimetry

DSC experiments were performed using a TA DSC Q2000. Hermetically sealed Tzero aluminium pans were used, with sample masses between 6-10 mg of uncured and cured samples. Sealing is required to prevent evaporation or sublimation from the pan. Sample cell was kept under a constant nitrogen flow of 50 $cm^3\,min^{-1}$.

For non-isothermal, dynamic DSC scans of uncured resins the samples were equilibrated at 30 °C and then heated to 250 °C at a desired heating rate; either 3, 5, 10, 15 or 20 °C min^{-1}.

For isothermal DSC scans of uncured resin, the DSC was equilibrated at the desired temperature for 5 minutes before the sample was loaded into the furnace. The isothermal temperature was maintained for a set time (100 minutes). The isothermal temperatures used were 100, 110, 115 and 120 °C, these were selected as temperatures that are within the exotherm peak of the dynamic DSC conducted using 10 °C min^{-1} ramp rate, between the onset and peak temperature.

It should be noted that in this chapter in order to calculate the kinetic parameters SI units were needed to be used therefore all temperatures used are used in Kelvin (K) not degrees Celsius (°C), as used thus far, to convert between units the Equation 16 was used.

$$T\ (K) = T(°C) + 273.15 \tag{16}$$

5.2. Non-isothermal reaction kinetics

Figure 43 presents the DSC thermograms for each anhydride-cured epoxy resin blends (resin blends **1**-**3**) from the dynamic DSC tests conducted at several heating rates as described in Section 5.1.2.

As expected, the effect of the increase in heating rate serves to shift the value of peak exotherm temperature (T_{max}) to a higher temperature regime in all three blends.

Assuming first order reaction kinetics, the Kissinger and Ozawa methods [42, 221, 222] can be used to yield a preliminary assessment of the resin kinetics in each of the three blends. Using the Kissinger method, Equation 17, the activation energy (E_a), and the pre-exponential factor (A), were determined for each of the three blends.

$$ln\left(\frac{\beta}{T_{max}^2}\right) = ln\left(\frac{AR}{E_a}\right) - \frac{E_a}{RT} \tag{17}$$

where, β is the heating rate (K min^{-1}); T_{max} is the exothermic peak maximum (K); E_a is the activation energy (kJ mol^{-1}), which is the energy barrier the reaction must overcome for the reaction to proceed; A is the pre-exponential factor (s^{-1}), which is interpreted as the probability that a molecule will have energy E_a and participate in the reaction; R is the gas constant (8.314 J K^{-1} mol^{-1}), and T is the temperature at which the reaction is occurring (K).
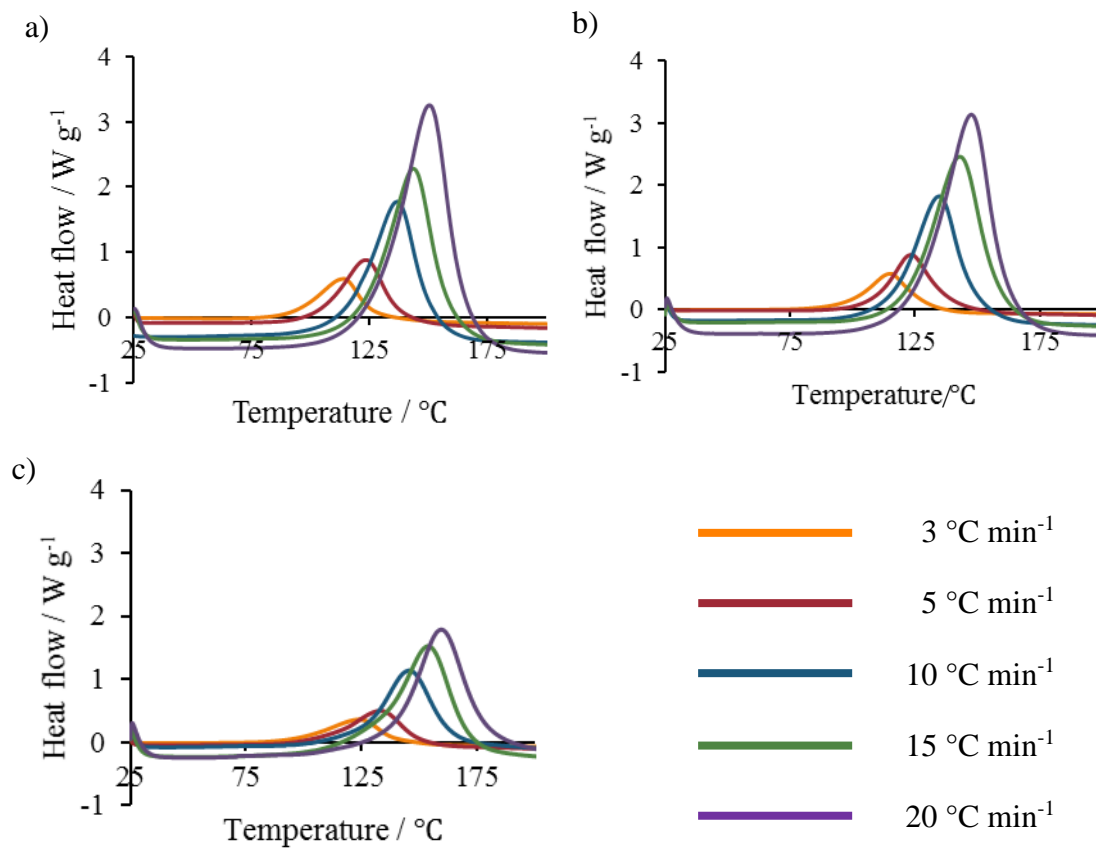
Figure 43: DSC thermograms of resin blends **1** (a), **2** (b), and **3** (c) at several different heating rates: 3, 5, 10, 15, 20 °C min^{-1}.

The activation energy (E_a) and pre-exponential factor (A) were determined from the gradient and y-intercept respectively from the plot of $\ln\beta = (T_{max})^2$ *versus* $1/T_{max}$, Figure 44.

A complementary method to Kissinger, was proposed by Ozawa, this considers the effect of heating rate and uses the inverse of the exothermic peak maximum and the logarithm of the heating rate, allowing the E_a to be determined using Equation 18.

$$ln\, \beta = \text{const} - 1.052\, \frac{E_a/R}{T_{max}} \tag{18}$$

Figure 44 (a-c), shows the plots of the kinetic data obtained using both the Kissinger and Ozawa methods, for the blends **1**, **2** and **3**, and by using Equations 17 and 18, the values of E_a were determined from the gradients of the lines. It can be seen in both cases (Kissinger and Ozawa) that the R^2 value is greater than 0.99 suggesting a perfect fit for the equation of the line and that both models are valid. The Kissinger method also enables the pre-exponential factor (A) to be determined, and therefore the rate constant (k) for the reaction can be calculated, using the Arrhenius equation as given in Equation 19.

$$k = A\, e^{\left(\frac{-E_a}{RT}\right)} \tag{19}$$

where, k is the rate constant (s^{-1}) and T is the temperature of the reaction (348 K or 75 °C, selected as this was the cure temperature used throughout the study). The values calculated are given in Table 15.

Table 15: Kissinger and Ozawa kinetic analysis for the three anhydride-cured resin blends (**1**-**3**).

Blend	Ozawa method, E_a (kJ mol^{-1})	Kissinger method, E_a (kJ mol^{-1})	Pre-exponential factor, A (s^{-1})	Rate constant, k (10^{-2}) at 348 K (s^{-1})
1	72.2	69.2	3.3×10^8	1.40
2	78.1	75.4	2.5×10^9	1.20
3	75.2	72.2	4.6×10^8	0.68

Interestingly the reduced reactivity of blend **3** is shown by the lowest first order rate constant (6.8×10^{-3} s^{-1} at 348 K), but this is not reflected in the activation energy, which is found to be highest for blend **2**. Similarly, of the three blends, **1** displays the fewest collisions ($A = 3.3 \times 10^8$ s^{-1}), so the reason for the disparity is more complex [223].
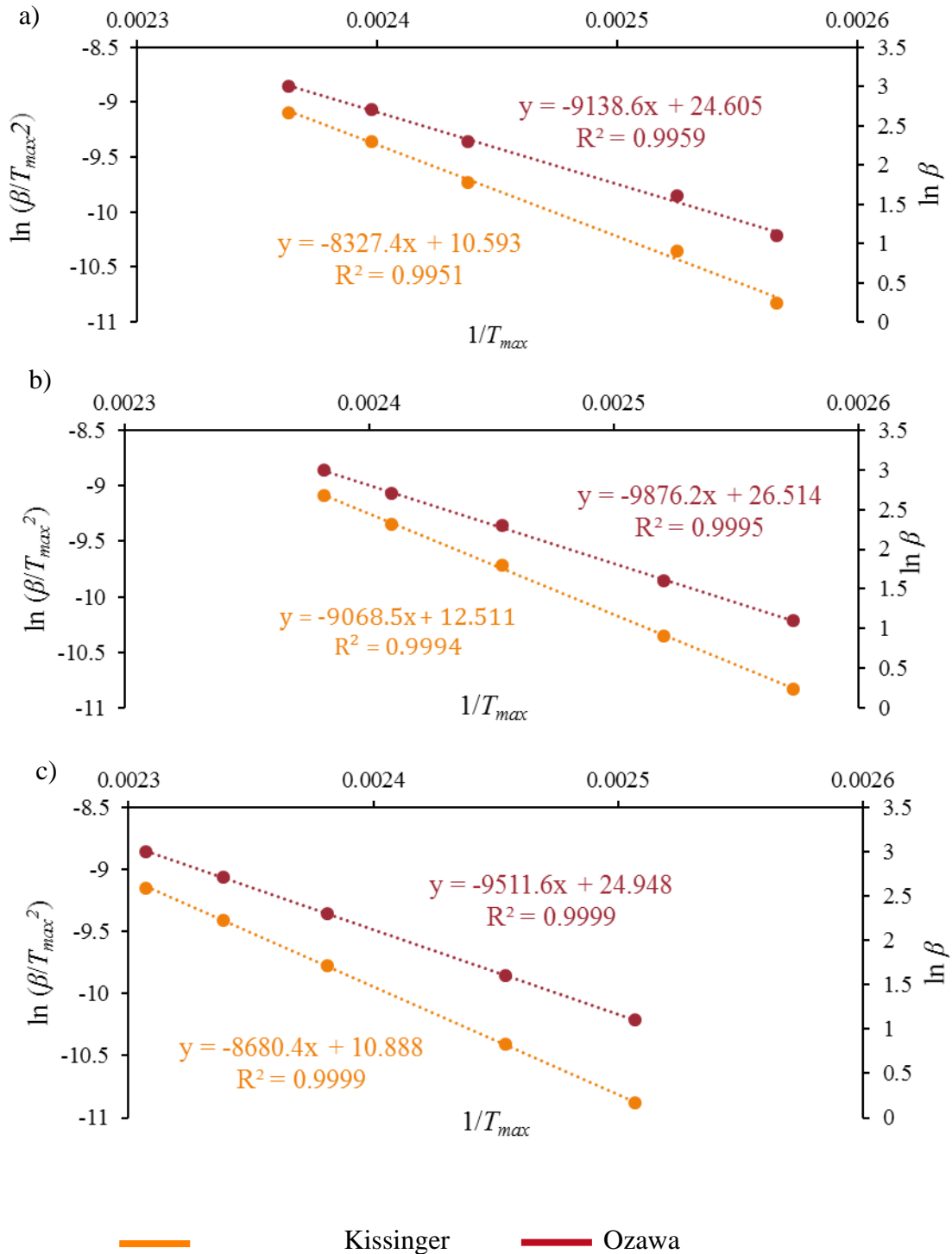
Figure 44: Kissinger and Ozawa plots for resin blends **1** (a), **2** (b) and **3** (c).

The same experimental procedure was applied to the industry benchmark resin, resulting in the following Kissinger and Ozawa plots, (Figure 45) and associated parameters (Table 16). Note the rate constant was calculated at 70 °C (348 K) which was the cure temperature prescribed for this resin system.
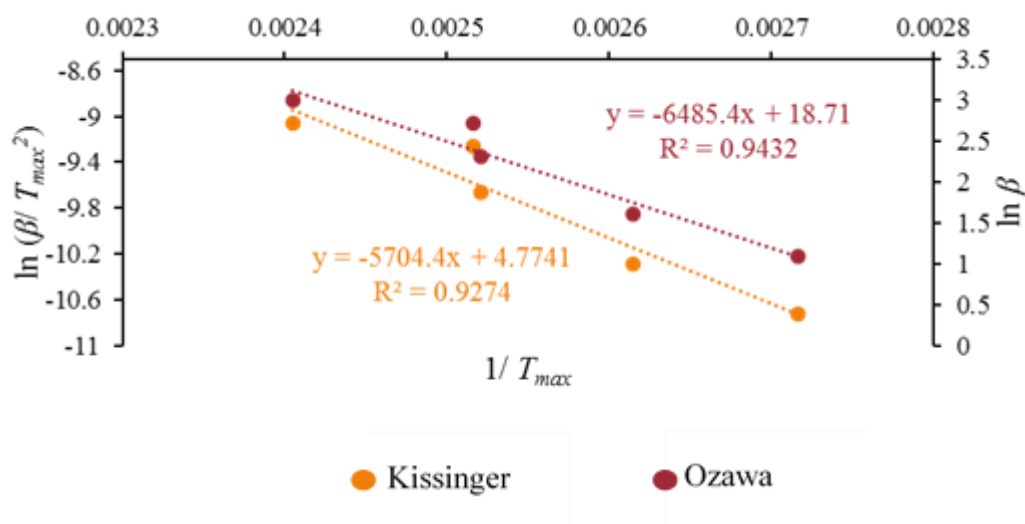
Figure 45: Kissinger and Ozawa plots for the industry benchmark resin.

Table 16: Kissinger and Ozawa kinetic analysis for the industry benchmark.

Blend	Ozawa method E_a (kJ mol^{-1})	Kissinger method E_a (kJ mol^{-1})	Pre-exponential factor A (s^{-1})	Rate constant k (10^{-2}) at 348 K (s^{-1})
Industry benchmark	51.3	47.4	6.8 x 10^5	4.04

The kinetic data shows that the benchmark amine-based system cures at faster rate than the anhydride resins, with lower activation energies and a faster rate constant at cure temperature. This furthers the understanding from thermal analysis of the resin in Chapter 4.2.3, where anhydrides were shown to have lower reaction enthalpies.

Overall, this shows that anhydride-cured epoxies could be more desirable for use in wind turbine blades. These structures have thick composite sections, which as discussed in Chapter 2 have great manufacturing challenges due to thermal gradients during cure. As

these resins generate less exothermic heat and have slower reaction kinetics it could mitigate risk of uncontrolled exothermic reactions.

5.3. Isothermal cure kinetics

The kinetic parameters obtained from dynamic DSC experiments has enabled comparison to be made of the resin blends in terms of their activation energies, pre-exponential factors, and reaction rates at cure temperature. However both Kissinger and Ozawa methods only enable certain cure kinetic parameters to be estimated by assuming first-order cure kinetics but these models do not enable the degree of cure to be estimated as the reaction progresses [217]. For this isothermal cure kinetics must be assessed to validate a cure kinetics model which most accurately captures the resin cure behaviour. A more comprehensive model of the cure kinetics was required to be used be for modelling the cure reaction as required for FEA modelling of vascular curing, and to convert the experimentally measured temperatures to degree of cure, used in Chapter 7.

The approach taken to study the cure kinetics was to fit the reaction rate profiles, which are obtained from the isothermal and dynamic DSC experiments, to cure kinetic models. One of the most widely used models for epoxy resins (including anhydride-cured epoxies) in literature is an autocatalytic model, Equation 20 [224]. The cure reaction is autocatalytic meaning that one or more of the products of the polymerisation process act as a catalyst for the same reaction.

$$\dot{\alpha} = (k_1 + k_2\alpha^m)(1 - \alpha)^n \tag{20}$$

where, $\dot{\alpha}$ is the cure reaction rate; m and n are reaction orders; and k_1 and k_2 are reaction rates. In the Ryan and Dutta model [225], k_1 is taken to be the initial reaction rate when time (t) and $\alpha = 0$, hence k_2 can be determined using Equation 21 [225].

$$k_2 = \frac{(2 - m)k_1\alpha_p^{1-m}}{m - 2\alpha_p} \tag{21}$$

where, α_p is the degree of cure at the maximum rate of reaction.

By using a reduced gradient non-linear optimisation method implemented in Microsoft Excel the optimum values of m and n are determined by minimising the sum of the squared differences between experimental reaction rates and predicted reaction rates, in a similar manner to that described by Karkanas [226]. However, this autocatalytic model

presented a poor fit to the experimental data beyond 60% conversion, as shown in Figure 46.
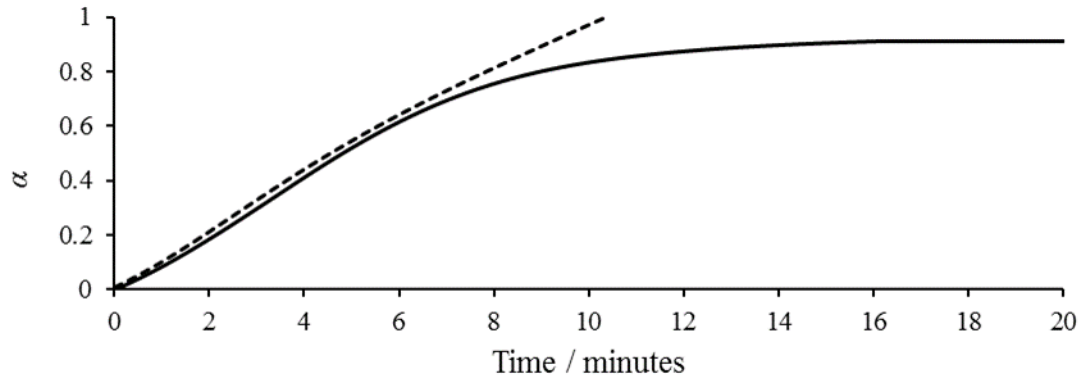
Figure 46: Autocatalytic model fitting (dotted line) to experimental isothermal DSC data (solid line) at 110 °C in plot showing degree of cure *versus* time.

There are many different cure kinetic models which can be considered, from extensive literature reading a modified autocatalytic cure kinetic model was identified, referred to as the Karkanas model, Equation 22 [226, 227]

In this study, when the Karkanas model was compared to the experimental data it captured the final stages of cure more accurately than had been achieved with the autocatalytic model, as shown in Figures 47 and 48.

The reaction orders: *m*, *n₁*, and *n₂*, were determined using the optimisation solver in a similar manner to that previously used for the autocatalytic cure kinetic model. The reaction orders determined for the modified autocatalytic (Karkanas) model are given in Table 17.

$$\dot{\alpha} = k_1(1 - \alpha)^{n_1} + k_2\alpha^m(1 - \alpha)^{n_2} \tag{22}$$
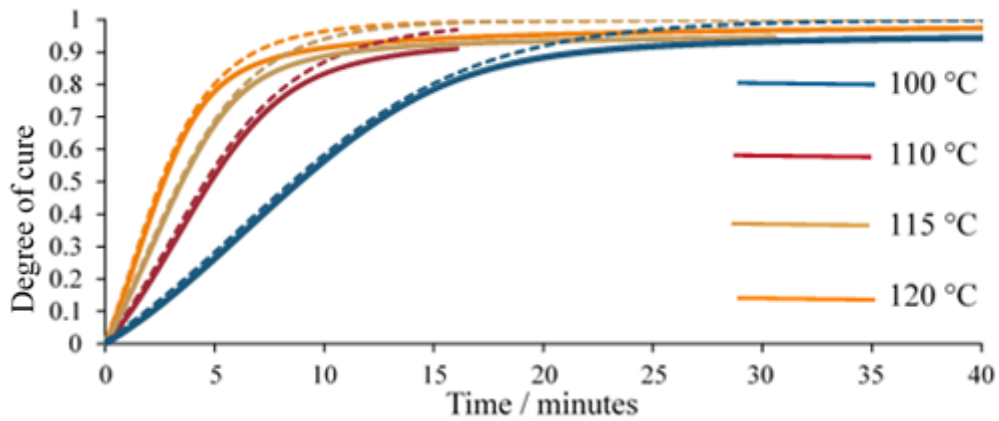
Figure 47: Plot of degree of cure *versus* time for isothermal cure at various temperatures. Comparing experimental data with modified cure kinetic model (dotted line).
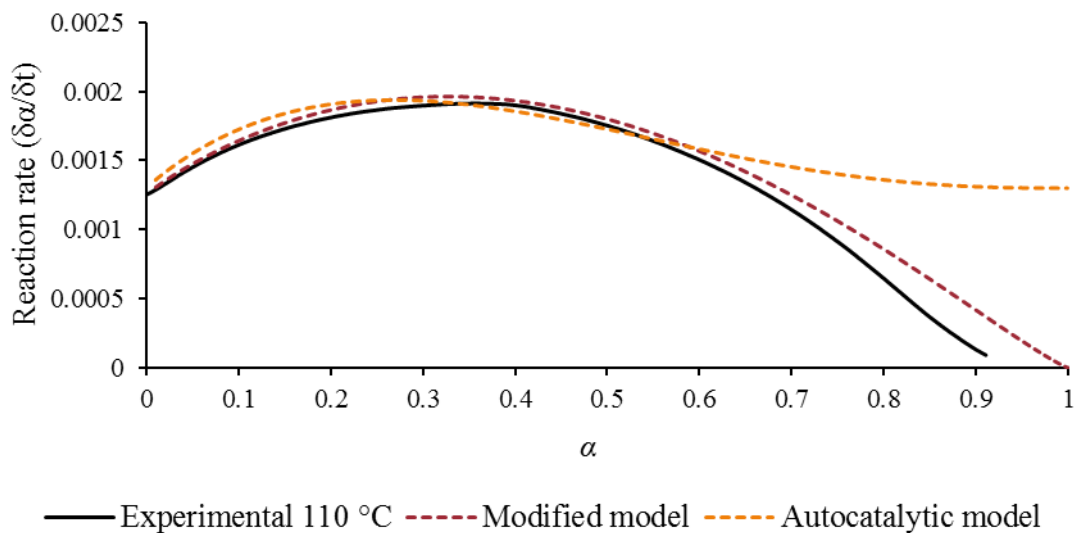
Figure 48: Reaction rate *versus* degree of cure at 110 °C. Comparing both autocatalytic model and modified (Karkanas) model to experimental data.

As highlighted, the modified autocatalytic/ Karkanas model described herein fits the data well in the chemically-controlled regime, with several reactions leading to the formation of the polymer network. However, at higher levels of conversion ($\alpha > 0.65$, shown in Figure 47) there appears to be deviation between the model predictions and the experimental data. Though it should be noted this deviation seemed to be less than that observed using the unmodified autocatalytic model. Beyond *c.a.* 65% conversion, the reaction is in a diffusion-controlled regime, whereby the mobility of the unreacted groups becomes increasing hindered as the polymer network grows thus reducing the

90

rate at which these groups can diffuse through the bulk polymer and react [228]. There are models which look to capture the rate of diffusion as well as the chemically-controlled reaction rates, however these are not explored in this work [228, 229]. As the mean error squared between the experimental and model predictions was below 3.5×10^{-9}, it was accepted that the modified autocatalytic model was able to model to progression of cure to a good degree and therefore could be used in Chapter 7 to allow for FEA simulation of the cure reaction.

Table 17: Kinetic parameters at different isothermal temperatures.

Temperature	k_1	k_2	reaction orders		
(°C)	($\times 10^{-4}$ s^{-1})	($\times 10^{-4}$ s^{-1})	m	n_1	n_2
100	7.4	23.8	1.02	0.89	1.01
110	12.5	53.5	0.95	1.13	1.17
115	20.0	55.1	0.98	0.94	1.18
120	26.3	77.0	0.90	1.14	1.23

The pre-exponential factors (A_i) and activation energies (E_{ai}) were determined from the rate constants k_1 and k_2. The rate constants, given in Table 17, increased with temperature following the Arrhenius relationship. From the linear least-squares fit of ln k_i *versus* $1/T$, Figure 49, the pre-exponential factors (A_i) and activation energies (E_{ai}) were determined from the *y*-intercept and gradient respectively, given in Table 18.

Table 18: Cure kinetic parameters E_a and A for resin blend **1**.

Activation energy, E_a		Pre-exponential factor, A	
E_{a1} (kJ mol^{-1})	78.5	A_1 (s^{-1})	7.3×10^7
E_{a2} (kJ mol^{-1})	69.2	A_2 (s^{-1})	1.2×10^7
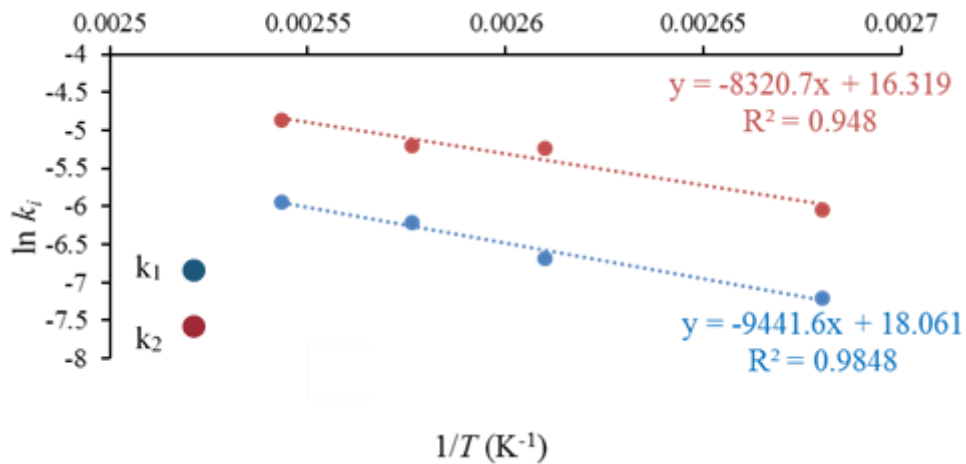
Figure 49: Linear least-squares fit of ln k_i versus $1/T$ for resin blend **1**.

Kinetics based on isothermal data can only be obtained over a narrow temperature range, from the onset of cure to the exothermic peak observed during a dynamic DSC thermogram. For resin blend **1** this range is from 75 °C (onset of cure) to 135 °C (exotherm peak). Figure 50, shows the Karkanas autocatalytic model fitted to the 10 °C min^{-1} and 2 °C min^{-1} dynamic cure of the resin using the kinetic parameters determined from the isothermal study, given in Tables 17 and 18. For the reaction orders, the average of the m, n_1 and n_2 were used, determined to be 0.96, 1.03 and 1.15 respectively.
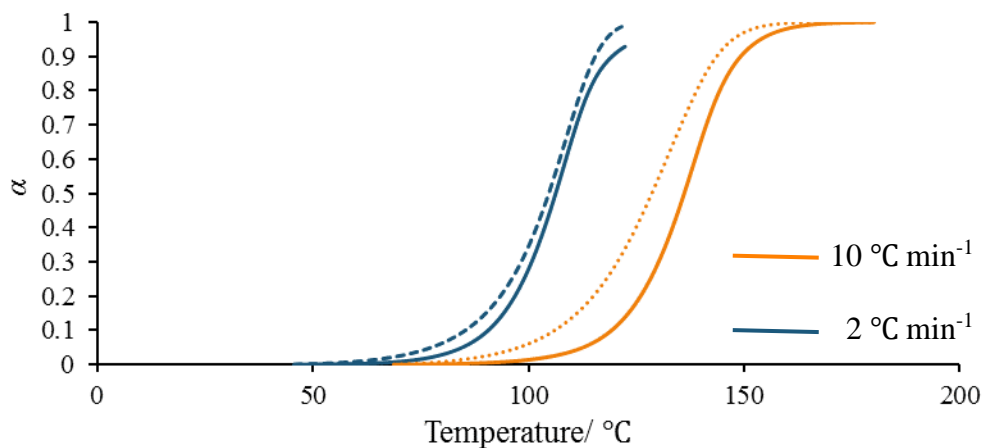
Figure 50: Plot of degree of cure *versus* temperature for dynamic thermal traces at 10 °C min^{-1} and 2 °C min^{-1} ramp rates. *N.B.* The dashed line represents the cure kinetic model data and the solid line the experimental data from DSC analysis.

Although there is some discrepancy between the model and the experimental data, the mean squared error was found to be very small 0.003 between the predicted rate of reaction and that seen experimentally. It was also shown from Figure 50, that the model does fit better with slower temperature heating rates, which may be due to the lag in heat transfer at faster heating rates. It was deemed that as the model fits well with the slower heating rate of 2 °C min^{-1} it is still valid, as this heating rate is comparable with that used in the oven cure cycle which is set ramp at to 2 °C min^{-1} and is likely to lag behind this to account for heat transfer. This model was already validated in isothermal conditions such as those observed during the dwell of the cure cycle and was shown to capture the resin cure behaviour more accurately than the more widely used autocatalytic model.

5.4.   Summary

The Kissinger and Ozawa models allowed for the cure kinetic parameters E_a and A to be estimated for each resin blend in a quick and easy manner. Thus, allowing for comparisons to be made between the different anhydrides, allowing examination of the effect of anhydride structure on the resin cure kinetics.

As discussed more detailed assessment of the resin cure kinetics for resin blend **1** was conducted to enable a cure kinetic model to be found which could be used to predict the cure progression. A cure kinetic model was required for the vascular cure work in Chapter 7. From the work outlined in this chapter, the modified autocatalytic/ Karkanas model was selected to be used in this work. This modified autocatalytic (Karkanas) model displayed the best fit to the isothermal and dynamic DSC experimental data, compared to the Ryan-Dutta autocatalytic model which was more widely reported in literature to model anhydride-cured epoxy resins.

6 COMPOSITE LAMINATE INTERFACIAL PROPERTIES

It is well understood that the interfacial properties of composite laminates are critical to the overall performance, this being how well the resin and fibre adhere to each other. It is understood that composite laminate strength in tension and bending increases with greater resin and fibre adhesion, but this increase in interfacial shear strength often leads to reduction in impact performance [61]. In this chapter the interfacial properties of the anhydride-cured epoxies are studied by examining both the interlaminar and interfacial shear strength.

Firstly, the interfacial properties of the anhydride-cured epoxies were assessed on the glass fibre supplied by HCCL, the fibre they currently use for WTB production. The interlaminar shear strength (ILSS) was characterised *via* short beam shear mechanical test. This is a macromechanical technique which was used to indirectly assess the interfacial properties of the matrix on the fibre [163]; assessing the effect of anhydride structure upon ILSS and benchmarking this against the industry benchmark.

The interfacial shear strength (IFSS) was then assessed using the microbond test technique. Section 3.4.7 critically reviewed the many methods available to characterise the IFSS and reasons why the microbond testing technique was used.

One aim of the thesis was to assess the viability of using this resin in carbon fibre composite systems. As highlighted in Chapter 2, the industry is moving toward using carbon fibre as this enables larger blades to be produced by minimising weight, thus allowing greater energy efficiency. The aim was to assess the interfacial properties of the resin on carbon fibre with different sizing/surface treatments to advise HCCL on their fibre selection. As will be discussed in this chapter there was issues with the use of

the microbond test setup to assess carbon fibre, therefore only preliminary work is presented.

6.1. Experimental

The experimental setups and techniques used to characterise the ILSS and IFSS are described herein. The reasoning behind the selection of the microbond test to examine the IFSS was given in Section 3.4.7.

6.1.1. Glass fibre laminates

6.1.1.1. Laminate manufacture

A preform of five plies (250 mm x 150 mm) of a biased 0/90° biaxial NCF fabric (LTx1240, supplied by Owens Corning technical fabrics, the specification of the fabric was given in Section 3.2.1) was laid up in a uniform direction on a tool plate for vacuum assisted resin infusion (VARI). The resins (resin blends **1**-**3** or industry benchmark) were prepared as outlined in Section 3. The resin was pulled through the preform using a vacuum, the VARI process was described in Section 3.3.

Once infused the laminate was cured given the prescribed cure cycle in an air circulated oven. For resin blends **1**-**3** this was: ramp 2 °C min^{-1} to 75 °C, dwell at 75 °C for 12 hours before cooling to room temperature. For the industry benchmark this was: 2 °C min^{-1} to 70 °C, dwell at 70 °C for 6 hours before cooling to room temperature.

6.1.1.2. Resin burn off

Resin burn off tests were conducted following ASTM standard D2584-18 [230]. Ceramic crucibles (with lids) were heated in a furnace to 500 °C, these crucibles were then allowed to cool to room temperature in a desiccator before being weighed. A GFRP composite sample (weighing approximately 2.5 g) was added to the crucible and weighed again. The crucible (containing the sample) was returned to the furnace (500 °C). The weight was recorded periodically until the crucible and residue maintained a constant weight (within 1.0 mg). The weights were recorded after the crucible had cooled to room temperature.

6.1.1.3. Short beam shear testing

The short beam shear test procedure was conducted following the ASTM standard D2344 as outlined in Section 3.4.6. The GFRP laminates manufactured as described in

Section 6.1.1.1, the average measured laminate thickness was 4.1 mm (SD 0.13). Due to the laminate thickness to meet the dimension requirements as described in Section 3.4.6, the samples were cut oversized and polished to refine the size to the desired geometry (33 ±1 mm x 9.5 ±1 mm). To account for biaxial nature of the reinforcement, specimens were cut with the dominant (0°) fibre in the sample length and loaded perpendicular to it. The span length of the test fixture was fixed at 24 mm. The specimens were loaded until failure. The load *vs* displacement data was recorded during testing.

6.1.2. Microbond testing

A procedure had to be developed which would hold the fibres taut whilst uncured resin was applied and allow the setup to be easily transported to the oven for curing. For this a silicone mould was made to allow for the fibres to be held taut as they were adhered to the end tabs, as shown in Figure 51. Firstly, an inverse mould was 3D printed, from which a silicone mould was cast. The silicone could be used to a maximum temperature of 250 °C and therefore would be suitable as it would withstand the cure temperatures for the resin systems assessed in this work.

The fibres were laid across the silicone mould and mounted into plastic tabs using Dymax OP ultra-lightweight UV curable adhesive 3193 [231]. To ensure the fibre was taut, the fibre was secured using double sided tape, the setup is shown schematically in Figure 51. The adhesive was then allowed to cure under UV light for several hours (typically 3 hours).

Figure 51: Schematic of the setup used to prepare the single fibre specimens.

The resin was then mixed and degassed as specified in Section 3.1. A method to apply suitably small volumes of resin to the fibre surface had to be established. In literature, various methods are reported including using a fine needle [232], an alumina fibre secured to a drawn glass tube [185], or super fine tweezers [233]. For ease and

simplicity, the method found to be most reliable to form consistent droplets in the appropriate embedment length range (80-200 μm), was using a single glass fibre (H-glass from LTx1240 fabric, fibre diameter 17 μm) attached to a glass pipette using tape. The glass fibre was dipped into a small amount of resin and then wiped on the taut fibre held in the silicone mould, leaving behind a single resin droplet. On each fibre 6-8 droplets were applied.

Microbond testing of the anhydride-cured epoxies was conducted with relative ease. However, curing the droplets of the industrial benchmark resin was found to be problematic. The industry benchmark resin when applied to droplet and cured following its prescribed cure cycle the droplet was unable to cure sufficiently. This was observed in testing as instead of debonding from the fibre, the droplet was instead smeared along the supporting fibre. This was observed even when longer and higher temperature cure cycles were used, *i.e.* 12 hours at 70 °C or curing at 90 °C for 6 or 12 hours. This phenomenon was hypothesised to occur as such small volumes of resins were being cured, there was not enough bulk to generate the heat to cure the resin.

Therefore, an alternative amine-cured epoxy resin was sourced to be used as a baseline resin to compare the interfacial adhesion of the anhydride-cured epoxies to. The resin selected was Prime[TM] 20LV cured with extra slow hardener. Prime[TM] 20LV was reported to be used for infusion of wind turbine blades due to its low viscosity and long working time, and its ability to reach excellent mechanical properties even at moderate cure temperatures [234]. From assessment of the Prime[TM] 20LV datasheet [234], the technical data provided by Hexion (previously Momentive) on the industry benchmark resin [235], and data obtained in Chapter 4, demonstrated these resins had similar properties. For example, Prime[TM] 20LV had a reported mixed viscosity at 25 ºC of 220-243 cP which can be compared to the reported value of 250-280 cP for the industry benchmark. The cured T_g was also similar, the Prime[TM] 20LV resin reportedly had cured T_g of 70 ºC as determined by DMA when cured for 16 hours at 50 ºC, compared to the data obtained in Chapter 4, which reported the T_g to be 70 ºC as measured by DMA.

Prime[TM] 20LV resin was prepared by mixing the epoxy and extra slow hardener in 100: 26 weight ratio [234]. The resin was applied to the fibre to form droplets in the same manner as used for the anhydride-cured epoxy resins, as described in Section 6.1.2. The droplets were oven cured with the following cure cycle: ramp to 70 °C at 2 °C min^{-1} and held isothermally for 6 hours. This resin was used in the microbond test

as a baseline amine-cured epoxy to which the anhydride-cured epoxies were benchmarked against.

All droplets were cured on the fibres whist on the silicone mould in an air circulated fan oven, using the cure cycle prescribed for the given resin. It was identified that the air circulating ovens may cause too much movement of the fibres during the cure, which could lead to fibre breakage or loss of resin droplets. To prevent these issues an aluminium box was purchased, and holes were created at various locations to allow some air circulation. The silicone mould was housed within this aluminium box during the cure.

Once cured, optical microscopy, was used to size the droplets, an example of the images taken is shown in Figure 52. The droplet embedment length and diameter were measured using the measurement tools the microscope AxioVision software.

As discussed in Section 3.4.7, the microbond test works by pulling a fibre with a cured resin droplet through a microvise gap. As the gap is too small to pull the droplet through, the interface de-bonds as the fibre is pulled through. The force required to pull the fibre through the microvise gap was recorded during the testing. In this work a Dia-stron microbond tester, fitted with a 2000 gmf (20 N) load cell was used.
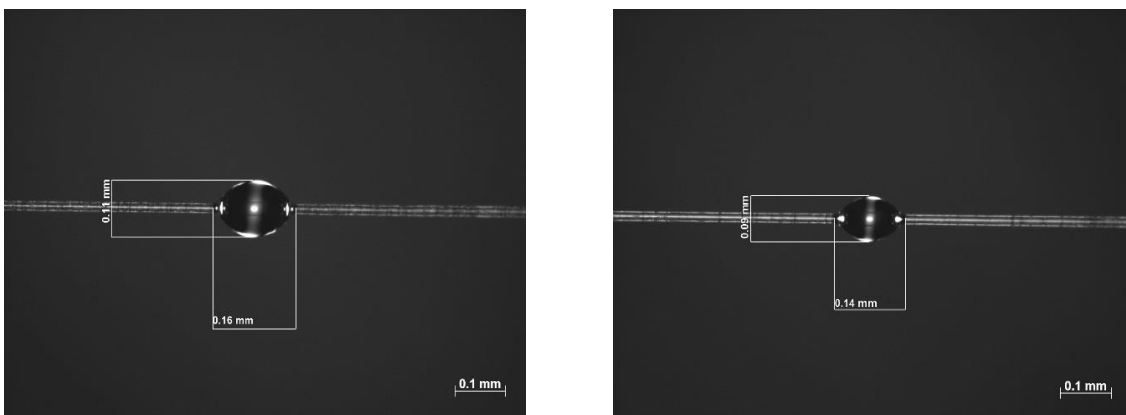
Figure 52: Optical micrographs of typical droplets on glass fibre supplied.

However, the microvises originally purchased with the test machine came in following gap sizes (50 μm, 100 μm, 150 μm and 200 μm). From literature the understanding was that the microvise gap should be twice the size of the fibre diameter, as discussed in Section 3.4.7. As the H-glass fibre had a diameter of 17 μm, the 50 μm size microvise

was selected as this closest to the required size. However, instead of interfacial debonding being observed, the resin droplet was itself being sheared, with matrix droplet breakage occurring, as shown in Figure 53. It was hypothesised that this was due to the gap being too large and therefore causing stress concentrations in the matrix and not at the interface.
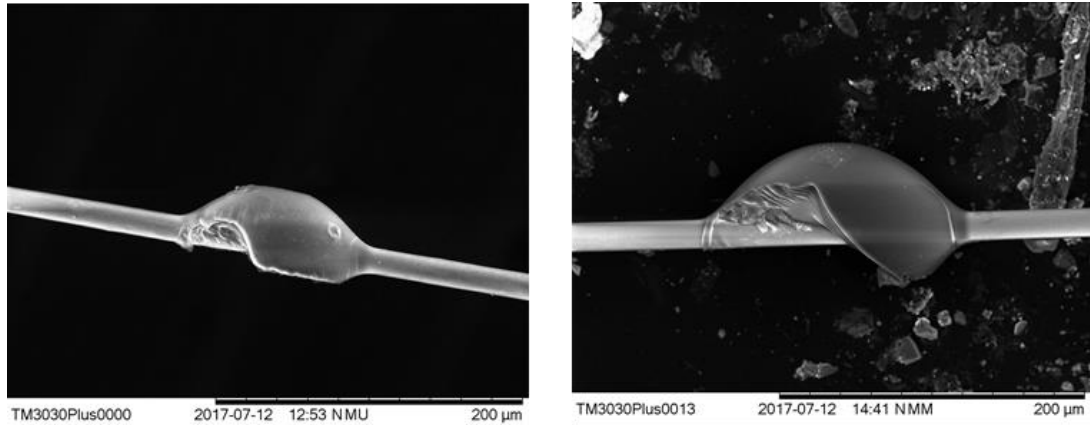
Figure 53: SEM micrographs of droplets sheared during the microbond tests using a 50 μm microvise gap.

Therefore, microvises with smaller gap sizes were machined. The microvises were cut from a tungsten plate of thickness 0.25 mm using an Oxford Lasers Alpha System, operating at 532 nm (green) with a pulse frequency of 1 kHz. The laser (300 mW power) moved across the tungsten at a speed of 2 mm s^{-1}, so the pulses were 2 microns apart and had a width of 5 microns. The microvises obtained had following gap sizes: 9 μm, 20 μm and 29 μm, *N.B* the gap sizes were measured from SEM micrographs using imageJ software, taking and average of 10 measurements. These micrographs also showed that the type of microvises used had a sharp edge which was used to shear the droplet, as shown in Figure 54, refer to Section 3.4.7.1 for difference between sharp and blunt edge microvises.

The Dia-stron test machine works as the tab is held in the holder and the fibre is laid so the droplet to be tested lies behind the microvise. The tab was moved laterally away from the microvise at a speed of 0.016 mm s^{-1}. The test machine is shown in Figure 55. Note that the fibres were cut in half so that each end tab was loaded separately.
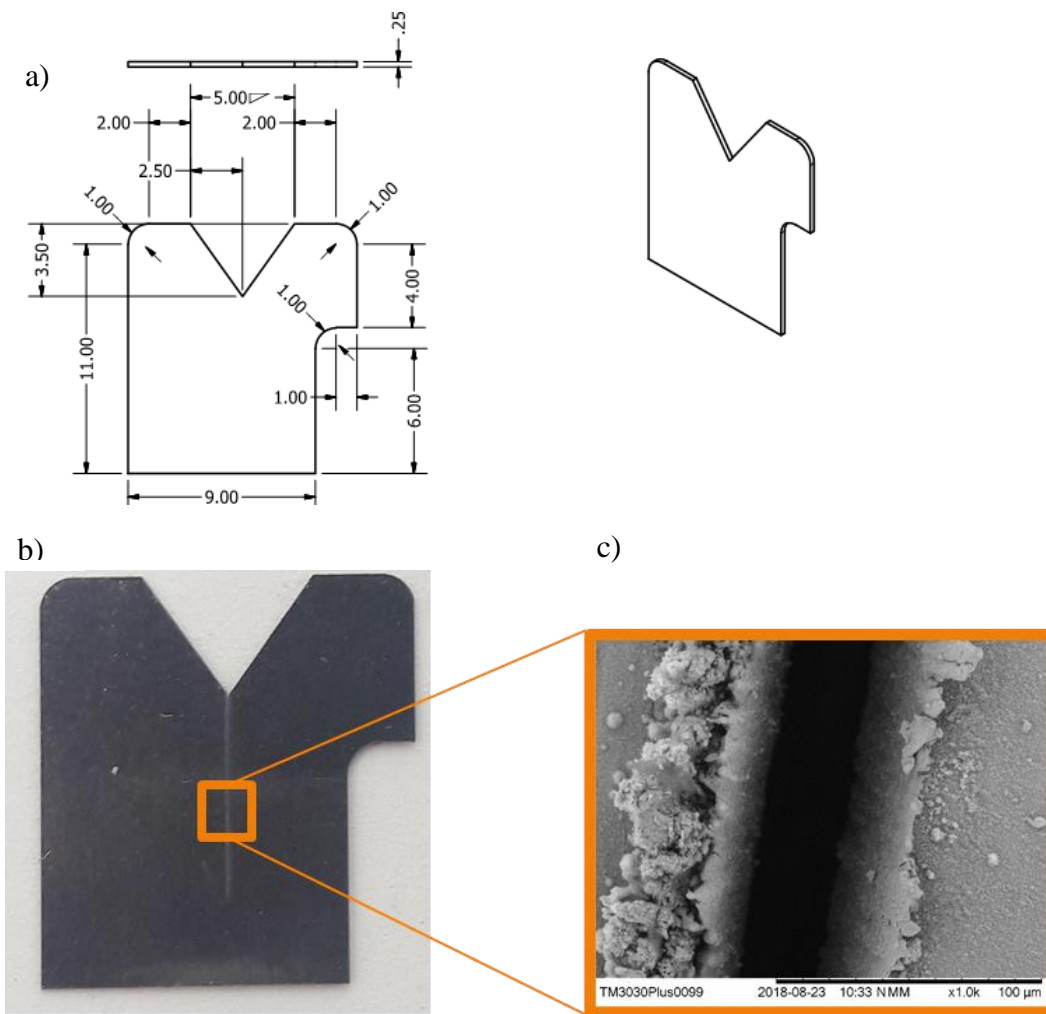
Figure 54: a) AutoInventor drawing used to specify the outer geometry of the microvise, units in mm; b) photograph of laser cut microvise; c) SEM micrograph of the microvise used to determine the microvise gap- 29 μm.
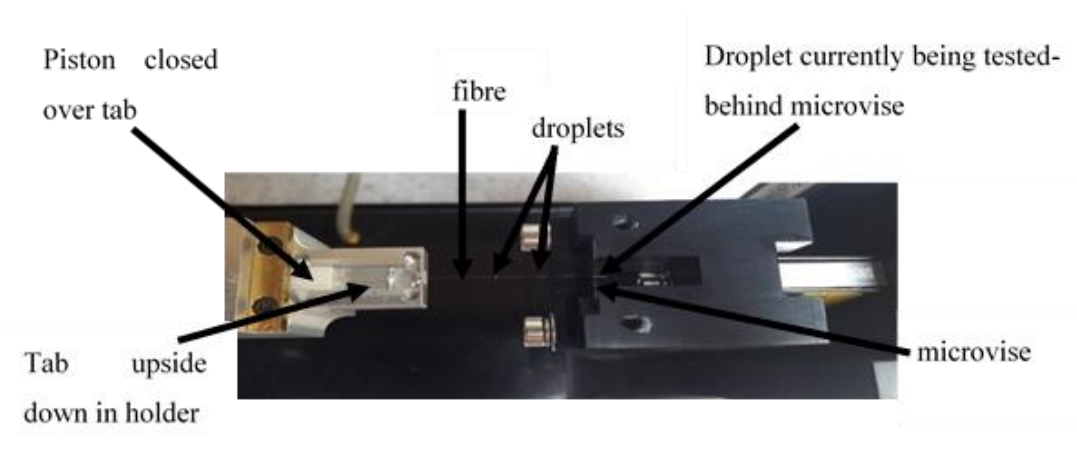
Figure 55: Annotated photograph of microbond test machine, as viewed from above.

6.1.3. Carbon fibre laminates

6.1.3.1. Laminate manufacture

A preform of six plies of the ±45 carbon fibre NCF fabric (fabric details were given in Section 3.2.2) were laid up in stacking sequence $[(0/90)]_{3s}$, the preform was prepared for infusion using the bagging procedure described in Section 3.3. The resin (resin blend **1** or industry benchmark) was prepared and degassed as outlined in Section 3. The preform was infused with the resin at room temperature. Once infused the laminate was cured with given the prescribed cure cycle:

- For resin blend **1**: ramp 2 °C min^{-1} to 75 °C, dwell at 75 °C for 12 hours before cooling to room temperature.

- For the industry benchmark: 2 °C min^{-1} to 70 °C, dwell at 70 °C for 6 hours before cooling to room temperature.

6.1.3.2. Short beam shear testing

Samples for short beam shear testing were cut so that the fibre direction was 0/90° from the laminate made with ±45° fibre direction. The testing was conducted in accordance with ASTM D234 using the procedure outlined in Section 3.4.6. The average thickness of the laminates manufactured using the procedure outlined in Section 6.1.3, was 2.7 ±0.4 mm. The specimens were cut and polished to following specimen dimensions: length 16.0 ±0.2 mm and width 4.6 ±0.8 mm, the span length of the test fixture was adjusted so that the loading noses were positioned 11 mm apart. The samples were tested in the same manner as described in Section 6.1.1.3.

6.2.   Results and discussion

The following section presents the results from the tests undertaken to probe the interfacial properties of the resins on both glass and carbon fibre surfaces.

6.2.1. GFRP fibre volume fraction

The fibre volume fraction of the laminate infused with resin blend **1** was determined following the resin burn off test as outlined in Section 6.1.1.2, it was assumed the same v_f was attained for all laminates manufactured. Following the burn off test, the residue

corresponds to the weight of the glass fibre, w_f. The average weight fraction of the glass fibre was 75 wt%. The fibre volume fraction was calculated using Equations 23-25.

$$\frac{v_f}{v_r} = \frac{w_f}{1 - w_f} X \frac{\rho_r}{\rho_f} \tag{23}$$

$$v_m = \frac{1}{1 + \frac{v_f}{v_r}} \tag{24}$$

$$v_f = 1 - v_m \tag{25}$$

The density of the glass fibre, ρ_f, was assumed to be 2.6 g cm^{-3} [236]. The density of the resin, ρ_r, determined in Section 4.2.8.1 was used, 1.22 g cm^{-3}. v_m is the matrix volume ratio. It was assumed that there were no voids in the laminate. The average v_f was determined to be 57%.

6.2.2. ILSS of the GFRP laminates

The ILSS of the GFRP specimens was determined using Equation 26:

$$ILSS = \frac{3\,F}{4 \times b \times h} \tag{26}$$

where F is the maximum load observed (N), b and h are the specimen width and thickness (mm) respectively.

A typical force *versus* displacement plot for each resin blend recorded during the short beam shear experiment is shown in Figure 56.
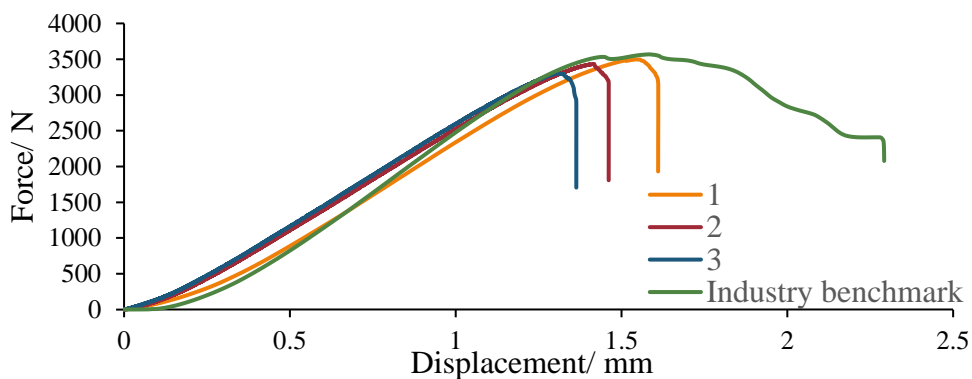
Figure 56: Force *versus* displacement plot for each of the four resin blends, resin blends **1**-**3** and the industry benchmark.

For each resin system this data was recorded for five samples, the calculated values for each resin system are given in Table 19, standard deviation given in brackets. The

average thickness of the laminates was 4.1 mm (SD 0.13), note in the calculation of the ILSS was done using the exact dimensions of each test specimen before averaging.

Table 19: ILSS values for each resin system GFRP laminate.

Blend	Average ILSS (MPa)
1	65 (2.4)
2	67 (3.2)
3	66 (3.7)
Industry benchmark	56 (1.4)

This shows that within experimental error all the anhydride resin systems had same ILSS and show significant improvement (18%) over the amine-cured industry benchmark.

However, from examining the failure patterns of the test specimens, Figure 56, it was observed that the industry benchmark displayed a much more gradual failure. In the anhydride-cured resin GFRP systems a sudden drop was observed soon after reaching the maximum load. A gradual failure in short beam shear testing is often associated with a more toughened system response. The industry benchmark curing agent Epikure^{TM} RIMH037 is a mix of poly(propylene glycol)bis(2-aminopropyl ether) (50-75 %) and 3-aminomethyl-3,5,5-trimethlcyclohexylamine (25-50%) [235]. The largest component in the industry benchmark curing agent is an aliphatic amine, Garcia *et al.* [237], showed that aliphatic amines showed increased fracture toughness over cyclic amines. The aliphatic chains of the industry benchmark impart greater flexibility to the molecule and thus the cured thermoset network. Aliphatic chains are not present in the anhydride-cured epoxies. The increased molecular flexibility of the amine-cured industry benchmark could explain the more gradual failure observed.

6.2.3. Microbond analysis of resins on H-glass fibre

The force *versus* displacement for each droplet was recorded during the test. A typical trace of a successful microbond test is given in Figure 57. During the test, the observed force reaches a maximum (interfacial failure of the droplet and fibre) and then drops and subsequently a small (frictional) force is measured as the droplet is dragged along the fibre. If the fibre broke during the test then only a force drop was observed, all fibre break data were omitted.
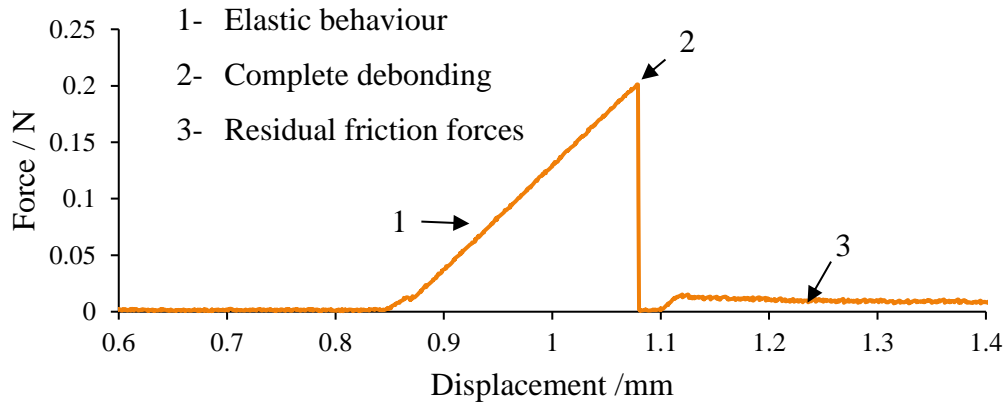
Figure 57: Typical force *versus* displacement plot obtained from a successful microbond test.

SEM micrographs were obtained after microbond testing, to ensure correct failure was achieved, before data was included in subsequent analysis. Figure 58, shows an example of the microbond failure as observed by SEM after testing. It showed a fraction of the droplet was left at the droplets initial position, Figure 58a. Figure 58b shows the displaced droplet at a distance from this. The residue of the droplet left at the initial bonding position was relatively small, thus indicating that having a narrower microvise gap has not resulted in excess matrix cracking and the residue of the droplet is negligible compared to the fibre embedded length [170].

The surface of the fibre where the droplet was initially bonded can also be studied to examine the hackle patterns on the fibre surface. An example from an anhydride-cured resin sample and the amine-cured industry benchmark is shown in Figure 59 [176]. It was observed that greater evidence of these hackle patterns was found in samples of the anhydride-cured resins whereas a much smoother fibre surface was observed for amine-cured resin system. Evidence of hackle patterns alluded to that fact that the interfacial adhesion was much greater. Whereas smoother surface indicated that debonding of the interface occurred along the entire embedment length simultaneously, hence a weaker interface. This was observed in the value of IFSS determined for each case.
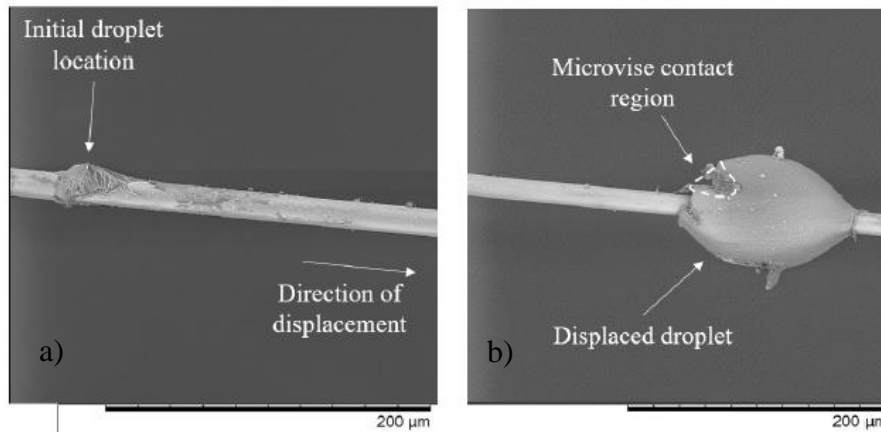
Figure 58: SEM images of a microbond sample after testing. a) SEM showing residue of droplet left at initial bonding site. b) SEM image of the displaced droplet.

Once it was identified that the failure observed in testing was due to the interfacial shear failure of the droplet and fibre, then the data were compiled for each resin on the glass fibre supplied in order to determine the interfacial shear strength (IFSS).
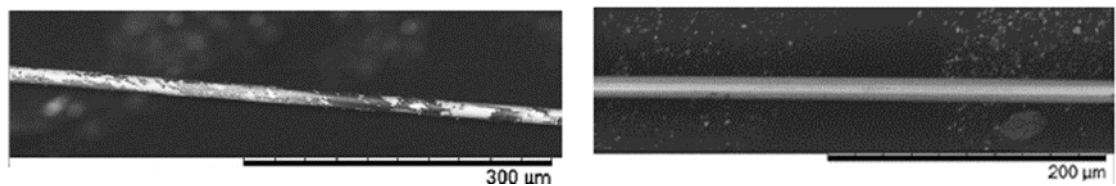
Figure 59: a) SEM image showing hackle patterns from debonding of anhydride-cured resin system. b) SEM image showing lack of hackle patterns of the fibre surface with amine-cured resin, Prime^{TM} 20LV [174].

6.1.1.1 Determination of IFSS and statistical analysis

From the successful tests, scatter plots of the maximum force (F) observed during the test *versus* the embedded length of the droplet, is given in Figure 60. A linear regression line of best fit was forced through the origin. Outliers were removed from the data set by removing any data points where the error squared between the experimental data and the predicted value from the linear regression line exceeded 0.01 (*i.e.* measured force was +/- 0.1 N from the predicted force determined from the linear regression line). From the gradient of this linear regression line the average IFSS for each resin blend was calculated by dividing the gradient by $d_f\pi$ (fibre circumference, $d_f = 17$ μm), following the

relationship given in Equation 11, Section 3.4.7.1. The calculated average IFSS for each matrix on the glass fibre is given in Table 20.
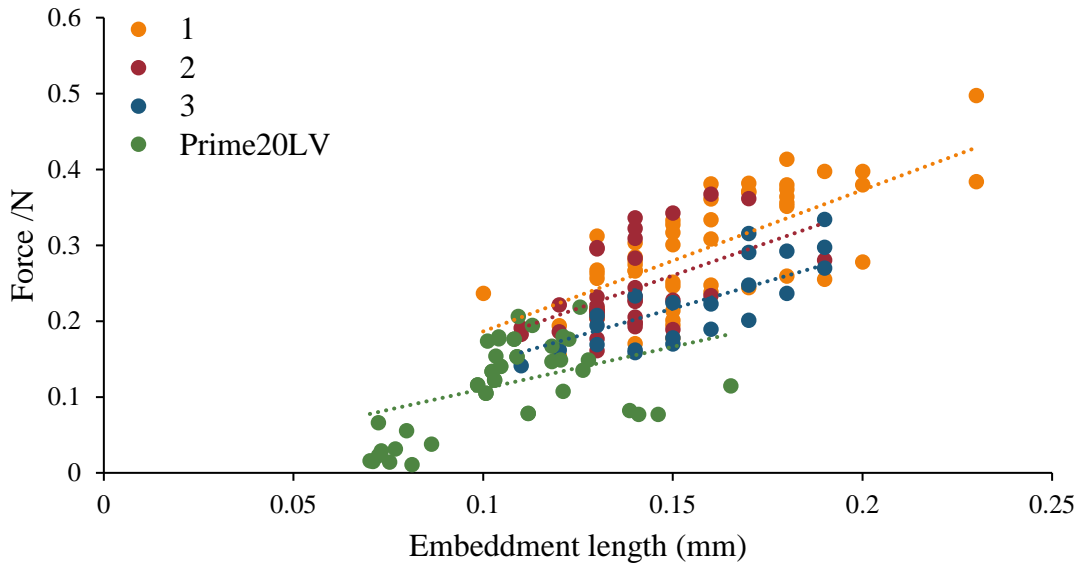
Figure 60: Plot of the maximum force *versus* the droplet embedment length for the four resins (resin blends **1** – **3** and industry benchmark) assessed on H-glass fibre.

Table 20: IFSS of each resin system (resin blend **1-3** and Prime^{TM} 20LV) on H-glass fibre.

Blend	Gradient (from Figure 60)	IFSS (MPa)	Variance of F/L$_e$ values
1	1.86	35	0.12
2	1.73	33	0.12
3	1.44	26	0.05
Prime^{TM} 20LV	1.21	21	0.30

As the microbond test is prone to large data scatter, it was vital to assess if the results were statistically different and thus allow better evaluation of the results. To do this Students T-test was used. For each successful test, the maximum observed force was divided by the droplet's embedment length ("stiffness"). A two-sample test assuming unequal variances was conducted to compare in turn each resin to the others. This method assumed that the population sampling was random, and that the data was

normally distrusted. Due to the large sample size (>20) and evaluation of skew this was found to be valid. Skewness was evaluated using the adjusted Fisher-Pearson standardised moment coefficient Equation 27.

$$S = \frac{n\sum_{i=1}^{n}(x_i - \bar{x})^3}{(n-1)(n-2)\text{SD}^3} \tag{27}$$

where n is the number of samples, $\bar{x}$ is the sample mean and SD is the standard deviation of the population sample. It was found that all resin samples had a resulting skewness, S, within the acceptable range (90%) [174].

The two-sample T-test was conducted at the 5% significance level. Therefore, if the *P-value* was greater than 0.05 the null hypothesis was accepted- the null hypothesis being that the two sample sets are not statistically significant.

For the anhydride-cured resins this statistical test shows that resin blends **1** and **2** were not statistically different but both were statistically different to resin blend **3**. This was interesting as it shows the two resins that are most structurally similar and similar ILSS values, also exhibited the same interfacial bonding strength. The anhydride structure of resin blend **3** was much bulkier and therefore more sterically hindered and therefore as predicted, this exhibited lower IFSS than the other blends. It is hypothesised that this bulkier substituent prevented the resins reacting with the reactive sites on the fibre surface.

The amine-cured Prime™ 20LV resin showed significantly lower IFSS compared to the anhydride-cured resin systems. The improved performance has been attributed to the presence of the carbonyl groups of the anhydride structures. These groups can react with the hydroxyl groups on the glass fibre surface, thus increasing number of possible bonding locations and hence improving the adhesion at the fibre interface. In comparison, the amine-cured epoxies do not have these groups and rely solely on the interaction of the epoxy component of the resin, overall having fewer reactive sites to interact with the fibre surface. Gottlieb *et al.* [238] also reported that anhydride-cured epoxies had increased interfacial adhesion with glass fibres. They had observed that in the resin assessed in their work, the presence of polar maleic anhydride within the blend resulted in increased bonding to hydrophilic silanes on glass fibre surface.

6.2.4. Carbon fibre laminate ILSS

In a similar manner to had been conducted for the glass fibre laminates, short beam shear tests were conducted to evaluate the ILSS. A typical force *versus* displacement curve obtained from the two laminates (resin blend **1** and the industry benchmark) is shown in Figure 61. As had been observed in the testing of GFRP laminates in earlier studies, a more brittle failure was observed for the anhydride-cured resin (resin blend **1**) compared to the industry benchmark, which seemed to have a more toughened response. As indicted by the gradual drop in force following initial failure.
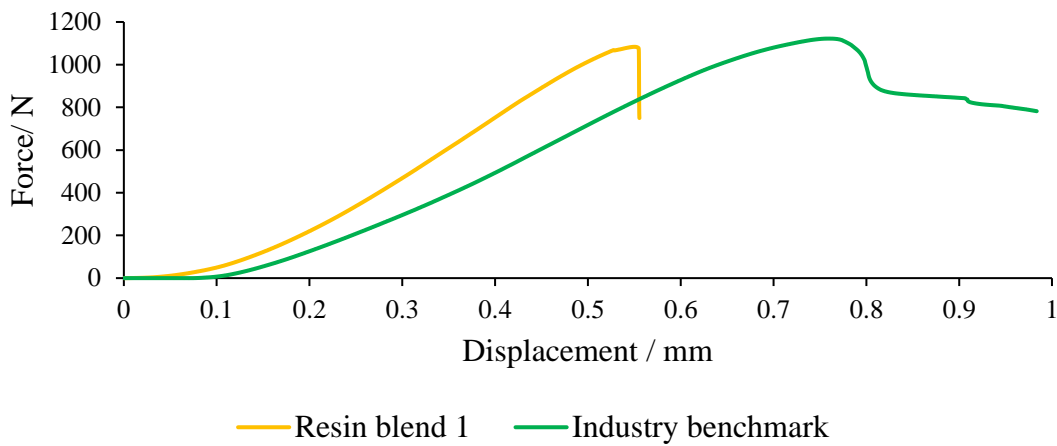
Figure 61: Force *versus* displacement plot for resin blend **1** and industry benchmark CFRP laminates obtained from short beam shear testing.

Following the same procedure as given in Section 6.2.2, Equation 26 was used to calculate the ILSS of the CFRP laminates. The ILSS was calculated using the exact specimen dimensions, Table 21 presents the mean ILSS of the six specimens. The average laminate thickness was 2.7 mm for laminate infused with resin blend **1** and 2.9 mm for the industry benchmark laminate. The data shows a 30% increase in ILSS is obtained from the anhydride-cured resin system over the industry benchmark.

Table 21: Average ILSS calculated for resin blend **1** and the industry benchmark CFRP lamimates.

Blend	Average ILSS (MPa)	Standard deviation
1	75	2.4
Industry benchmark	57	2.5

6.2.4.1. Laminate quality assurance

To ensure these results are reliable the quality of the infused laminates was assessed by potting and polishing samples of these laminates for micrograph analysis to observe the void content. TGA analysis was also used to assess the fibre volume fraction.

The fibre weight fraction was assessed using TGA in the same manner as described in Section 4.1.1.4. The following thermograms are overlaid in Figure 62: neat fabric, both cured resins (resin blend **1** and industry benchmark) and both CFRP laminates. This showed the fibre weight fraction was the same for both laminates with same weight percentage of residual mass corresponding to the fibre in each case (~64 %). The small dip noted in the TGA thermogram of the dry fibre corresponds to the loss of mass from the polyester thread, used to stitch the NCF fabric together.
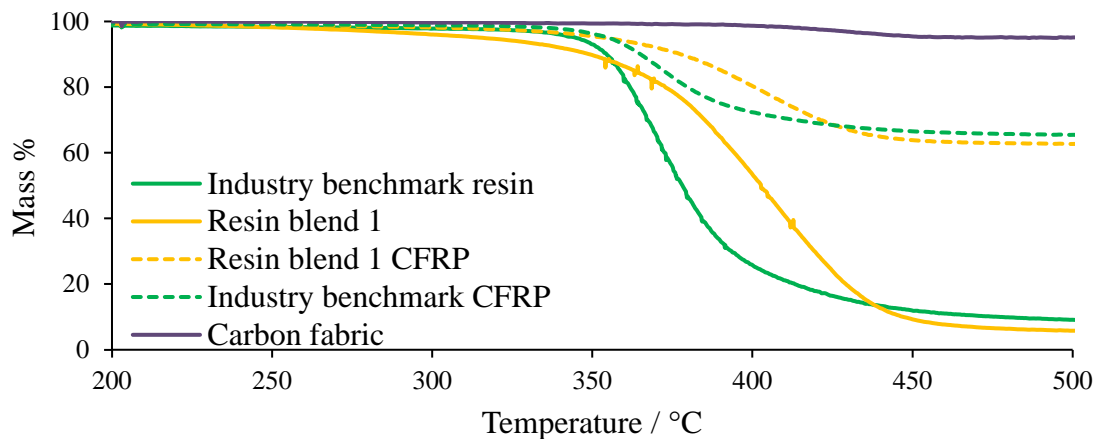
Figure 62: TGA analysis of neat resins (resin blend **1** and industry benchmark), carbon fabric and CFRP laminates to assess weight percentage of fibre.

Optical micrographs were obtained for potted samples taken from both laminates (potted in two-part epoxy resin, cured, and subsequently polished), shown in Figure 63. From the optical micrographs, no measurable voids were observed.

As the laminate quality was comparable between both laminates the ILSS results are deemed to be reliable and show that the anhydride-cured resin (resin blend **1**) offers significant improvement in interlaminar shear over the industry benchmark. The improvement in interfacial adhesion was to be probed further using the micromechanical technique of microbond testing.
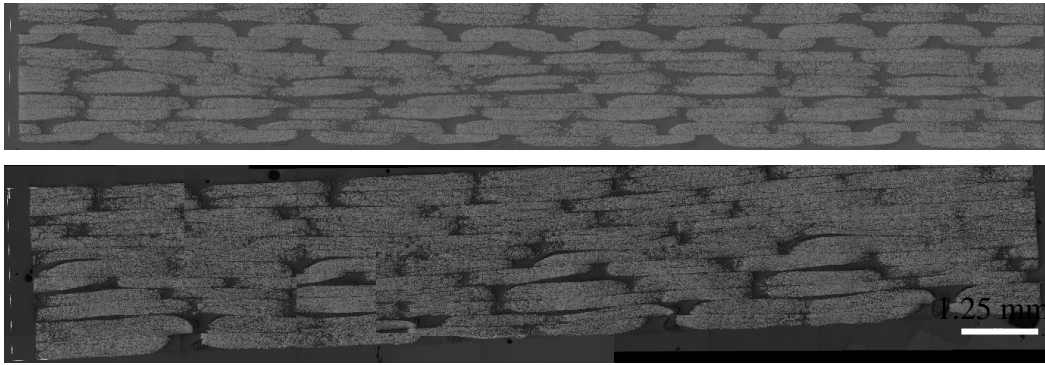
Figure 63: Optical micrographs of CFRP laminates: resin blend **1** (top), industry benchmark resin (bottom).

6.2.4.2. Microbond testing

HCCL have not yet selected a carbon fibre fabric to use for WTBs. By evaluating the IFSS of the resins on carbon fibre, greater understanding of the interface could be obtained, and work could be undertaken to optimise the fibre sizing agents/surface treatments to enhance the interfacial properties for the anhydride-cured epoxy resin. HCCL would then be able to use this to inform selection of an appropriate carbon fibre fabric.

Initial testing was conducted on unsized carbon fibres supplied by Carbon Nexus at Deakin University, Australia [64]. Had the microbond test worked well then carbon fibres with a range of different sizings/surface treatments would have been evaluated.

However, the setup proved to be much more temperamental with carbon fibres. This was due to carbon fibres being much thinner and more delicate, approximately 7 µm compared to 17 µm (glass fibres used in Section 6.2.3). To separate one fibre from the tow a small piece of masking tape was attached to one end of the fibre and used to gently pull it from the tow. The other end was then taped, the tape was used to move the fibre to the silicone mould and to pull it taught across the end tabs as had been done for the preparation of glass fibre microbond samples. Once aligned in the mould, the fibre was fixed in place using the UV-cured adhesive, as described in Section 6.2.3.

Initially droplets were applied in same manner as had been used for the preparation of glass fibre microbond samples, however the droplets were too large (embedment length approximately 300 µm) and leading to fibre breakage in early trials. From literature it is reported that embedment lengths 60-120 µm were desirable [239]. To achieve these

embedment lengths, it was found that using a single carbon fibre attached to a glass pipette was most reliable. In practise it was best to do this under a bright light to observe the droplets being applied to the fibre surface.

In the same manner as used for glass fibre microbond testing, the droplets were cured using the prescribed cure cycle, for these initial tests resin blend **1** was used. Once cured the droplet size parameters were measured under an optical microscope. Droplets of the desired size were achieved (60-120 µm), as shown in Figure 64.
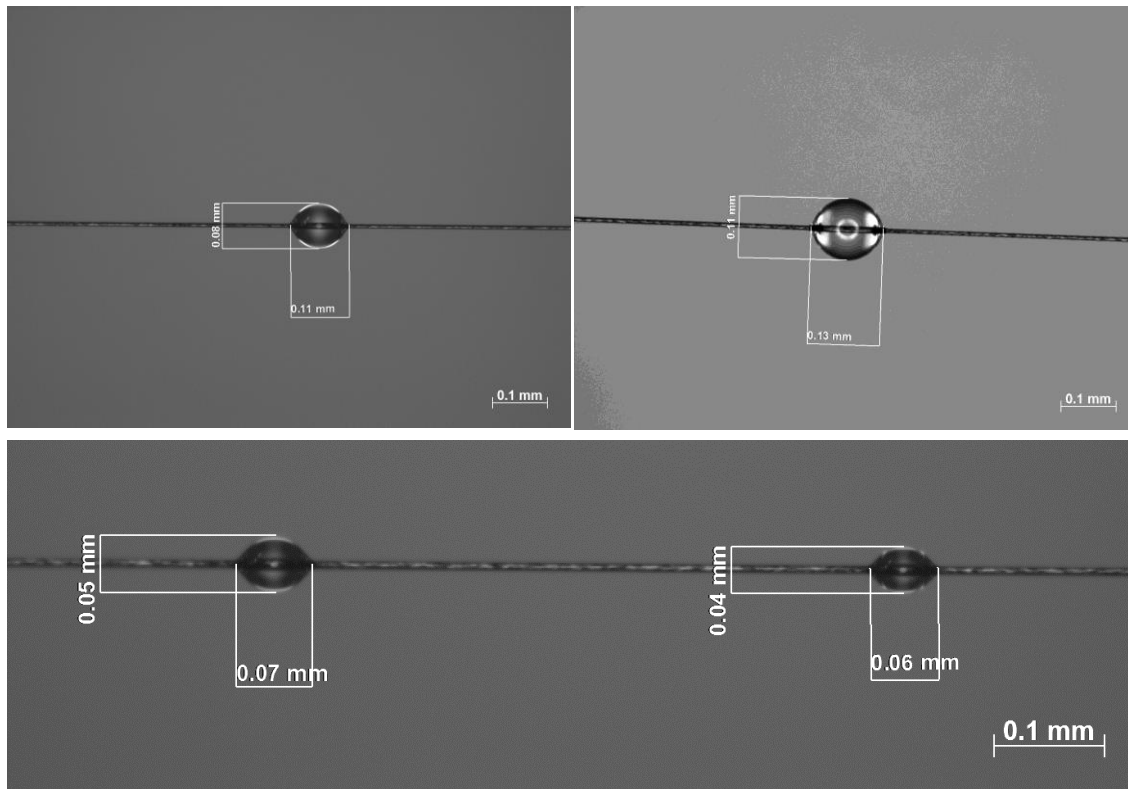
Figure 64: Droplet sizing for microbond testing of resin blend **1** on unsized carbon fibre.

Literature showed that slower displacement rates should be used when testing carbon fibre compared to glass fibre, due to its brittle nature [173]. Hence a displacement rate of 0.002 mm s^{-1} was used.

Even after establishing a method to enable droplets with small embedment lengths to be obtained, the microbond testing still proved to be difficult using the current microbond test setup, hence no useable data was obtained. The smallest microvise that was able to be machined was 9 µm. However, as shown in Figure 65, the microvise edge was not as

precise as had been achieved at larger gap sizes, its burred and rough edges were observed with SEM.
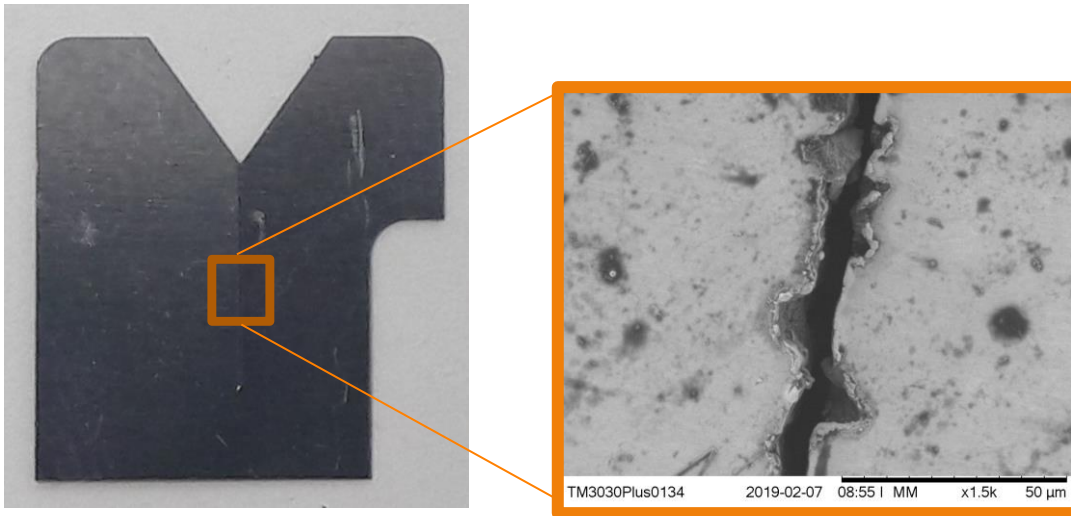
Figure 65: Photograph and SEM micrograph of the 9 µm microvise.

It is hypothesised that this burring caused non-symmetrical loading of the droplet as it was pushed by the microvise, thereby causing stress concentrations which lead to fibre failure rather than interfacial debonding.

Due to project time constraints, IFSS testing of the resins on carbon fibre was suspended. Section 8.2 outlines possible improvements to the current setup which could be made to enable this testing to be conducted.

6.3. Summary

It has been shown that for both glass and carbon fibre systems the anhydride-cured epoxy resin has improved interlaminar properties over the amine-cured industry benchmark, as determined by short beam shear testing.

Microbond testing was used to assess the IFSS. The anhydride-cured resin blend **1** had a 40% increase over the amine-cured Prime^{TM} 20LV resin. Unfortunately, the industry benchmark could not be directly assessed as the resin did not cure. Further work would look to assess different cure cycles to allow for microbond testing or testing *via* different means *i.e.* single fibre fragmentation.

Further to this, the effect of the anhydride structure of the interfacial properties was examined. Resin blends **1** and **2** which are very similar in chemistry display very similar

results in both ILSS and IFSS tests. However, the anhydride in resin blend **3** is much bulkier and is seen to have lower adhesion to the fibre, as this sterically bulky group may prevent the bonding of the resin to the fibre, yet still shows improvement over the amine-cured industry benchmark.

This improvement of the IFSS over the amine-cured Prime^{TM} 20LV by the anhydride-cured systems was hypothesised to be due to increased polarity of the resin due to the presence of the carbonyl groups of the anhydride structures. These groups can react with the hydroxyl groups on the glass fibre surface, thus increasing number of possible bonding locations over the amine-cured counterpart, hence the improved interfacial performance.

To assess if the improvement in interfacial properties translated to carbon fibre some preliminary investigations were conducted for resin blend **1** and the industry benchmark resins. From ILSS the anhydride-cured resin blend **1** showed a 32% increase over the industry benchmark. Thus, indicating that even with traditional epoxy sizings the anhydride-cured resins offers improved interfacial adhesion. However further probing of the interfacial adhesion *via* microbond testing was not achieved due to issues with the setup. This forms part of the future work and will be discussed in Chapter 8. If a method could be established to evaluate the IFSS then the effect of sizing agents could be explored to optimise the carbon fibre for the resin system further.

7 OPTIMISED CURING OF THICK COMPOSITE SECTIONS - VASCULAR CURING

As discussed in Section 2.5, the curing of thick composite parts offers a manufacturing challenge. To overcome this, wind turbine manufactures currently opt for long low temperature cure cycles to mitigate exothermic reactions and to ensure cure homogeneity throughout the part. The author highlighted in Section 2.5.1, several methods have been explored in literature to mitigate this issue.

Previous work at the University of Bristol, modelled vascular networks as a method for optimising the cure of thick composite sections, reducing the peak exotherm and decreasing the cure variance through thickness. In that work using finite element analysis (FEA) modelling, O'Donnell *et al.* [137], showed that embedding a vascule within a composite laminate improved cure homogeneity, as discussed in Section 2.5.1.2.

Interestingly, in civil engineering vascular curing is well established, known in this industry as pipe cooling. The construction of the Hoover Dam in 1931 utilised a network of pipes through which cold water was pumped during the cure of the concrete blocks. In this setup the vascular network enabled removal of excess heat as the concrete cured, thus reducing residual stresses [240].

In the current work, an experimental setup was developed to enable experimental validation of models: FEA and FDA simulations (*N.B.* the FDA simulation was conducted by Dr M. O'Donnell, University of Bristol) to assess the effectiveness of the vascules in curing thick composite sections. The FDA simulation due to its increased

computational efficiency was used to determine an optimised temperature programme for the vascule which was experimentally validated.

The work presented herein has contributed to a journal submission written in collaboration with M. P O'Donnell *et al.* which is currently under review and awaiting publication [241].

7.1. Development of laboratory setup

It was imperative to develop a laboratory setup which could be used in these preliminary investigations. The initial idea of the lab setup is shown Figure 66: it incorporated a circulator, which was used to pump silicone oil at a controlled temperature around a network of pipes (including the vascule/s). For early trials with polydimethylsiloxane (PDMS) an aluminium mould was manufactured to hold the vascules in place at the midplane of the silicone block.
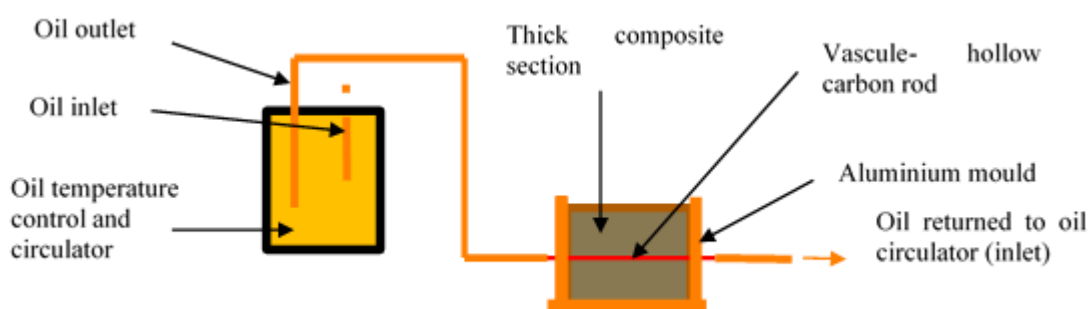
Figure 66: Schematic of the vascular cure laboratory scale setup.

In a previous study at the University of Bristol a setup utilising a peristaltic pump was used [242], but the pump was found to be insufficient as it had a very small volumetric flow rate (variable from 0.023-0.042 mL min^{-1} depending on voltage) thus making the system thermally inefficient.

To mitigate this issue, different alternatives were investigated and the most appropriate was determined to be a heating circulator (CC-202C model, Huber), which had the capacity to pump oil around an external system at a controlled temperature. The model offered temperature operation from 45-200 °C (with option to maintain lower temperatures of 20 °C and -30 °C with water cooling and refrigeration respectively). The circulator had the capacity to hold 2 L of silicone oil and had maximum delivery flow rate of 27 L min^{-1} and pressure of 0.7 bar. Furthermore, the circulator could be connected

to the SpyLight control system to allow the temperature profile to be monitored and data to be acquired.

To connect the circulator (outlet/inlet barbs require tubing with inner diameter (ID) 8 mm) to the vascules (pultruded carbon fibre rods – OD 4 mm, ID 3mm) a series of polytetrafluoroethylene (PTFE) tubes (maximum operating temperature 260 °C) and brass T-splitters and reducing couplers were used. Silicone self-fusing tape was wrapped around these junctions to help ensure that the system was sealed.

To ensure the thermal losses across the system were minimised the PTFE tubing and connectors were wrapped in calcium-magnesium silicate thermal insulation sheet. This was then wrapped in aluminium foil to insulate the system further and to prevent exposure to the thermal insulation sheet which causes skin irritation when handled. The laboratory scale setup developed is shown in Figure 67, for clarity the picture was taken prior to wrapping with insulating material around the PTFE tubing.
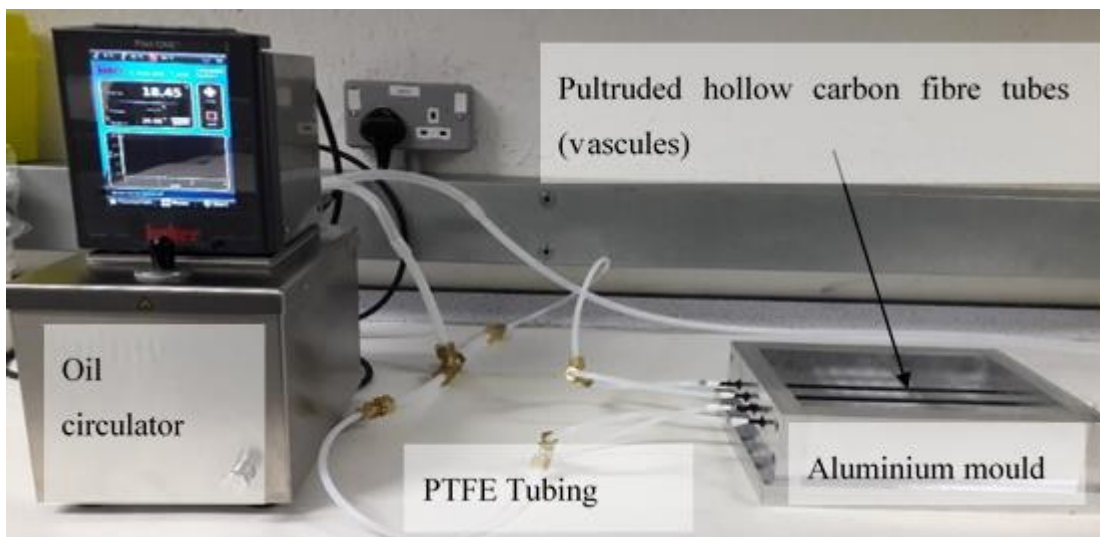
Figure 67: Photograph of the laboratory-scale setup used for the silicone trials.

7.1.1. Assessment for setup for temperature efficiency

To assess the thermal efficiency of the system a thermal camera (FLIR systems Y650sc) was used to monitor the surface temperature of the vascules achieved with set circulator heating profiles. It was found that the temperature of the circulator should be set 15 °C above the desired temperature to mitigate thermal losses.

To ensure the vascule followed the following temperature cycle: 2 °C min⁻¹ ramp to 70 °C, dwell at 70 °C for 90 minutes, cool down to room temperature, the oil circulator was set to reach 85 °C. This is shown in Figure 68.
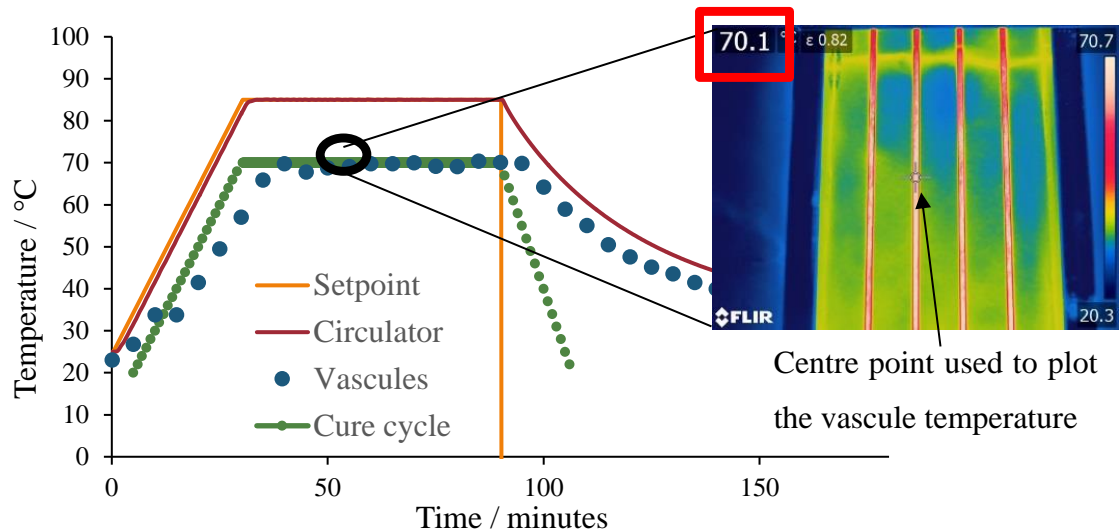
Figure 68: Monitoring the thermal efficiency of the vascule setup.

It was hypothesised the thermal losses were caused in part by the aluminium mould, in which the vascules were held, which acted as large heat sink. Therefore, in all further testing conducted on the laboratory bench in the aluminium mould (silicone trials) the circulator was set 15 °C higher than the desired temperature. However, for the GFRP trials the aluminium mould was not used. The thermal losses were hypothesised to be less as the experiments were conducted in conjunction with oven curing, therefore this compensation factor was not used.

From Figure 68, it was observed that the cool down rate of the silicone oil in the circulator was limited (< 1 °C min⁻¹), as only air circulation was used. The cooling rate of the fan assisted ovens was assessed to ensure the cooling rate of the circulator was comparable. The cooling rate achieved in an air circulated oven was monitored using a thermocouple placed at the centre of the oven as it cooled from 75 °C. This showed that a cooling rate of 0.46 °C min⁻¹ was achieved, thus the cooling offered by the circulator was comparable.

7.2. Silicone trials

Curing of a 60 mm thick silicone section (150 mm x l0 mm) within the aluminium mould was monitored by embedding thermocouples at given locations. A series of experiments were conducted: curing solely with vascules, curing with vascules in conjunction with oven curing, and curing solely with oven (no vascule). Within the section four vascules were used, these were equally spaced across the width of the section.

K-type thermocouples were used to monitor the temperature at eight locations at the central cross-section, the data was recorded using a Pico Technology thermocouple data logger and laptop with Pico Technology software. The circulator and oven were programmed to heat at 2 °C min^{-1} to 70 °C and dwell for 90 minutes before cooling to room temperature, accounting for thermal losses of the vascule setup as noted in Section 7.1.1. In the following figures the line colours represent the thermocouple location as indicated on the graphic of the cross-section in each figure. Note that any position labelled with a cross-through the circle indicates where the thermocouple failed to record data.

Initially the silicone rubber was cured solely using the vascules. The thermocouple data from this experiment are shown in Figure 69.
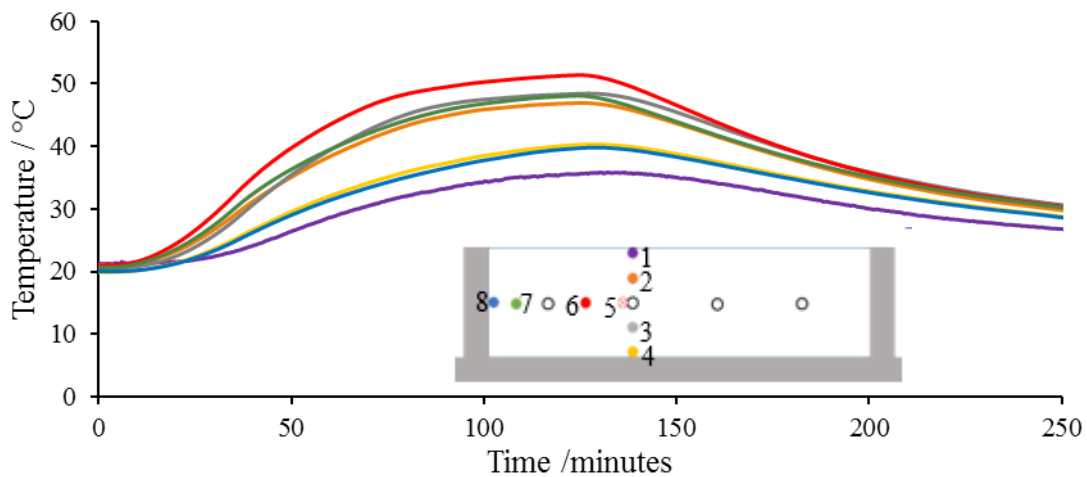
Figure 69: Temperature profile monitoring for curing a 60 mm silicone block using vascular heating. The graphic is not to scale but is indicative of the relative location of the thermocouples within the cross-section at the midplane of the silicone block.

From Figure 69, it is observed that the heat from the vascule radiated uniformly as the thermocouples located a similar distance from a vascule had similar temperature profiles *i.e.* thermocouples (T) placed approximately 30 mm from a vascule and next to the aluminium tooling (T4 and T8) have similar profiles and thermocouples which are 15 mm from a vascule also have similar heat profiles (T2, T3, and T7). As expected, the thermocouple placed 15 mm from two vascules (T6) showed the highest temperature profile and the thermocouple which was placed at the silicone surface and exposed to the ambient air showed the lowest temperature profile (T1).

The maximum temperature observed was 50 °C, which is far from the desired cure temperature. This was because the only heating in this initial benchtop setup came from the vascules themselves and therefore thermal losses to the mould and ambient atmosphere were substantial. To compare the addition of vascules to a realistic scenario, it was imperative that a block of silicone was cured in the oven and in the oven with vascules embedded. Again, in these two scenarios, thermocouples were placed at the same eight locations and the temperature profile measured during the cure.

Figure 70 shows the thermocouple data for the experiment whereby the silicone was cured in the oven (cure cycle: 2 °C min^{-1} to 70 °C, dwell 90 minutes before cooling to room temperature) without the addition of vascules.
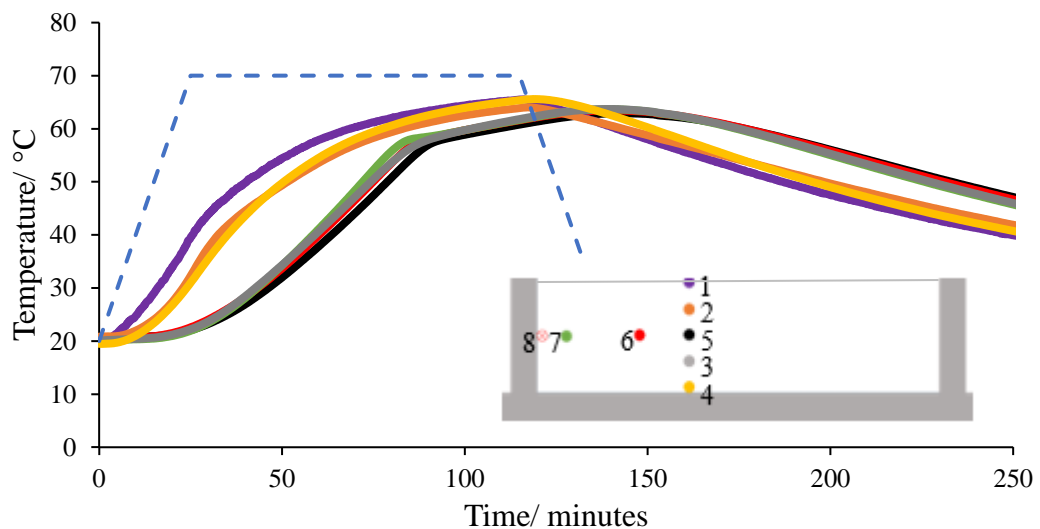
Figure 70: Thermocouple data for oven cured silicone block. Graphic is not to scale but shows relative position of the thermocouples within the silicone cross-section. The dashed blue line represents the programmed oven temperature cycle.

Figure 70, highlights that with oven cure although a higher temperature is reached overall (60 °C) this temperature was only reached just before cooling and therefore there was no dwell observed within the part. In Figure 70, the temperature readings are split into two groups: the thermocouples located near the outer edges have a different heating profile to those located at more central locations. The outer thermocouples are shown to have quicker heating rate than those at internal locations.

Figure 71, shows the thermocouple data for the experiment where vascular curing was used in conjunction with oven curing. The thermocouple data shows that a more uniform cure throughout the thickness of the silicone block was obtained with this setup. The only outlier was the thermocouple which was attached directly to the vascule surface (T5). The other thermocouples showed the same heating profile, whether they were located at the tool surface (30 mm from the vascule) or a smaller 15 mm distance from the vascule.
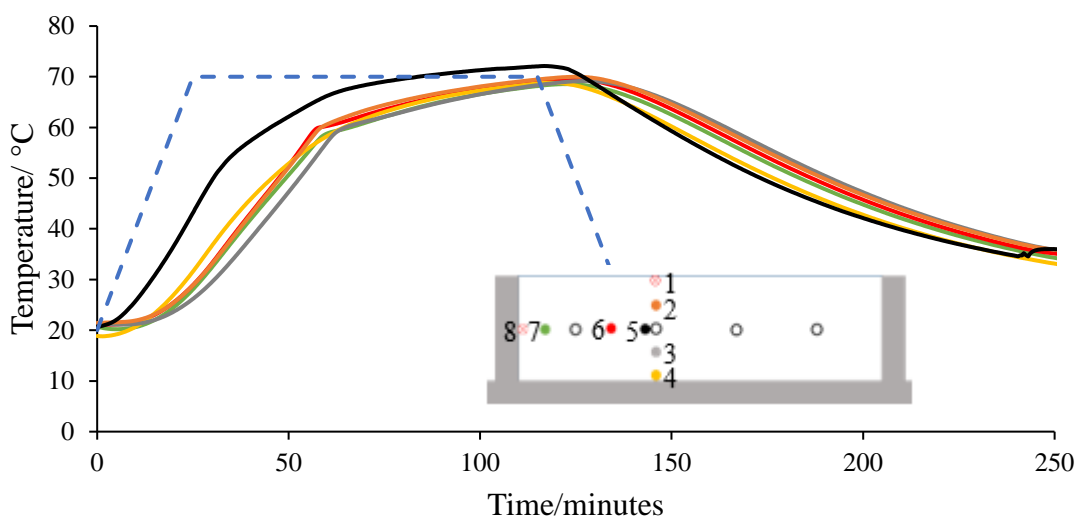
Figure 71: Thermocouple data for the silicone block cured in the oven in conjunction with vascular curing. Graphic shows relative position of the thermocouples within the cross-section of the silicone block, graphic is not to scale. The dashed blue line represents the programmed oven temperature profile.

It was useful to employ silicone for these initial trials to demonstrate an initial proof of concept that, as a secondary heating mechanism, vascules helped to achieve uniform temperature profiles through a thick section, compared to conventional oven curing.

Silicone (PDMS), however, is a lightly crosslinked elastomer so does not display an exothermic curing process of comparable magnitude to thermoset resins, and therefore oversimplifies the issue of curing thick composite sections. During resin cure the exothermic heat generated leads to thermal spiking. These thermal spikes can lead to thermal degradation of the polymer, impacting the mechanical performance of the resulting part. The variation in temperature can lead to differences in the degree of cure, which in turn causes residual stresses to be locked within the cured resin. As highlighted in Section 2.5, this can cause defects such as warpage and delamination, which reduce the mechanical performance of the laminate.

The next phase of the preliminary investigation assessed how the vascules perform when embedded within a thick composite section.

7.3.   Curing of 50 mm thick GFRP laminates

This section will outline how a 2D finite element analysis (FEA) model was constructed and the experimental setup used. The results from both, were compared to enable the experimental validation of the model. The effectiveness of the vascules was assessed by monitoring the internal temperature (and thereby degree of cure) in two configurations: without vascules and with a single vascule located at the centre of the laminate. These were both assessed for 50 mm thick composite blocks (100 mm x 100 mm).

7.3.1.   Finite element analysis (FEA)

Two FEA models were created in ABAQUS, one with and one without a central vascule, these models simulated the development of cure and the heat flow generated due to exothermic nature of the reaction. The model used the HETVAL subroutine, coded in Fortran, to output the heat flux at each time frequency step.

7.3.1.1. Methodology

As already discussed, the polymer curing process is exothermic as energy is released as the crosslinked network forms. The enthalpy of reaction and cure kinetics have been established in earlier chapters, Chapters 4 and 5 respectively. The heat flux is the flow of energy per unit area per unit time. The subroutine HETVAL output the heat flux during cure (dh/dt) (internal heat generation) and was given by Equation 28.

$$\frac{dh}{dt} = \frac{d\alpha}{dt} \times \rho \, (1 - v_f) \times \Delta H_c \qquad (28)$$

where $d\alpha/dt$ (also referred to as $\dot{\alpha}$) is the rate of the cure reaction as determined from the cure kinetic model, described in Chapter 5; ρ is the uncured resin density, v_f is the fibre volume fraction and ΔH_c is the enthalpy of the cure reaction, determined in Chapter 4.

The Fortran code of the subroutine, given in Appendix A.1, shows how the fibre volume fraction and cure kinetics were accounted for in the FEA model.

The FE model was built using the GUI/CAE interface and during the solution the necessary variables were passed from each integration point (time step) to the subroutine which in turn output the heat flux at each point. A 2D cross-sectional model of a 50 mm x 100 mm section was input. Two models were setup, one with and one without a 5 mm diameter central vascule.

The required material properties were determined in Chapter 4 and are presented again in Table 22.

Table 22: Material property inputs for resin blend **1** and its GFRP laminate used in the FEA model of vascular cure.

Property	Value
Enthalpy of reaction	333.3 J g^{-1}. Determined in Section 4.2.3.
Density	For GFRP laminate: 2.150 g cm^{-3} and for cure resin 1.214 g cm^{-3}. Determined in Section 4.2.8.1.
Specific heat capacity of GFRP at 75 °C	For the cured resin this was shown in Section 4.2.8.2 to be 0.95 J g^{-1} K^{-1}. E-glass has values of specific heat of 0.764 J g^{-1} K^{-1} at 20 °C and 0.958 J g^{-1} K^{-1} at 200 °C assuming linear regression through these points then specific heat capacity at 75 °C can be assumed to be 0.82 J g^{-1} K^{-1}[243]. Using the rule of mixtures this was calculated to be 875 J kg^{-1} K^{-1}.
Thermal conductivity of GFRP at 75 °C	For the cured resin this was determined using laser flash analysis to be 0.118 W m^{-1} K^{-1}, as shown in Section 4.2.8.5. E-glass has a known conductivity of 1 W m^{-1} K^{-1} [243]. Using the rule of mixtures, the conductivity of the composite was determined to be 0.00063 J s^{-1} mm^{-1} K^{-1}.

Temperature profiles were assigned to the geometry boundary conditions. These temperature profiles were determined from the experimental temperatures observed at the laminate top and tool plate surface, obtained from thermocouple readings from the curing of the GFRP laminate with no vascule present, cured with the resin blend **1** cure cycle as prescribed in Section 3.1.1. In the FEA model with a central vascule the surface temperature of the vascule was assumed to match the prescribed cure cycle. Figure 72 shows the temperature profiles used and the surface to which these were applied in the FEA models.

a)   b)
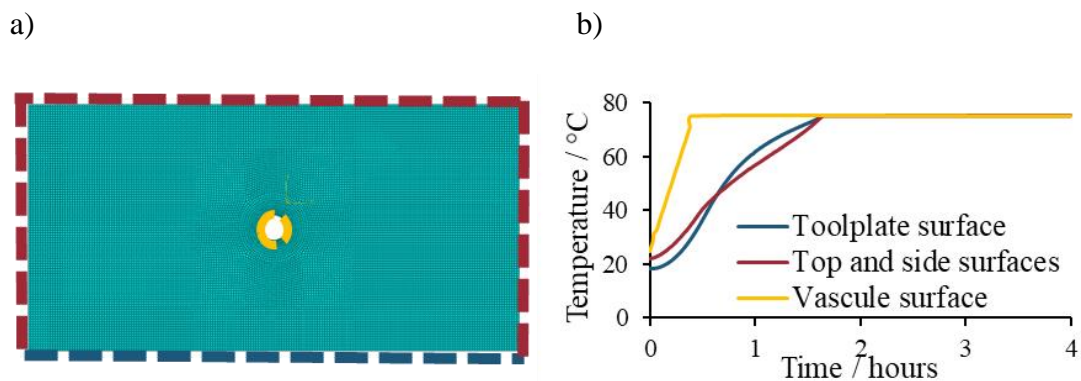
Figure 72: Temperature profiles for the FEA model outer surfaces. a) schematic showing where the temperature boundary conditions were applied, b) temperature profiles shown graphically. *N.B.* Vascule only present in one model but outer boundary temperatures are the same in both models.

The part was meshed using heat transfer elements with approximate global size of 0.5 mm, with quad elements, following a structured meshing technique. To determine the mesh size to use a mesh-convergence study was performed by tracking the degree of cure at a specific time observed at the thermocouple locations as the element size was reduced from 2-0.1 mm. The mesh was considered to be converged when the degree of cure did not vary by more than 1% between the current and previous meshing iteration. For the model with a central vascule, to create elements with quadratic shape the part was sectioned, and certain edges were seeded to help improve uniformity, this sectioning and mesh for both models are shown in Appendix A.2. Once meshed a nodal set was created which matched the location of the thermocouples 1-7 used in the experiments as described in Section 7.3.2.2. The degree of cure and temperature profile at these nodal positions were exported from the FEA model to enable the results to be compared to experimental data.

7.3.2. Experimental

7.3.2.1. Materials

E-glass NCF ±45 fabric was cut into 100 mm x 100 mm squares and laid up to form a preform (140 plies for 50 mm thick sections). Resin blend **1** was the resin selected for these trials and was mixed in ratios given in Section 3.1.1. The preform was infused using the method described in Section 3.3. The infused laminate was cured with the cure cycle prescribed in Section 3.1.1.

The fibre volume fraction was determined in the same manner as described in Section 6.1.1.2 and 6.2.1. The density of E-glass fibre was assumed to be 2.6 g cm^{-3} [243]. The average v_f was calculated to be 57%, using Equations 23-25.

The vascule (if used, was positioned at the centre of the midplane) and thermocouples (in several positions through thickness) were affixed between plies using Evotac spray adhesive. The location of the thermocouples is detailed in Section 7.3.2.2.

7.3.2.2. Thermocouple locations

Thermocouples were placed between the following plies (numbered from the bottom of the laminate – nearest to the tool plate): 1-2, 25-26, 50-51, 70-71 (also location of vascule), 90-91, 115-116, and 139-140, as shown in Figure 73. As described in Section 7.3.1.1, these locations were matched by the nodal elements of the FEA model (assuming the cured ply thickness (CPT) was 0.36 mm, 140 plies corresponded to 50 mm thick laminate), shown in Appendix A.2.
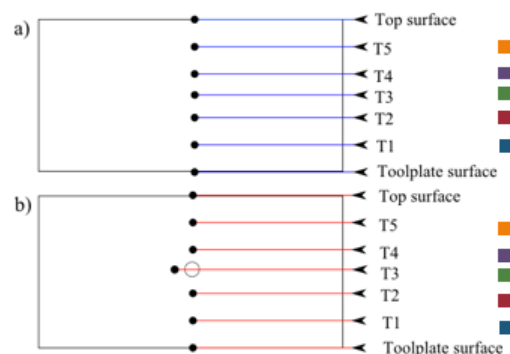
Figure 73: Schematic of the thermocouple positions used both experimentally and in the FEA models: a) without vascule and b) with vascule. *N.B.* The colour of the square corresponds to the key used in all subsequent plots.

124

7.3.2.3. Vascule

Initial silicone trials utilised pultruded carbon rods, however, upon moving to 50 mm thick composite laminates the rods were crushed under the vacuum, thus causing oil to leak into the preform. This failure was due to lack of hoop strength as the material was unidirectional. Consequently, an alternative carbon rod was sourced, which offered improved hoop strength, woven finish carbon fibre tubes were selected (OD 5 mm, ID 3 mm, purchased from EasyComposites). Prior to conducting the following experiments checks on thermal efficiency of system with the new vascules were conducted to ensure the performance matched that of the pultruded carbon rod, which was used in earlier silicone trails described in Section 7.2.

The vascule was embedded at the centre of the midplane, sandwiched between plies 70 and 71, an example of how this appeared in the cured laminate is pictured in Figure 74.

Figure 74: Photograph of sectioned cured GFRP laminate with central vascule.

7.3.3. Results and discussion

Figure 75 shows the temperature plots for the FEA predictions and experimental data for both setups with and without a central vascule. In the experiments it was found at each run at least one thermocouple failed to record useable data, hence only thermocouples T1-5 yielded useable data in these initial experimental runs and therefore were used to compare results in each setup.
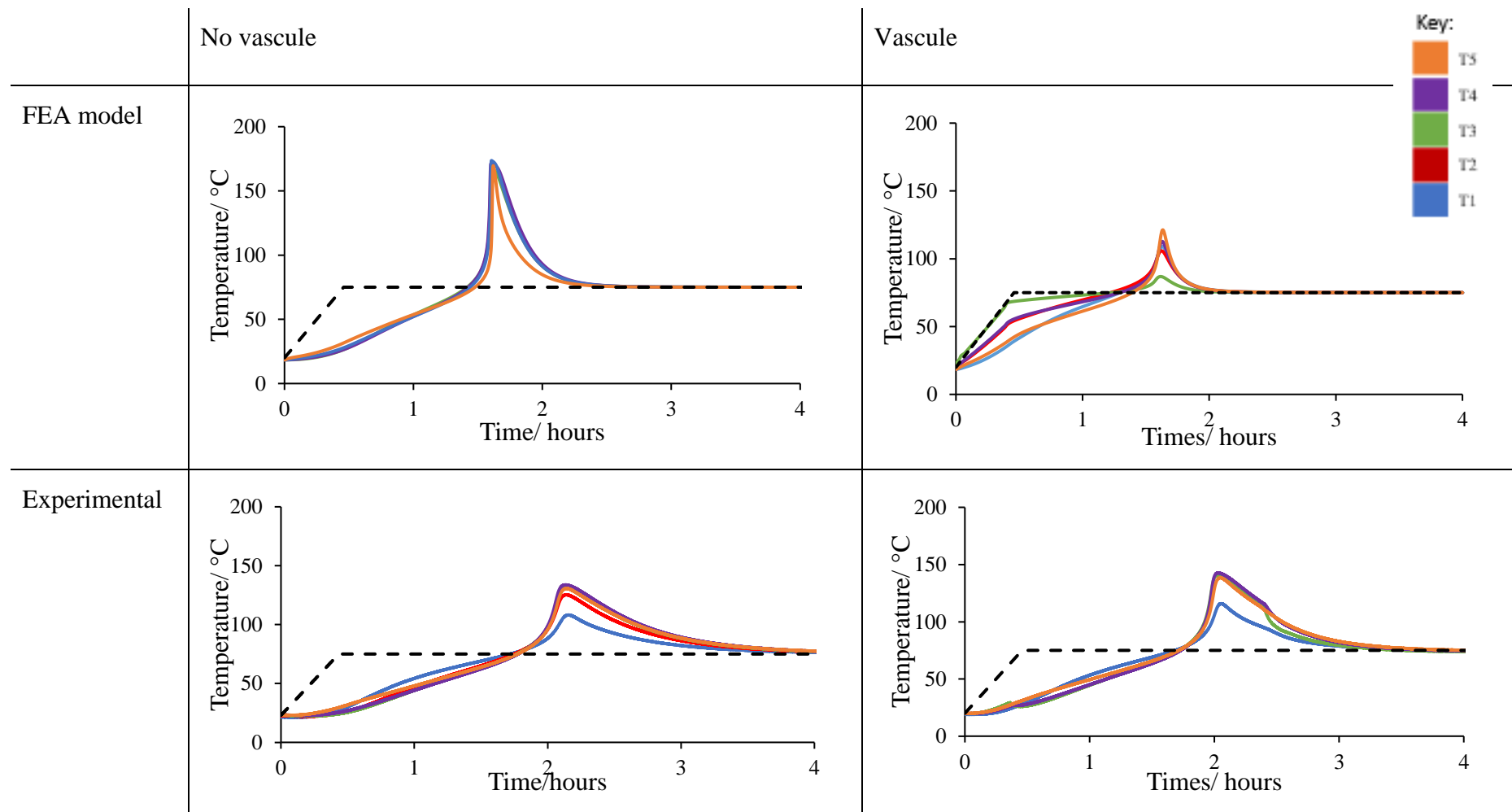
Figure 75: Plots of the temperature profiles observed for the FEA model and experiments with and without vascule. The line colour indicates the thermocouple position as shown in the key in top right-hand corner. The hashed black line indicates the programmed oven cure cycle.
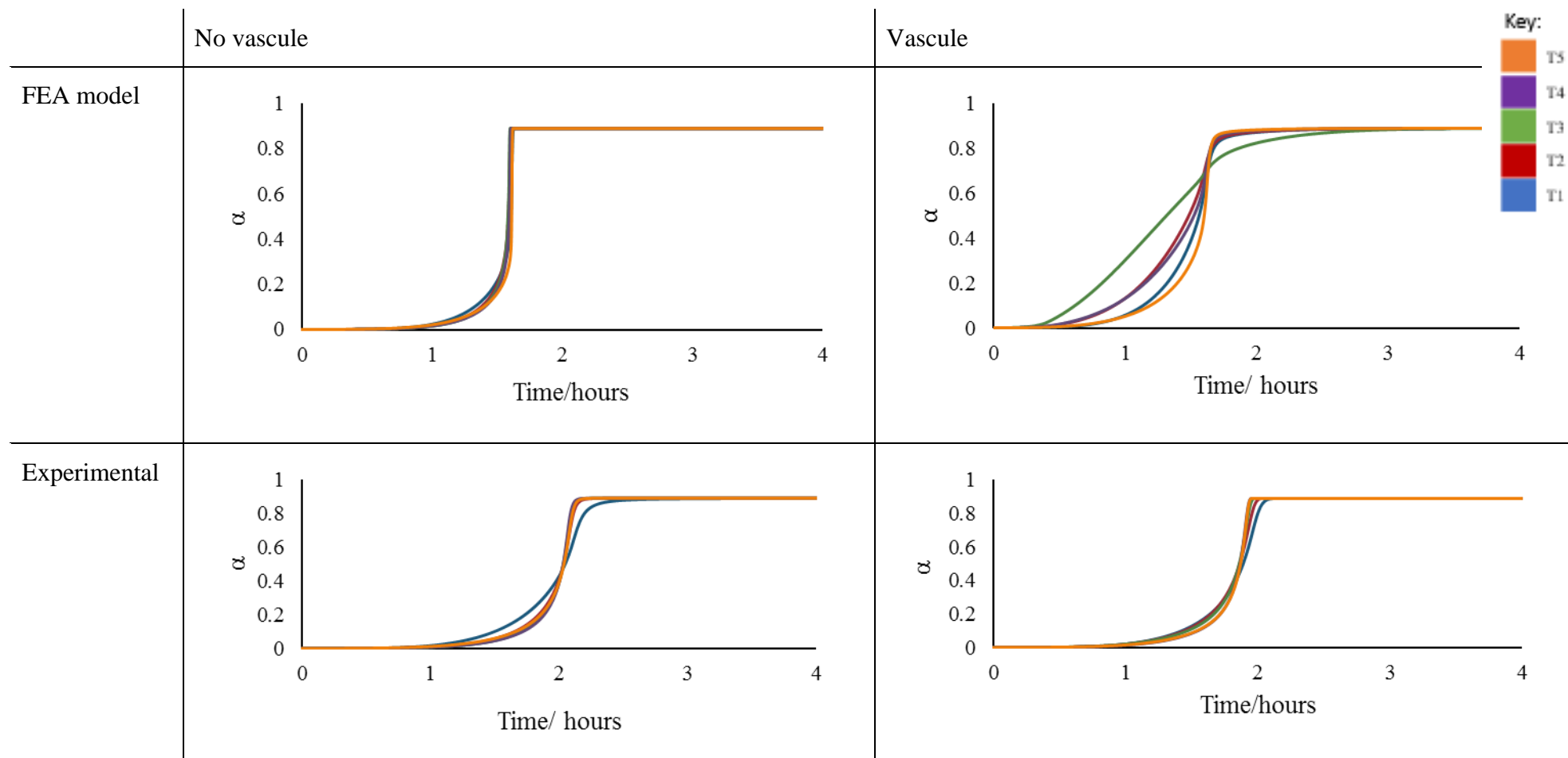
Figure 76: Plots of degree of cure evolution observed in both the FEA model and experimentally for the setups with and without vascule. The line colour indicates the thermocouple position as shown in the key in top right-hand corner.

Using the Karankas cure kinetic model validated in Chapter 5, the thermocouple data obtained experimentally was converted to the degree of cure. In the FEA model the HETVAL subroutine used this cure kinetic model to determine the degree of cure, the data for the nodal positions was exported. Figure 76 presents the FEA predictions and experimental degree of cure evolution over the cure cycle.

Figure 75, shows that the FEA modelled predicted that the addition of the vascule would significantly reduce the maximum temperature observed in the cure. The model showed that the peak temperature would be reduced from 174 °C (configuration with no vascule) to 121 °C (configuration with a central vascule), at the central ply (T3) where the highest peak temperature was observed. A 53 °C reduction in the peak exotherm temperature observed.

Such a dramatic improvement was not observed experimentally when comparing to two configurations. At the central location T3, the observed peak exotherm was reduced from 131 °C to 120 °C, which showed a 11 °C reduction in the peak exotherm temperature. At T2, a greater reduction of 14 °C and at T4 a smaller reduction of 5 °C were noted. Although T2 and T4 are positioned equidistant away from the vascule, the observed temperatures are different, and this is hypothesised to be due to the different boundary conditions *i.e.* tool plate *vs* bagging material.

The smaller reduction in exotherm at T3 compared to the FEA predicted may be due, to the boundary conditions used in the FEA model. The same boundary condition as the top surface was used for the sides. Experimentally these were not equivalent as the sides were surrounded by tacky tape, the thermal profile at these locations should be monitored in future work and used in subsequent models. Another potential reason for the disparity between the model and experimental results may be due to how the vascule was embedded within the laminate. The plies were wrapped over the vascule, which may have created a resin rich pocket at the location of T3 and therefore resulted in higher exotherm compared to the laminate with no vascule present, thus making the improvement of the vascule not as pronounced as would be expected if the embedment method was improved.

Another limitation of the current model was that the thermal conductivity of the composite material was calculated from rules of mixtures using thermal conductivity of the glass fibre and cured resin (Table 22), therefore assuming isotropic material

properties. However, composite materials are inherently anisotropic due to the directionality of the fibres. Heat transfer is most effective along the direction of the fibres [244]. Therefore, within this composite laminate with fibres laid in both 0/90 ° orientations, the heat transfer will be much poorer through thickness. This was not captured within the FEA model and therefore may add to the differences observed between the experimental and simulation results.

Trask *et al*. [245], studied different methods for the embedment of vascules from being laid between plies (as used in the work described thus far) to vascules being nested in pre-cut recesses, shown in Figure 77. However, in the study by Trask much smaller vascule diameters (0.5 mm) compared to the vascules used herein (5 mm). The method currently used will potentially have a resin pockets in the areas where the ply deforms around the vascule, which are likely to impact the mechanical performance of the laminate and therefore further work to establish the best way to embed the vascule within the laminate.
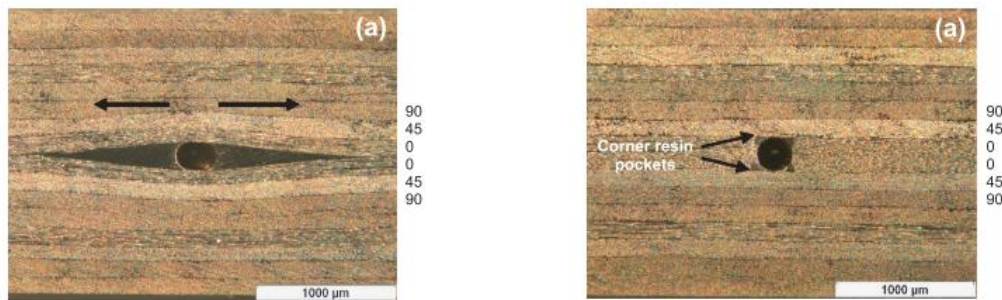
Figure 77: Vascule embedment methods used by Trask *et al.* [245]: a) vascule between plies, b) vascule nested in pre-cut recesses within preform. Taken with permission from [245].

The data from Figures 75 and 76 showed some improvement, but it was hypothesised that if the vascule acted as a thermal sink during the exotherm this would be beneficial as it could draw excess heat away from the composite part. An optimised temperature profile was determined in the following section and trialled experimentally, Section 7.3.4

7.3.3.1. Current limitations of the FEA model

The experimental results clearly showed that some critical parameters are not being captured accurately in the current model predictions and the assumptions made in the model must oversimplify the problem. For example, the exotherm temperature peaks are

much narrower and more symmetrical in the FEA model; the maximum observed temperatures are much higher and the vascule was predicted to have a much greater effect in reducing the peak exotherm. There was also a lag in the experimental data, with the peak exotherm being observed approximately 35 minutes later than in the FEA, this may indicate the system is not as thermally conductive as predicted. This may be due in part to the limitations described with the modelling of the boundary conditions.

It is known that material properties such as density [246], thermal conductivity [247,248] and specific heat capacity [249] vary with degree of cure [250], however owing to time constraints and available equipment, these properties were only assessed for the resin in its cured state. Assessing these time and temperature variable properties will be critical to building a more robust and accurate model in future work.

The FEA model was two-dimensional and therefore simplified the problem as it did not consider the effect of laminate length but assumed constant properties across the plate. This may be true at the central locations but approaching the end of the laminates this condition does not hold true. Future iterations of the model should look to capture the temperature profile of the boundary conditions more accurately. In the current FEA model the top and side temperatures were the same, yet experimentally this would not be the case. In the current setup, the sides were supported by a mould of tacky tape which created the inner bag for infusion, this was not modelled.

7.3.4. Optimised vascular cure

To determine an optimal vascule temperature profile, work was conducted in collaboration with Dr Matthew O' Donnell at the University of Bristol. O'Donnell developed a non-dimensional finite difference analysis (FDA) and optimisation framework in Matlab to determine an optimised thermal profile. Full details of the numerical implementation are given in [241]. By implementing the analysis in Matlab, using meta-heuristic algorithms, the computational costs, associated with FDA analysis and post-processing could be more easily controlled than could be achieved with FEA modelling.

To validate the FDA the results were compared to the FEA model, where the boundary conditions and material inputs are consistent, as described in Sections 7.3.1 and 7.3.2,

therefore the same limitations, as discussed in Section 7.3.3.1, also apply to this model. The results showing that the FDA and FEA are comparable are given in Appendix B.1.

O'Donnell used the FDA simulation to generate an optimised temperature profile for the vascule located at the central location, which was used experimentally as the programme for the oil circulator. In this work the optimisation was conducted with objective to minimise the observed peak temperature. This was conducted as the exothermic peak overshoot could be directly measured within the proof-of-concept laboratory setup and could therefore allow for validation of the model.

The optimised vascule temperature profile was:

- Ramp from 24 °C to 70 °C at 14 °C min^{-1}
- Ramp from 70 °C to 80 °C at 0.17 °C min^{-1}
- Cool to 20 °C at 2.6 °C min^{-1} [*]
- Ramp to 75 °C at 1.05 °C min^{-1}
- Dwell at 75 °C for 560 minutes (remainder of the cure cycle)
- Cool to room temperature (no additional cooling)

[*] As discussed in Section 7, the cooling rate of the circulator was limited. To increase the cooling rate a chiller unit (Huber K6 Kiss) was used to circulate water at 5 °C around the cooling coil in the oil circulator.

A plot of the optimised vascule temperature from the FDA simulation and the achieved temperature profile of the oil circulator when programmed to match the FDA simulation, was given in Figure 78. Overall, the idealised temperature profile was matched by the oil circulator and therefore was used in subsequent vascular cure. However, during the cooling segment, the temperature of 20 °C was not achieved. In future experiments, better control may be achieved if instead of circulating water through the circulator cooling coil, silicone oil was used as this can be cooled to much lower temperatures (approaching -30 °C).

Figure 79, showed the reduction in observed peak temperate was achieved when this optimised vascule temperature profile was used. The optimised vascule temperature profile enabled the vascule to act as a heat sink during the exotherm, drawing the excess heat from the part, thus improving the temperature uniformity through thickness. Unfortunately, in this experiment the thermocouple at the central ply (T3) failed to record data, however, the other internal thermocouples still recorded useable data. The

maximum temperature recorded was at T5 at 108 °C, thus showing a reduction in observed temperature at this location of 22 °C. Significant reductions in the observed peak exotherm were observed at all the internal thermocouples as shown in Table 23.
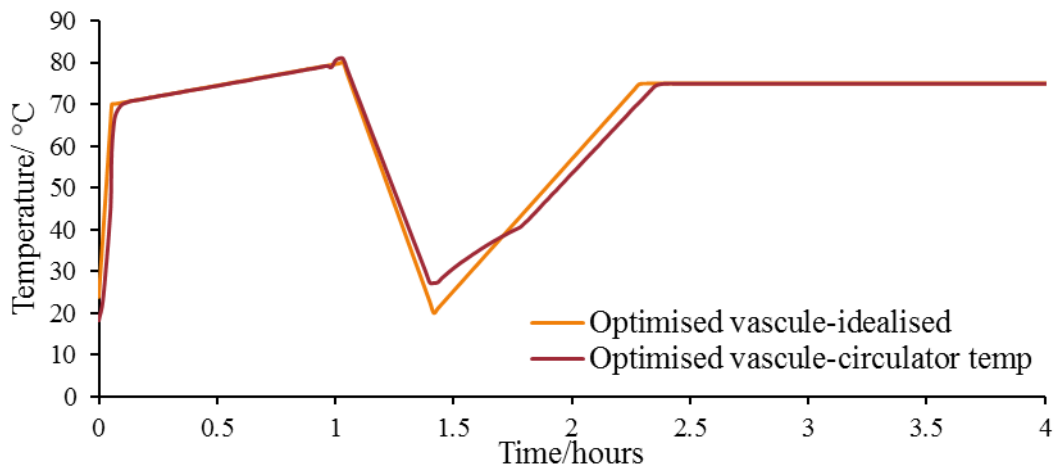
Figure 78: Temperature profiles of the FDA optimised solution and the achieved temperature profile of the circulator during the experiment.

Table 23: Comparison of the thermocouple data for the peak exotherm temperature for the experimental setup without vascule and with the optimised vascule temperature profile.

Thermocouple	Peak temperature observed / °C		Reduction in observed temperature / °C
	No vascule	Optimised vascule	
T1	108	91	17
T2	125	94	31
T4	134	105	29
T5	130	108	22
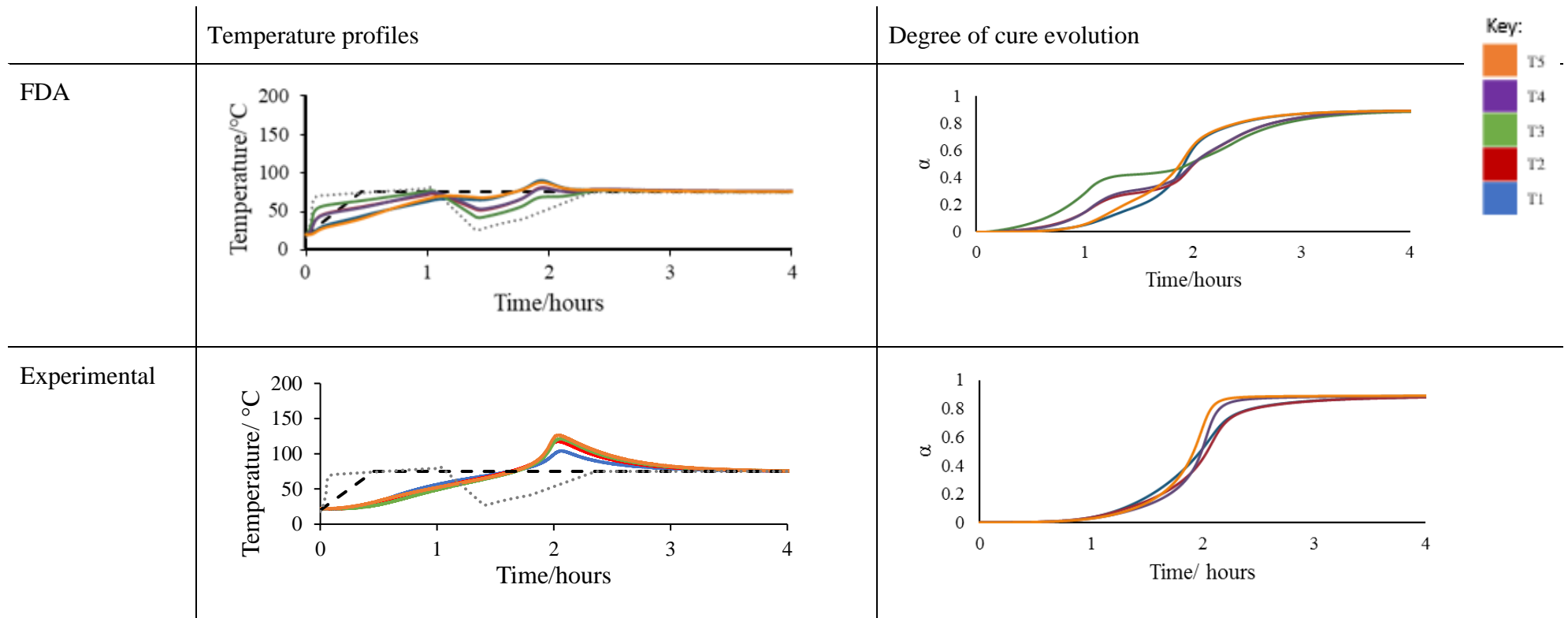
Figure 79: Optimised vascule temperature profile effect on through thickness temperature and degree of cure. The line colour represents the thermocouple position as indicated in the top right hand corner. The hashed black line represents the oven temperature profile and the dotted grey line represents the temperature profile of the vascule.

Figure 80, shows a plot of the rate of degree of cure as a function of cure, this shows that for the optimised vascule experiment there was a much more uniform and controlled rate of reaction over the whole process compared to the setups with (non-optimised) and without vascule.
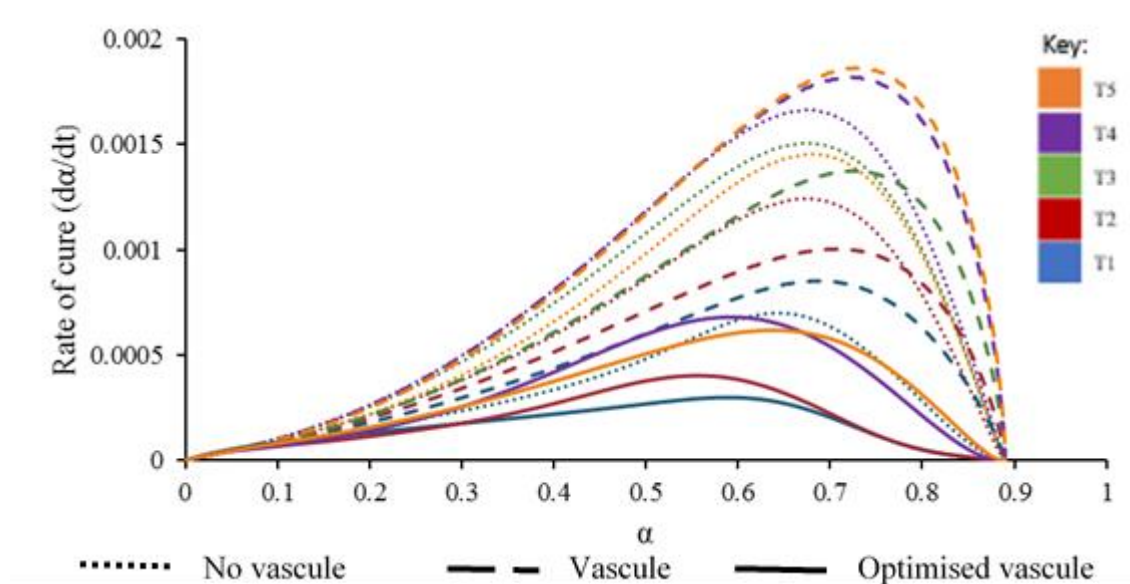
Figure 80: Plot of rate of cure *versus* degree of cure from experimental results. The line colour indicates the thermocouple position as shown in the key in top right-hand corner.

Further to this, O'Donnell has shown that the FDA simulation can conduct optimisation with objective to reduce cure variance and thus improve cure homogeneity. As discussed, it is the uniformity of cure which is most imperative to prevent build-up of residual stresses. And therefore, going forward once the model is refined to accurately capture the behaviour observed, would be the most appropriate optimisation objective.

The simulation showed that increasing the number of vascules can yet further enhance cure uniformity and reduce the peak exotherm. In the FDA model the vascule coordinates were selected to distribute the vascule centres evenly thorough the domain, coordinates as given in Table 24. The coordinate system (X, Y), with value in mm. Hence (0,0) corresponds to bottom left-hand corner of the laminate and (100,50) to the top right-hand corner, of the 2D modelled section. The model did not account for the asymmetry observed due to different boundary conditions (toolplate *versus* top surface), therefore further work could be conducted to allow for vascule placement to be optimised further. A single central vascule led to the prediction

of a reduction in cure variance of 13% yet increasing to two vascules led to further reduction of 61%. With the current geometry, adding more vascules gave negligible improvement in the cure variance [241].

Table 24: Showing the cure variance improving over the baseline system (no vascule) with increasing the number of vascules [241].

Vascule number	Vascule position (mm)	Cure variance improvement (%)
0	-	-
1	(50,25)	13
2	(33,25), (67,25)	61
4	(33,17), (33,33), (67,17), (67,33)	63

7.4.   Summary

The results of the FEA and FDA simulations and the preliminary experiments demonstrate that the inclusion of vascules within a GFRP laminate, in conjunction with oven curing did reduce the peak exotherm observed. This also showed an improvement in the cure variance was obtained, this is predicted to reduce further with increasing the number of vascules beyond one. Reducing the variation and increasing the uniformity of the cure through the laminate thickness is hypothesised to reduce the residual stresses locked within the laminate and therefore improve the quality of the resulting part.

In conclusion, the work thus far has shown the potential for vascular curing as a method to allow for optimisation of the cure process, limiting peak exotherm and reducing cure variance. It is hoped that with further development this method will be viable for industrial applications to improve cure homogeneity, increase manufacturing turnover and improve the quality of the resulting part.

8 CONCLUSIONS AND SUGGESTIONS FOR FURTHER WORK

8.1.   Thesis summary

The objectives of the thesis, as outlined in Chapter 1, were to:

- Characterise the anhydride-cured epoxy resins as supplied by HCCL. Assessing the effect of the anhydride structure on the resin properties and comparing these to a commercially available diamine-cured epoxy resin, widely used in the WTB industry.

- Assess the interfacial performance of the anhydride-cured HCCL resins (**1**-**3**) on the glass fibre reinforcement currently used by HCCL. There is a major drive in the WTB to move toward carbon/hybrid composites to build larger more efficient WTBs. Therefore, assessing the anhydride-cured resins on carbon fibres to identify sizings/surface treatments HCCL should look for when selecting a carbon fibre to maximise the composite performance.

- Develop a proof-of-concept experimental setup to demonstrate the technology of vascular curing. This method has previously been shown, through computer simulation, to reduce the cure variance across thick composite parts but had not yet been experimentally verified.

In Chapter 4, the anhydride-cured HCCL epoxy resins were characterised and benchmarked against a diamine-cured resin which is widely used by the WTB industry (Epikote^{TM} resin MGS RIMR035 with Epikure^{TM} curing agent MGS RIMH037). The effect of the anhydride structure upon the resin properties was assessed for the HCCL resin, a DGEBA epoxy cured with a tertiary amine (Ancamine K54) and one of the following anhydrides: a mixture of 3-

and 4-methyl-1,2,3,6-tetrahydrophthalic anhydride (denoted as resin blend **1**), a mixture of 3- and 4-methyl-hexahydrophthalic anhydride (resin blend **2**); or methyl-3,6-endomethylene-1,2,3,6-tetrahydrophthalic anhydride (resin blend **3**).

All the resins showed comparable bulk viscosities, gel times, and moduli (below T_g); yet the anhydride-cured epoxies displayed overall higher cured T_g values, compared to the diamine-cured resins. The resulting retention in modulus over a wider temperature range and their higher char yields, lead to higher operating temperatures. The anhydride-cured epoxies also displayed lower enthalpies of reaction (on average 300 J g^{-1}) *versus* the diamine cured industry benchmark (377 J g^{-1}). Having a lower reaction enthalpy is beneficial as this would result in reduced exothermic reaction and thus should reduce peak exothermic temperature observed during cure and therefore reduce thermal gradients in the thick composite parts that are commonly encountered in WTBs.

From an assessment of the structure-property relationship of the anhydrides, the main difference observed was that the cured resin blend **3** displayed a higher char yield (14%) compared to resin blends **1** and **2**. This was attributed to the inclusion of the norborene moiety, which can undergo a thermally initiated retro-Diels Alder reaction accompanied by crosslinking. Although not required for applications involving WTBs, this increased thermal performance may make this resin an attractive possibility for other applications.

The experimental work undertaken to characterise the interfacial adhesion of the resins was presented in Chapter 6. Firstly, the macromechanical testing was conducted by short beam shear testing of infused glass fibre laminates. This showed that resin blend **1** displayed a 18% improvement in ILSS over the diamine-cured industry benchmark. The interfacial adhesion was then probed further by examining the interface with a micromechanical (microbond) test, to determine the IFSS of the resins on the same glass fibre. However, owing to difficulties with curing of the benchmark resin in the droplet form required, another diamine-cured standard resin (Prime^{TM} 20LV) was used to benchmark the anhydride resins against. Compared to Prime^{TM} 20LV, the anhydride cured resins showed significant improvements in IFSS, with 66% improvement shown for resin blend **1**. This improvement in interfacial properties is attributed to the presence of the carbonyl groups in the anhydride structures. These groups can also react the hydroxyl groups on the glass fibre surface, thus increasing number of possible bonding locations thus improving the adhesion at the fibre interface. In contrast the diamine-cured counterpart does not have these additional groups to interact with the hydroxyl groups at the fibre surface and relies solely on the reactive groups in the epoxy.

Resin blend **3** shows the lowest IFSS of the anhydride-cured epoxies studied and this is attributed to the anhydride being bulkier than the other two anhydrides and the steric hinderance reduces the resin's ability to bond to the fibre surface.

The improvement in interfacial adhesion observed in this study highlights more positive attributes of these resins systems which make them attractive to the WTB industry, as improved interfacial adhesion leads to improved mechanical performance as the resin can more effectively transfer stress between fibres.

Resin blend **1** was assessed as having the best balance of resin and interfacial properties on glass fibre and consequently, this blend was used exclusively to assess the interfacial adhesion with carbon fibre and for the study on vascular curing. To have material inputs for the FEA model used in the vascule cure setup, further resin characterisation was conducted solely on resin blend **1**, including a more rigorous assessment of the resin cure kinetics and determination of its thermal conductivity.

The interfacial performance of both resin blend **1** and the industry benchmark on carbon fibre were further examined in Chapter 6. Initially macromechanical testing of the resins was conducted on an industry standard carbon fibre for which a standard sizing suitable for use with epoxy resins in used, although its actual nature is proprietary. The ILSS of resin blend **1** was shown to be 75 MPa compared to 57 MPa for the industry benchmark, that this resin shows greatly enhanced interlaminar performance. Unfortunately, owing to setup issues the IFSS of the anhydride resin on various carbon fibres with different sizings/ surface treatments could not be conducted. Consequently, it was not possible to identify the most appropriate carbon fibre sizing to be used by HCCL in their development of carbon/hybrid WTBs. However, the increase in interlaminar performance does show great potential for these anhydride-cured epoxies in CFRPs, as with standard sizing/surface treatments used, there was already an improvement in interfacial adhesion.

In Chapter 7, a vascular cure experimental setup was developed to demonstrate the method as a proof-of-concept curing method for thick composite parts. A series of setup trials undertaken to assess the oil circulator for its temperature efficiency and heating/cooling rate capabilities. Preliminary experiments were conducted on 50 mm thick sections, with and without a central vascule. In the experiments with a vascule two heating profiles were examined in combination with the oven curing, heat profile which matched the current cure cycle used in the oven (ramp 2 °C min^{-1} to 75 °C, dwell at 75 °C for 12 hours) and an optimised heating profile as

determined from a FDA computer simulation (which had a heat-cool-heat cycle, whereby the oil circulated was cooled when the resin was undergoing the exothermic cure reaction). These preliminary results demonstrated the ability of the vascule to improve cure homogeneity, the optimise vascule profile showed that a reduced the observed peak exotherm on average by 25 °C was achieved.

8.2. Suggestions for further work

Although the potential for these anhydride-cured resins to offer increased interfacial adhesion and optimised cure with the vascular cure setup has been demonstrated. Further work can be undertaken to showcase the full potential of the resin and processing method. This section will provide the framework for some recommendations for further work.

8.2.1. Resin development

From the work undertaken it was clear the anhydride-cured epoxies demonstrated the ability to match the industry benchmark in terms of thermal and mechanical properties and even showed much greater interfacial adhesion and lower reaction enthalpy, confirming that it has favourable properties for its application to WTBs. However, during this work two further considerations were identified but not explored as they fell beyond the scope of the current project, *i.e.* water uptake and fracture toughness.

It is known that anhydrides are susceptible to moisture ingress and as wind turbines are exposed to harsh conditions in use it is vital that this should be mitigated. This thesis reported a very simple test whereby cured resin samples of resin blend **1** and the industry benchmark were submerged in deionised water (temperature maintained at 50 °C) for a period of 42 days. The masses of the samples were recorded at regular intervals and the moisture absorption of the samples was determined. This simple test showed that per millimetre thickness, resin blend **1** gained 2.6 % mass increase compared to the diamine-cured industry benchmark which gained 0.9% weight. The impact of the moisture absorption on the T_g of resin blend **1** was assessed *via* DSC analysis and showed a drop of 20 °C.

It is well understood that moisture ingress causes a reduction in mechanical performance. In the WTB manufacturing processes blades are invariably coated with *e.g.* polyurethane to prevent moisture ingress. Further work might look to assess whether these coatings offer a sufficiently high degree of hydrophobicity for anhydride-cured resins. If they are not sufficient then further work could look to optimise the hydrophobic coating used for

anhydride-cured epoxy composite WTBs, some of which have already been highlighted in literature. Additives can be added to prevent moisture ingress, and one such example are polyhedral oligomeric silsesquioxane (POSS) reagents, which have been reported to reduce moisture ingress in other anhydride-cured epoxies. POSS reagents may be tailored for their reactivity by selection of different functional groups ensuring that they become bound covalently to the resin. For resins produced by VARI methods, it is important that such additives do not increase the resins viscosity and are not filtered out during the infusion process. Further work could look to assess the current state-of -the-art additives or surface coatings which could mitigate moisture ingress or could look to develop novel additives perhaps where additives are bound to the fibre and thus reduce issues associated with infusion. Assessing the impact of moisture ingress upon the mechanical performance would also be critical to this work.

From the short beam shear tests although the anhydride-cured resin demonstrates clear advantage in offering improved interfacial adhesion. However, it was observed that the failure was much more brittle than observed for the diamine-cured industry benchmark which showed a more progressive failure. It is thought this could indicate the anhydride-cured epoxies resin have lower fracture toughness. Many additives are discussed in literature which have been shown to improve fracture toughness such as thermoplastic particles and graphene nanoplatelets. The issues of increasing resin viscosity and filtering of the additives during infusion should still be considered when assessing use of these additives and may prevent their use in this application. However, hyperbranched polymers (HBPs) have been shown in literature to increase fracture toughness, yet they are a liquid additive that undergoes phase separation during cure thus does not have the issues. It would be the authors recommendation to assess HBPs as a means of toughening the anhydride-cured epoxies evaluated in this work. Resin fracture toughness can be assessed using ASTM D5045- Plane-Strain Fracture Toughness, to determine K_{1c}.

For both these resin development areas identified if additives are added to the resin or fibre it will be critical to assess the effect of these upon the interfacial properties between the resin and fibre. As discussed, the anhydride-cured epoxies studied here display greater interfacial adhesion makes them favourable for use more widely in the WTB industry. It would be imperative that the inclusion of any additive did not significantly reduce its interfacial performance.

8.2.2. Interfacial adhesion on carbon fibre

The microbond technique used to characterise the IFSS of the anhydride-cured epoxy resins on glass fibre seemed to work well, but on moving to carbon fibres the current setup was not ideal. Instead of shearing the droplet from the fibre surface, the fibre itself broke even though very small resin droplet sizes (embedded lengths 60-120 µm) were achieved and the size was in line with those reported in literature. On examination of the microvise under SEM, rugged edges and surface burring were observed, this was hypothesised to have been causing an uneven loading on the resin droplet and thus leading to fibre failure. It would therefore be recommended that the setup be modified in one of two ways to eliminate this issue:

- New manufacturing method of microvise to be used- perhaps a different technique could be used which does not cause high temperatures to be seen at the metal surface and thus prevents burring.
- In literature many of the examples of microbond use two blades which are on a micrometre to control the spacing between the blade edges. Potentially moving away from the setup currently used could enable finer fibres to be examined.

Microbond testing was used as the microbond tester setup was available at the University of Bristol and the method was identified of being simple to setup. However, one of the other methods for determination of IFSS such as single fibre fragmentation or single fibre pull out could be explored.

If other methods were established, then this could also be used to assess the IFSS of the industry benchmark resin on glass fibres to for comparison to the anhydride-cured resins. In the current work issues with curing of droplets of the industry benchmark were observed and hence another diamine-cured epoxy (Prime^{TM} 20LV) was used.

8.2.3. Vascular curing

This project has led to the development of a proof-of-concept laboratory scale setup (TRL 2) and conducted preliminary testing demonstrating the feasibility and potential of the system. It was shown to reduce significantly the peak exotherm temperature observed at the centre of a 50 mm thick GFRP section. Figure 81, shows a testing framework which could be used to progress the technology through the technology readiness levels (TRLs) to TRL 9 where it would become used operationally in industry [251].

However, this section will suggest work which should be examined initially in order to address methods to improve and optimise the vascule network required to enable a small-scale

prototype to be developed before it could be considered for industrial applications. There are clearly a great many steps required to advance this technology to TRL 9. This section will identify further work which could be conducted in order to enable the development of a small-scale prototype of a wind turbine blade which has been cured with a vascule network located at critical locations (as determined from simulations) and demonstrates an improvement in cure homogeneity with optimised shorter cure cycle with no/negligible impact on mechanical performance (TRL5).

8.2.3.1. Modelling/simulation

In Chapter 7, small differences were observed between the simulation and experimental results, with slight lag in peak exotherm being observed experimentally and the simulation predicting higher peak temperature than seen experimentally. For example, when no vascule is present from FEA simulation the peak exotherm at T4 is predicted to be 171 °C at 1.7 hours into the cure cycle. Yet experimentally the reported peak exotherm is 131 °C, at 2.1 hours into the cure cycle.

This error could be caused by the oversimplification of boundary temperature conditions used in the simulation, with sides given the same temperature profile as the top as determined from experimental thermal data. However, in practise the sides would be more thermally insulated due to the presence of tacky tape. Future work should look to obtain the experimental thermal data at these boundary conditions and assess whether this addresses the small difference observed.

Secondly there has been some simplification of the material properties characterised and used in the model. It is thought that these should be very minor and therefore not drastically alter the prediction, but to increase accuracy they may need to be assessed. The values used for density and thermal conductivity were kept constant at cured resin values. However, these properties do change during cure, and how these properties change during the cure could be modelled and incorporated into the simulation.

In addition, the current model simplifies the problem as it models only a cross section *i.e.* two-dimensional slice of the part. Development of a three-dimensional model might be better able to simulate the evolution of cure as the heat transfer in all directions would be captured. Assessing whether the increased accuracy from using a 3D model is vital if the optimum position can be obtained with 2D model will be critical. Using the model which offers best

accuracy in a reasonable computation time is a compromise and therefore the benefits of moving to more complex models needs to be assessed.

8.2.3.2. Experimental setup

Assessing the effect of embedding the vascules upon the mechanical performance of the composite laminate is critical. It has been reported in literature that vascules used for self-healing applications have a negligible influence on mechanical performance, but it should be noted that those reports used vascules with smaller diameters than those used in this work.

In the current work the aim was to develop a setup which showcased the potential for vascular curing to reduce the observed exotherm and reduce thermal gradients through thick composite sections, which was successfully achieved. However, optimisation of the setup and the impact of the vascule on the mechanical performance of the laminate was not assessed. Here are some considerations which could be assessed in further work:

- <u>Vascule material.</u> In this work a carbon rod was used as these were readily available in small diameter sizes and the use of carbon enabled the impact of increasing weight by its addition to minimised. However, metal rods may enable quicker transfer of heat to and from the composite during cure. The interaction between the rod and resin and the interface between them may be critical to the mechanical performance and therefore this may need to be characterised and methods to improve the interface could be examined.

- <u>Vascule size</u>. In the current work, vascules with OD 5 mm and ID 3 mm were used to minimise issues of back pressure on the oil circulator. However further work could look to determine the minimum diameter which does not create too much back pressure to impact the performance of the circulator. Assessing the optimum vascule diameter to minimise impact on mechanical performance, still enable efficient heat transfer to composite and to enable efficient circulation of oil through vascule network will be required.

- <u>Embedment technique.</u> In the current work the central plies were wrapped around the vascule, but this was observed to create resin pockets at the side of the vascule. It may be more beneficial to cut the plies so the vascule sits in a cavity within the composite. This may favour square profiled vascules which could also be examined.

Once the work has been conducted in these areas to increase robustness of the simulation model and to assess an optimum vascule setup in terms of embedment technique and vascule

143

size. Then the technology should have progressed to TRL 3. The next phase will look toward scale up with more complex geometries to optimise number and location of vascules within these parts. Further assessment of the impact of the vascule on the manufacture part quality should be assessed to determine if the reduction in observed peak exotherm does reduce the residual stresses locked within the laminate. From this a small-scale prototype can be produced which can be used to showcase the potential for industry (TRL5).
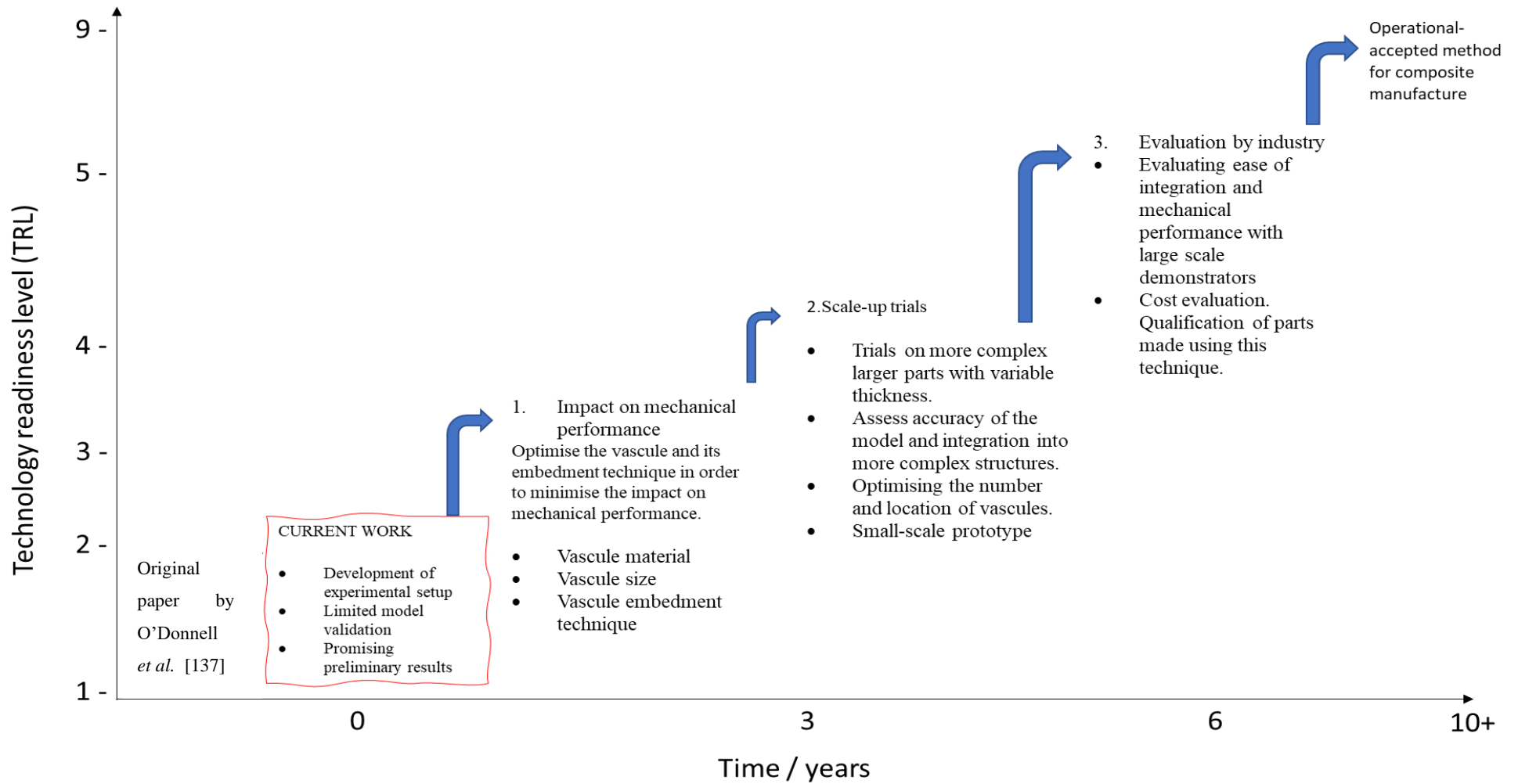
Figure 81: Future work plan for the development of the vascular cure technology.

8.3. Concluding remarks

Overall, the project demonstrated that these anhydride-cured epoxy resins do offer improvements in performance in terms of both material properties and manufacturing. The results of this work show that the anhydride-cured resins developed by HCCL show comparable resin properties in terms of viscosities, time to gel and storage modulus below T_g. The anhydride resins are shown to have higher T_g, by some 20 °C, than the industry benchmark when measured both by DSC and DMA. However, the main benefits over the industry benchmark assessed, are that the resins (**1-3**) all showed higher interfacial adhesion on the glass fibre and displayed lower reaction enthalpies therefore reducing risk of exotherm in thick composite sections.

A full assessment of the resin's interfacial adhesion on carbon fibre and identification of the most appropriate sizings/surface treatments to optimise the interfacial adhesion could not be conducted due to current limitations of the setup available. However, on an industry standard carbon fibre the ILSS of the anhydride-cured resin blend **1** showed a 32% increase over diamine-cured industry benchmark. This indicated that even on standard industry sizing treatments that the anhydride-cured resin offers enhanced interfacial adhesion and suggests its potential to be used on carbon fibre/hybrid composite WTBs.

The vascular curing experimental setup clearly demonstrated the ability of these internal networks to improve cure homogeneity and by reducing the temperature overshoot. This also offers the potential to optimise the cure cycle without incurring penalty of increasing the risk of exotherm. This offers the potential to increase part production rates by reducing cure cycle times and increase part quality by elimination of manufacturing defects caused by thermal gradients and cure variation within the part.

REFERENCES

[1]   R. Cherrington, V. Goodship, J. Meredith, B. M. Wood, S. R. Coles, A. Vuillaume, A. Feito-Boirac, F. Spee, K. Kirwan, Producer responsibility: Defining the incentive for recycling composite wind turbine blades in Europe, Energy Policy, 47, (2012), 13–21.

[2]   Global Wind Energy Council (GWEC), Global Wind Report 2015, 2016. http://www.gwec.net/gobal-figures/wind-energy-globa;-status/ (accessed May 18, 2020).

[3]   L. Mishnaevsky Jr, K. Branner, H. N. Petersen, J. Beauson, M. McGugan, B. F. Sørensen, Materials for wind turbine blades: an overview, *Materials*, 10, (2017), 1–24.

[4]   Hexcel, Propelling the future of renewable energy, (2019). https://www.hexcel.com/News/News-Releases/2941/propelling-the-future-of-renewable-energy (accessed February 22, 2020).

[5]   P. Malnati, J. Sloan, Fast and Faster: rapid-cure resins drive down cycle times, *Composites World*. (2018). https://www.compositesworld.com/articles/fast-and-faster-rapid-cure-epoxies-drive-down-cycle-times (accessed May 18, 2020).

[6]   G. Gardiner, Blade cycle time: 37 percent faster, *Composites World*. (2012). https://www.compositesworld.com/articles/blade-cycle-time-37-percent-faster (accessed May 18, 2020).

[7]   B. Hoevel, A. Sagnard, New materials tackle weight, strength and cure time issues for wind turbine blades, *Reinforced plastics*. Materials Today. (2011). https://www.materialstoday.com/composite-parts/features/new-materials-tackle-weight-strength-and-cure/ (accessed May 18, 2020).

[8]   G. Daun, Cure agents improve rotor production, *Reinforced Plastics,* Materials Today, (2009). https://www.materialstoday.com/composite-applications/features/curing-agents-improve-rotor-production/ (accessed

February 22, 2020).

[9]   P. J. Schubel and R. J. Crossley, Wind turbine blade design review, *Wind Engineering*, 36, **4**, (2012), 365–388.

[10]   T. J. Price, James Blyth – Britain's first modern wind power pioneer, *Wind Engineering*, 29, (1984), 191–200.

[11]   O. Edenhofer, R. Pichs-Madruge, Y. Sokona, K. Seyboth, P. Matschoss, S. Kadner, T. Zwickel, P. Eickmeier, G. Hansern, S. Schlömer, C. von Stechow, eds., Summary for Policymakers. In: IPCC special report on renewable energy resources and climate change mitigation, Cambridge University Press, Cambridge, UK, 2011.

[12]   P. A. Owusu, S. Asumadu-Sarkodie, A review of renewable energy sources, sustainability issues and climate change mitigation, *Cogent Engineering*, 3, (2016), 1–14.

[13]   J. Damota, I. Lamas, A. Couce, J. Rodríguez, Vertical axis wind turbines: current technologies and future trends, *Renew. Energy Power Qual. J.*, 1, **13**, (2017), 530–535.

[14]   P. Tchakoua, R. Wamkeue, M. Ouhrouche, T. A. Tameghe, G. Ekemb, A new approach for modeling darrieus-type vertical axis wind turbine rotors using electrical equivalent circuit analogy: basis of theoretical formulations and model development, *Energies,* 8, (2015).

[15]   C. Seidel, S. Jayaram, L. Kunkel, A. Mackowski, Structural analysis of biologically inspired small wind turbine blades, *Int. J. Mech. Mater. Eng.*, 12 (2017), 1–9.

[16]   P. Brøndsted, H. Lilholt, A. Lystrup, Composite materials for wind power turbine blades, *Annu. Rev. Mater. Res.,* 35, (2005), 505–38.

[17]   S. I. Al-Majed, T. Fujigaki, Wind power generation : an overview, *Modern Electric Power Systems*, (2010), 5–10.

[18]   T. Burton, D. Sharpe, N. Jenkins, E. Bossanyi, WindEnergy Handbook, John Wiley and Sons Ltd., Chichester, UK, 2001.

[19]   S. Eriksson, H. Bernhoff, M. Leijon, Evaluation of different turbine concepts for

wind power, *Renew. Sustain. Energy Rev.,* 12, (2008), 1419–1434.

[20]   P. Langemeier, C. Scheuer, Big challenges: the role of resin in wind turbine rotor blade development, *Reinforced Plastics*, Materials Today, (2010), 36–39.

[21]   S. Kumar, S. Krishnan, S. Mohanty, S. K. Nayak, Synthesis and characterization of petroleum and biobased epoxy resins: a review, *Polym. Int*., 67, (2018), 815–839.

[22]   R. Nijssen, G. D. de Winkel, Developments in materials for offshore wind turbine blades, in: C. Ng, L. Ran (Eds.), Offshore wind farms: technologies, design and operation, Woodhead Publishing, Duxford, UK 2016.

[23]   B. Ellis (Ed.), Chemistry and Technology of Epoxy Resins, Spinger, Netherlands, 1993.

[24]   J. E. Ehlers, N. G. Rondan, L. K. Huynh, H. Pham, M. Marks, T. N. Truong, Theoretical study on mechanisms of the epoxy-amine curing reaction, *Macromolecules,* 40, (2007), 4370–4377.

[25]   L. Matějka, J. Lövy, S. Pokorný, K. Bouchal, K. Dušek, Curing epoxy resins with anhydrides: model reactions and reaction mechanism, *J. Polym. Sci. Part A Polym. Chem*., 21, (1983), 2873–2885.

[26]   H. K. Weiss, Anhydride curing agents for epoxy resins, *Ind. Eng. Chem*., 49, (1957), 1089–1090.

[27]   R. Acosta Ortiz, O. Acosta Berlanga, A. E. García Valdez, R. Aguirre Flores, J. G. Télles Padilla, M. G. Méndez Padilla, Self-healing photocurable epoxy/thiol-ene systems using an aromatic epoxy resin, *Adv. Mater. Sci. Eng*., (2016), 1–11.

[28]   A. O. Konuray, X. Fernández-Francos, X. Ramis, Analysis of the reaction mechanism of the thiol-epoxy addition initiated by nucleophilic tertiary amines, *Polym. Chem*., 8, (2017), 5934–5947.

[29]   C. May, Epoxy Resins: Chemistry and Technology, 2nd Edition, CRC Press, New York, USA, 1987.

[30]   Evonik product report, Imidazole curing agents for epoxy resins, (2018), available: http://crosslinkers.evonik.com/product/crosslinkers/downloads/imidazole%20brochure.pdf (accessed May 18, 2020).

[31] J. B. Johnson, C. N. Owston, The effect of cure cycle on the mechanical properties of carbon fibre/epoxide resin, *Composites,*4, **3**, (1973) 111–117.

[32] J. Zhang, Y. C. Xu, P. Huang, Effect of cure cycle on curing process and hardness for epoxy resin, *eXPRESS Polym. Lett.*, 3, **9**, (2009) 534–541.

[33] A. Patel, O. Kravchenko, I. Manas-Zloczower, Effect of curing rate on the microstructure and macroscopic properties of epoxy fiberglass composites, *Polymers*, 10, **2**, (2018).

[34] H. Dodiuk, S.H. Goodman (Eds.), Handbook of thermoset plastics, third edition, Elsevier, 2014.

[35] J. P. Pascault, H. Sautereau, J. Verdu, R. J. J. Williams, Thermosetting polymers, Marcel Dekker, New York, USA, 2002.

[36] M. P. Pham, Theoretical studies of mechanisms of epoxy curing systems, *PhD Thesis*, The University of Utah, (2011).

[37] C. Li, K. Potter, M. R. Wisnom, G. Stringer, In-situ measurement of chemical shrinkage of MY750 epoxy resin by a novel gravimetric method, *Compos. Sci. Technol.*, 64, (2004), 55–64.

[38] P. S. Rhodes, Advances in anhydride epoxy systems, Proceedings in: *23rd Int. SAMPE Tech. Conf.*, New York, USA (1991).

[39] R. F. Fischer, Polyesters from epoxides and anhydrides, *Ind. Eng. Chem.*, 52, **4**, (1960), 321–323.

[40] Y. Tanaka, H. Kakiuchi, Study of epoxy compounds part I: curing reactions of epoxy resin and acid anhydride with amine and alcohol as catalyst, *J. Appl. Polym. Sci.*, 7, (1963), 1063–1081.

[41] M. K. Antoon, J. L. Koenig, Crosslinking mechanism of an anhydride-cured epoxy resin as studied by fourier transform infrared spectroscopy, *J. Polym. Sci. Polym. Chem. Ed.*, 19, (1981), 549–570.

[42] J. Rocks, Characterization of novel co-anhydride cured epoxy resins, *PhD Thesis*, Queensland University of Technology, (2004).

[43] European Environment Agency (EEA), EEA Technical Report, *Europe's onshore and offshore wind energy potential*, 6, (2009).

[44]   General Electric, Press release GE announces Haliade-X, the world's most
         powerful offshore wind turbine, 2018, available:
         https://www.ge.com/news/press-releases/ge-announces-haliade-x-worlds-most-
         powerful-offshore-wind-turbine (accessed October 19, 2019).

[45]   F. C. Campbell, Structural Composite Materials, ASM International, USA,
         2010.

[46]   Y. G. Thyavihalli Girijappa, S. Mavinkere Rangappa, J. Parameswaranpillai, S.
         Siengchin, Natural fibers as sustainable and renewable resource for
         development of eco-friendly composites: a comprehensive review, *Front.
         Mater.*, 6, (2019).

[47]   M. Vlasblom, The manufacture, properties and applications of high-strength,
         high-modulud polyethylene fibres, in: A. R Bunsell (Ed.), Handbook of Tensile
         Properties of Textile and Technical Fibres, 2nd edition, Woodhead Publishing,
         2009, 437-485.

[48]   Dyneema Fiber, Dyneema, DSM, available:
         https://www.dsm.com/products/dyneema/en_GB/technologies/dyneema-form-
         factors/fiber.html?WT.srch=1&WT.mc_id=SEA_dyneema-fiber_americas-
         emea-
         apac&gclid=Cj0KCQiA7aPyBRChARIsAJfWCgLLRg1Qn6MLtdxTp7NZ2vlz
         A00bPtyGfeHLtJ4mJ_0zBQ6a866TgFoaAv98EALw_wcB (accessed February
         16, 2020).

[49]   T. P. Sathishkumar, S. Satheeshkumar, J. Naveen, Glass fiber-reinforced
         polymer composites - a review, *J. Reinf. Plast. Compos.*, 33, **13**, (2014), 1258–
         1275.

[50]   The fiber, Compos. World. (2016).
         https://www.compositesworld.com/articles/the-fiber (accessed February 16,
         2020).

[51]   J. Thomason, P. Jenkins, L. Yang, Glass fibre strength - a review with relation
         to composite recycling, *Fibers*, 4, **18**, (2016).

[52]   F. M. Jensen, K. Branner, Chapter 1: Introduction to wind turbine blade design,
         in: P. Brøndsted, R. P. Nijssen (Eds.), Advances in wind turbine blade design
         and materials, Woodhead Publishing, 2013: pp. 3–25.

[53] National Research Council, Assessment of research needs for wind turbine blade rator materials technology, The National Academies Press, Washington, D.C, 1991.

[54] Composites World, Wind turbine blades: glass *vs*. carbon fiber, (2012). available: https://www.compositesworld.com/articles/wind-turbine-blades-glass-vs-carbon-fiber (accessed August 6, 2019).

[55] A. Wilson, Staying ahead in wind power: Vestas and Hexcel, *Inside Composites*, (2018), available: https://www.insidecomposites.com/staying-ahead-in-wind-power-vestas-and-hexcel/ (accessed July 22, 2019).

[56] L. Thomas, M. Ramachandra, Advanced materials for wind turbine blade- a review, *Materials Today: Proceedings*, 5, (2018), 2635–2640.

[57] Y. Swolfs, Perspective for fibre-hybrid composites in wind energy applications, *Materials*, 10, (2017).

[58] O. T. Thomsen, Sandwich materials for wind turbine blades - present and future, *J. Sandw. Struct. Mater.*, 11, (2009), 7–26.

[59] A. Petras, Design of sandwich structures, *PhD Thesis*, University of Cambridge, 1999.

[60] C. Kaboglu, S. Pimenta, A. Morris, J. P. Dear, The effect of different types of core material on the flexural behavior of sandwich composites for wind turbine blades, *J. Therm. Eng.*, 3, (2017), 1102–1109.

[61] D. Hull and T. Clyne, The interface region, in *An Introduction to Composite Materials*, Second edition, Cambridge University Press, Cambridge 1996, pp. 133–157.

[62] F. Severini, L. Formaro, M. Pegoraro, L. Posca, Chemical modification of carbon fiber surfaces, *Carbon*, 40, (2002), 735–741.

[63] L. Xiong, X. Qin, H. Liang, S. Huang, Z. Lian, Covalent functionalization of carbon fiber with poly(acrylamide) by reversible addition–fragmentation chain transfer polymerization for improving carbon fiber/epoxy interface, *Polym. Compos.*, (2017), 27–31.

[64] L. Servinis, K. M. Beggs, T. R. Gengenbach, E. H. Doeven, P. S. Francis, B. L.

Fox, J. M. Pringle, C. Pozo-Gonzalo, T. R. Walsh, L.C. Henderson, Tailoring the fibre-to-matrix interface using click chemistry on carbon fibre surfaces, *J. Mater. Chem. A*., 5, (2017), 11204–11213.

[65] S. Tiwari, J. Bijwe, Surface treatment of carbon fibers - a review, *Procedia Technol*., 14, (2014), 505–512.

[66] Y. Sawada, Y. Nakanishi, T. Fukuda, Effect of carbon fibre surface on interfacial adhesive strengths in CFRP, *Composites*, 24, (1993), 573–579.

[67] L. T. Drzal, N. Sugiura, D. Hook, The role of chemical bonding and surface topography in adhesion between carbon fibers and epoxy matrices, *Composite Interfaces,* 4, **5**, (1996), 337–354.

[68] O. Çoban, E. Akman, M.Ö. Bora, B. Genc Oztoprak, A. Demir, Laser surface treatment of CFRP composites for a better adhesive bonding owing to the mechanical interlocking mechanism, *Polym. Compos.*, 40, **9**, (2019).

[69] V. Cech, R. Prikryl, R. Balkova, A. Grycova, J. Vanek, Plasma surface treatment and modification of glass fibers, *Compos. Part A*., 33, (2002), 1367–1372.

[70] S. Mujin, H. Baorong, W. Yisheng, T. Ying, H. Weiqiu, D. Youxian, The surface of carbon fibres continuously treated by cold plasma, *Compos. Sci. Technol*., 34, (1989), 353–364.

[71] T. R. Pozegic, J. V. Anguita, I. Hamerton, K. D. G. I. Jayawardena, J-S. Chen, V. Stolojan, P. Ballocchi, R. Walsh, S. R. P. Silva, Multi-functional carbon fibre composites using carbon nanotubes as an alternative to polymer sizing, *Sci. Rep*., 6, (2016).

[72] R. J. Sager, P. J. Klein, D. C. Lagoudas, Q. Zhang, J. Liu, L. Dai, J. W. Baur, Effect of carbon nanotubes on the interfacial shear strength of T650 carbon fiber in an epoxy matrix, *Compos. Sci. Technol*., 69, (2009), 898–904.

[73] G. Marsh, What are the tools of the wind turbine blade trade?, *Renewable Energy Focus,* (2008), available http://www.renewableenergyfocus.com/view/3292/what-are-the-tools-of-the-wind-turbine-blade-trade/ (accessed February 16, 2020).

[74] G. Petsche, T. Kellner, Blade runners: a look inside a factory for giant wind

turbine blades, GE Reports, (2018), available: https://www.ge.com/reports/towering-achievement-look-inside-factory-giant-wind-turbine-blades/ (accessed February 16, 2020).

[75] K. K. Verma, B. L. Dinesh, K. Singh, K. M. Gaddikeri, V. Srinivasa, R. Kumar, R. Sundaram, Development of vacuum enhanced resin infusion technology (VERITy) process for manufacturing of primary aircraft structures, *Journal of the Indian Insitute of Science*, 93, **4**, (2013), 621–633.

[76] S. C. Nolet, Composite wind blade engineering and manufacturing, Massachusetts Insitute of Technology Independent Activities Periods Mini Course (2011), available: http://web.mit.edu/windenergy/windweek/Presentations/Nolet_Blades.pdf (accessed May 18, 2020).

[77] G. Marsh, Tooling up for large wind turbine blades, *Renewable Energy Focus*, (2007), available: http://www.renewableenergyfocus.com/view/1149/tooling-up-for-large-wind-turbine-blades/ (accessed February 16, 2020).

[78] G. Marsh, Industry perspective preview: what to do with "spent" wind turbine blades?, *Renewable Energy Focus*, (2017), available: http://www.renewableenergyfocus.com/view/46397/industry-perspective-preview-what-to-do-with-spent-wind-turbine-blades/ (accessed February 16, 2020).

[79] J. A. Grande, Wind power blades energise composites manufacturing, *Plastics Technology*, (2008), available: https://www.ptonline.com/articles/wind-power-blades-energize-composites-manufacturing (accessed July 23, 2019).

[80] G. C. Jacob, B. Hoevel, H. Q. Pham, M. L. Dettloff, N. E. Verghese, R. H. Turakhia, G. Hunter, J. F. Mandell, D. D. Samborsky, Technical advances in epoxy technology for wind turbine blade composite fabrication, International SAMPE Technical Conference, 2009.

[81] Hitachi Chemical Company Ltd, Internal presentaton: Introduction of wind power related products, 2011.

[82] P. Wang, S. Drapier, J. Molimard, A. Vautrin, J. C. Minni, Numerical and experimental analyses of resin infusion manufacturing processes of composite

materials, *J. Compos. Mater.*, 46, (2012), 1617–1631.

[83]   P. Brøndsted, R. P. L. Nijssen, Chapter 6: Fatigue as a design driver for composite wind turbine blades, in: Advances in Wind Turbine Blade Design and Materials, Woodhead Publishing Limited, 2013: pp. 175–209.

[84]   J. Dominy, C. Rudd, Manufacturing with thermosets, in: A. Long (Ed.), Design and Manufacture of Textile Composites, CRC Press, 2006.

[85]   S. van Oosterom, T. Allen, M. Battley, S. Bickerton, An objective comparison of common vacuum assisted resin infusion processes, *Compos. Part A.*, 125, (2019).

[86]   C. J. Hughes, J. W. Gillespie Jr, D. Heider, S. Amouroux, VARTM Variability and Substantiation, 2008, available: https://pdfs.semanticscholar.org/a3aa/b29cf4a49f3a5ea4919710235c7ee837a6dd.pdf?_ga=2.52613921.867511107.1581853717-1206832688.1581853717 (accessed May 18, 2020).

[87]   P. S. Veers, T. D. Ashwill, H. J. Sutherland, D. Laird, Trends in the design, manufacture and evaluation of wind turbine blades, *Wind Energy*, 6, **3**, (2003), 245–259.

[88]   M. Legault, Wind blades: progess and challenges, *CompositesWorld,* (2013). available: https://www.compositesworld.com/articles/wind-blades-progress-and-challenges (accessed February 16, 2020).

[89]   Y. N. Liu, C. Yuan, C. Liu, J. Pan, Q. Dong, Study on the resin infusion process based on automated fiber placement fabricated dry fiber preform, *Sci. Rep.*, 9, (2019), 1–11.

[90]   S. Zhu, C. J. Magnussen, E. L. Judd, M. C. Frank, F. E. Peters, Automated composite fabric layup for wind turbine blades, *J. Manuf. Sci. Eng.*, 139, (2017).

[91]   Z. Lanting, Research on structural lay-up optimum design of composite wind turbine blade, *Energy Procedia.*, 14, (2012), 637–642.

[92]   Y. K. Kim, S. R. White, Viscoelastic analysis of processing-induced residual stresses in thick composite laminates, *Mech. Compos. Mater. Struct.*, 4, (1997), 361–387.

[93]   E. Greenhalgh (Ed.), Defects and damage and their role in the failure of polymer

composites, in: Failure Analysis and Fractography of Polymer Composites, Woodhead Publishing Limited, 2009.

[94] D. S. Cairns, T. Riddle, J. Nelson, Wind turbine composite blade manufacturing: the need for understanding defect origins, prevalence, implications and reliability, Sandia National Laboratories Report, 2011.

[95] T. A. Bogetti, J. W. Gillespie, Process-induced stress and deformation in thick-section thermoset composite laminates, *J. Compos. Mater.*, 26, (1992), 626–660.

[96] J. H. Oh, D. G. Lee, Cure cycle for thick glass / epoxy composite laminates, *J. Compos. Mater.*, 36, (2002), 19–45.

[97] S. R. White, H. T. Hahn, Cure cycle optimization for the reduction of processing-induced residual stresses in composite materials, *J. Compos. Mater.*, 27, (1993), 1352–1378.

[98] T. A. Bogetti, J. W. Gillespie, Two-dimensional cure simulation of thick thermosetting composites, *J. Compos. Mater.*, 25, (1991), 239–273.

[99] J. N. Hay, P. O'Gara, Recent developments in thermoset curing methods, *Proceedings of the Insitution of Mechanical Engineers, Part G: Journal of Aerospace Engineering*, 220, **3**, (2006), 187–195.

[100] Y. Jiang, A novel method for the manufacturing of thick composites, *PhD* Thesis, Concordia Univeristy, Canada, 2004.

[101] G. Marsh, Mould tool heating - the oven-free alternative, *Reinforced Plastics*, 47, (2003), 38–41.

[102] R. Abdalrahman, S. Grove, A. Kyte, M. J. Rizvi, Numerical studies of integrally-heated composite tooling, Proceedings in: ECCM16, 16th European Conference on Composite Materials, Seville, Spain, 2014.

[103] J. Schlimbach, A. Ogale, Quickstep : beyond out of autoclave curing, Proceedings in: International SAMPE Technical Conference, Long beach, USA, 2011.

[104] S. R. White, Y. K. Kim, Staged curing of composite materials, *Compos. Part A.*, 27, (1996), 219–227.

[105] A. Skordos, J. Kratz, Layer by layer curing (LbL) feasibility study final report, CIMComp, 2018.

[106] C. Dispenza, S. Alessi, G. Spadaro, Carbon fiber composites cured by γ-radiation-induced polymerization of an epoxy resin matrix, *Adv. Polym. Technol.*, 27, (2008), 163–171.

[107] M. Invernizzi, G. Natale, M. Levi, S. Turri, G. Griffini, UV-assisted 3D printing of glass and carbon fiber-reinforced dual-cure polymer composites, *Materials*, 9, (2016).

[108] T. Glauser, M. Johansson, and A. Hult, A comparison of radiation and thermal curing of thick composites, *Macromol. Mater. Eng.*, 274, (2000), 25-30.

[109] A. Endruweit, M. S. Johnson, A. C. Long, Curing of composite components by ultraviolet radiation: a review, *Polym. Compos.*, (2006), 119–128.

[110] J. Zhou, Y. Li, L. Cheng, L. Zhang, Indirect microwave curing process design for manufacturing thick multidirectional carbon fiber reinforced thermoset composite materials, *Appl. Compos. Mater.*, 26, (2019), 533–552.

[111] R. Yusoff, M. K. Aroua, A. Nesbitt, R. J. Day, Curing of polymeric composites using microwave resin transfer moulding (RTM), *J. Eng. Sci. Technol.*, 2, (2007), 151–163.

[112] A. J. Berejka, C. Eberle, Electron beam curing of composites in North America, *Radiat. Phys. Chem.*, 63, (2002), 551–556.

[113] D. A. Nishitsuji, G. Marinucci, M. C. Evora, and L. G. de Andrade e Silva, Study of electron beam curing process using epoxy resin system, *Nuclear Instruments and Methods in Physics Research B,* 265, (2007), 135–138.

[114] F. Guasti, E. Rosi, Low energy electron beam curing for thick composite production, *Compos. Part A.*, 28A, (1997), 965–969.

[115] D. Abliz, Y. Duan, L. Steuernagel, L. Xie, D. Li, G. Ziegmann, Curing methods for advanced polymer composites - a review, *Polymers and Polymer Composites*, 21, (2013), 341–348.

[116] J. H. Lee, R. K. Prud'homme, I. A. Aksay, Cure depth in photopolymerization: experiments and theory, *J. Mater. Res.*, 16, (2001), 3536–3544.

[117] E. T. Thostenson, T. Chou, Microwave and conventional curing of thick-section

thermoset composite laminates: experiment and simulation, *Polymer Composites*, 22, **2**, (2001).

[118] J. Sloan, Microwave: an alternative to the autoclave?, *CompositesWorld,* (2011), available: https://www.compositesworld.com/articles/microwave-an-alternative-to-the-autoclave (accessed February 15, 2020).

[119] X. Xu, Y. Zhang, J. Jiang, H. Wang, X. Zhao, Q. Li, W. Lu, In-situ curing of glass fiber reinforced polymer composites via resistive heating of carbon nanotube films, *Compos. Sci. Technol.*, 149, (2017), 20–27.

[120] Huikeshoven product information, Powersheat carbon heating, Huikeshoven Ind., (2015). available: http://huikeshoven.nl/en/producten/powersheat-carbonheating/ (accessed August 23, 2019).

[121] Lantor launches new nonwoven heating concept at the JEC 2014, NetComposites. (2014), available: https://netcomposites.com/news/lantor-launches-new-nonwoven-heating-concept-at-the-jec-2014/ (accessed August 23, 2019).

[122] H. Fukuda, Processing of carbon fiber reinforced plastics by means of Joule heating, *Adv. Compos. Mater.*, 3, (1994), 153–161.

[123] N. Athanasopoulos, G. Sotiriadis, V. Kostopoulos, A study on the effect of Joule-heating during the liquid composite molding (LCM) process and on the curing of CFRP composite laminates, Proceedings in: The 10th International Conference on Flow Processes in Composite Materials (FPCM10), Switzerland, 2010.

[124] S. A. Hayes, A. D. Lafferty, G. Altinkurt, P. R. Wilson, M. Collinson, P. Duchene, Direct electrical cure of carbon fiber composites, *Adv. Manuf. Polym. Compos. Sci.*, 1, (2015), 112–119.

[125] M. Harada, M. Ochi, M. Tobita, T. Kimura, T. Ishigaki, N. Shimoyama, H. Aoki, Thermal-conductivity properties of liquid-crystalline epoxy resin cured under a magnetic field, *J. Polym. Sci. Part B Polym. Phys.*, 41, (2003), 1739–1743.

[126] T. Bayerl, M. Duhovic, P. Mitschang, D. Bhattacharyya, The heating of polymer composites by electromagnetic induction - a review, *Compos. Part A.*,

57, (2014), 27–40.

[127] G. Ariu, I. Hamerton, D. Ivanov, Positioning and aligning CNTs by external magnetic field to assist localised epoxy cure, *Open Phys.*, 14, (2016), 508–516.

[128] E. F. Reia Da Costa, A. A. Skordos, I. K. Partridge, A. Rezai, RTM processing and electrical performance of carbon nanotube modified epoxy/fibre composites, *Compos. Part A.*, 4, **3**, (2012), 593–602.

[129] J. R. N. Gnidakouong, H. D. Roh, J. H. Kim, Y. Bin Park, In-situ assessment of carbon nanotube flow and filtration monitoring through glass fabric using electrical resistance measurement, *Compos. Part A.*, 90, (2016), 137–146.

[130] A. K. K. Matt, S. Beyhaghi, R. S. Amano, J. Guo, Self-healing of wind turbine blades using microscale vascular vessels, *J. Energy Resour. Technol.*, 139, (2017).

[131] R. Shen, R. S. Amano, G. Lewinski, A. K. K. Matt, A new vascular system highly efficient in the storage and transport of healing agent for self-healing wind turbine blades, *J. Energy Resour. Technol.*, 141, (2019).

[132] R. Shen, R. S. Amano, G. Lewinski, Self-healing performance comparison between two promising vascular vessel systems of the wind turbine blade, *J. Energy Resour. Technol.*, 141, (2019).

[133] A.K. K. Matt, S. Strong, T. El-Gammal, R. S. Amano, Development of novel self-healing polymer composites for use in wind turbine blades, *J. Energy Resour. Technol.*, 137, (2015).

[134] K. Boba, C. Heath, M. McElroy, A. Lawrie, R. Trask, I. Bond, Development of embedded vascular networks in FRP for active / passive thermal management, University of Bristol Internal Report, 2015.

[135] O. Parent, A. Ilinca, Anti-icing and de-icing techniques for wind turbines: critical review, *Cold Reg. Sci. Technol.*, 65, (2011), 88–96.

[136] F. De Rosa, Electrically heated composite leading edges for aircraft anti-icing applications, *PhD Thesis*, University of Naples, 2010.

[137] M. P. O'Donnell, Y. Mahadik, C. Ward, Cure rate tailoring of thick composites *via* temperature controlled vascular pathways, Proceedings in: 57th AIAA/ASCE/AHS/ASC Structures, Structural Dynamics and Materials

Conference, San Diego, California, 2016.

[138]   S. Solarski, LTx1240 fabric specification, Owen Cornings, Belgium, Personal communication, April, 6 2017.

[139]   Owens Corning, XStrandH-Product information, (2012), available: http://www.informaworld.com/openurl?genre=article&doi=10.1080/096132191 08727117&magic=crossref%7C%7CD404A21C5BB053405B1A640AFFD44A E3%5Cnfile:///C:/Users/Owner/Documents/bibliography/Information - 1991.pdf (accessed October, 19 2019).

[140]   Owens Corning, Advantex glass fibre reinforcements, a total solution for the composites industry, (2003), available: https://www.pressreleasefinder.com/prdocs/2003/Advantex_Glass_fiber_Reinfo rcements.pdf (accessed October 19, 2019).

[141]   A. Broad, Development of vacuum assisted composites manufacturing technology for wind turbine blade manufacture, *MSc Thesis*, University of Central Lancashire, 2013.

[142]   EasyComposites, Guide to resin infusion, 2010, available: https://www.easycomposites.co.uk/downloads/TDS/EC-TDS-Guide-to-Resin-Infusion.pdf (accessed May 18, 2020).

[143]   F. C. Campbell, Manufacturing processes for advanced composites, Elsevier, Oxford, UK, 2003.

[144]   Humboldt Univerity of Berlin, Institute of Physics-advanced lab, Investigation of polymers with differential scanning calorimetry, available: http://polymerscience.physik.hu-berlin.de/docs/manuals/DSC.pdf (accessed May 18, 2020).

[145]   J. Xie, Y. Li, W. Wang, S. Pan, N. Cui, J. Liu, Comments on thermal physical properties testing methods of phase change materials, *Adv. Mech. Eng.*, (2013).

[146]   TA Instruments report, Modulated DSC (MDSC): How Does It Work?, available: http://www.tainstruments.com/pdf/literature/MDSC.pdf (accessed May 18, 2020).

[147]   L. C. Thomas, Why modulated DSC?: An overview and summary of advantages

and disadvantages relative to traditional DSC, TA Instruments (2005).

[148] Hitachi high-tech science corporation, Application brief: Specific heat capacity measurements using DSC 1., Chuo-ku, Tokyo, 1981.

[149] G. Kaiser, Netzsch, Specific heat: theoretical background and practical hints for measurements, (2009).

[150] Netzsch, Starting a measurement and data evaluation of a C_p measurement, Software manual, (2009).

[151] I. McAninch, G. R. Palmese, J. L. Lenhart, J. La Scala, DMA testing of epoxy resins: the importance of dimensions, *Polym. Eng. Sci.*, (2015), 2761–2772.

[152] K. P. Menard, N. R. Menard, Dynamic mechanical analysis in the analysis of polymers and rubbers, In: Encyclopaedia of Polymer Science and Technology, (2015).

[153] TA-Instruments, ARES-G2 Rheometer, ARES-G2 Instrument Manual. (2014) 1–33. available: http://www.tainstruments.com/ares-g2-quickstart-guide/ (accessed May 18, 2020).

[154] A.Y. Malkin, A.I. Isayev, Rheology: Concepts, Methods and Applications, 2nd Edition, ChemTec Publishing, Canada, 2017.

[155] J. Gotro, Rheology of thermosets part 3: controlled strain measurements, Polymer Innovation Blog, (2014), available: https://polymerinnovationblog.com/rheology-thermosets-part-3-controlled-strain-measurements/ (accessed September 12, 2019).

[156] C. H. Han, Rheology and processing of polymeric materials: Volume I Polymer Rheology, Oxford University Press, New York, USA, 2007.

[157] M. Kontopoulou (Ed.), Applied Polymer Rheology: polymeric fluids with industrial applications, John Wiley & Sons, Inc, New Jersey, 2011.

[158] P. J. Haines, (Ed.), Principles of thermal analysis and calorimetry, Royal Society of Chemistry, Cambridge, UK, 2002.

[159] M. A. A. Mohsin, L. Iannucci, E. S. Greenhalgh, Fibre-volume-fraction measurement of carbon fibre reinforced thermoplastic composites using thermogravimetric analysis, *Heliyon,* 5, (2019).

161

[160] D. Zhao, X. Qian, X. Gu, S.A. Jajja, R. Yang, Measurement techniques for thermal conductivity and interfacial thermal conductance of bulk and thin film materials, *J. Electron. Packag*., 138, (2016).

[161] W. J. Parker, R. J. Jenkins, C. P. Butler, G. L. Abbott, Flash method of determining thermal diffusivity, heat capacity, and thermal conductivity, *J. Appl. Phys*., 32, (1961).

[162] ASTM E1461-13 Standard test method for thermal diffusivity by the flash method, ASTM International, West Conshohocken, USA, 2012.

[163] ASTM D2344/D2344M-16, Standard test method for short-beam strength of polymer matrix composite materials and their laminates, West Conshohocken, USA, 2016.

[164] C. Medina, J. Molina-Aldareguia, C. Gonzalez, M. F. Melendrez, P. Flores, J. L. Llorca, Comparison of push-in and push-out tests for measuring interfacial shear strength in nano-reinforced composite materials, *J. Compos. Mater*., 50, **12**, (2015).

[165] X. F. Zhou, H. D. Wagner, S. R. Nutt, Interfacial properties of polymer composites measured by push-out and fragmentation tests, *Compos. Part A*., (2001), 1543–1551.

[166] D. Tripathi, F. R. Jones, Single fibre fragmentation tests for assessing adhesion in fibre reinforced composites, *J. Mater. Sci*., 33, (1998), 1–16.

[167] J. P. Favre, M.C. Merienne, Characterization of fibre/resin bonding in composites using a pull-out test, *Int. J. Adhes. Adhes*., 1, (1981), 311–316.

[168] B. Miller, P. Muri, L. Rebenfeld, A microbond method for determination of the shear strength of a fiber/ resin interface, *Compos. Sci. Technol*., 28, (1987), 17–32.

[169] V. Rao, P. Herrera-franco, A. D. Ozzello, L. T. Drzal, A direct comparison of the fragmentation test and the microbond pull-out test for determining the interfacial shear strength, *J. Adhes*., 34, (1991), 65–77.

[170] S. Sockalingam, G. Nilakantan, Fiber-matrix interface characterization through the microbond test: a review, *Int. J. Aeronaut. Sp. Sci*., 13, (2012), 282–295.

[171] A. Wada, H. Fukuda, Microbond test for the fiber/matrix interfacial shearing strength, Proceedings in: 12th International Conference on Composite Materials (ICCM12), Paris, France, 1999.

[172] P. J. Herrera-Franco, L. T. Drzal, Comparison of methods for the measurement of fibre/matrix adhesion in composites, *Composites,* 23, (1992), 2–27.

[173] S. Feih, K. Wonsyld, D. Minzari, P. Westermann, H. Lilholt, Testing procedure for the single fiber fragmentation test, Riso National Laboratory Report, Roskilde, Denmark, 2004.

[174] S. A. Azamtu, Assessing the interfacial shear strength of anhydride-cured epoxy resins on glass fibre, by means of single-fibre microbond testing, *MEng Dissertation*, University of Bristol, 2019.

[175] J. A. Nairn, C-H. Liu, Analytical and experimental methods for a fracture mechanics interpretation of the microbond test including the effects of friction and thermal stresses, *Int. J. Adhes. Adhes.*, 19, (1999), 59–70.

[176] R. J. Day, J. V. Cauich Rodrigez, Investigation of the micromechanics of the microbond test, *Compos. Sci. Technol.*, 58, (1998), 907–914.

[177] D. J. Bannister, M. C. Andrews, A. J. Cervenka, R .J. Young, Analysis of the single-fibre pull-out test by means of Raman spectroscopy: Part II. Micromechanics of deformation for an aramid/epoxy system, *Compos. Sci. Technol.*, 53, (1995), 411–421.

[178] M. J. Pitkethly, J. P. Favre, U. Gaur, J. Jakubowski, S. F. Mudrich, D. L. Caldwell, L. T. Drzal, M. Nardin, H. D. Wagner, L. Di Landro, A. Hampe, J. P. Armistead, M. Desaeger, I. Verpoest, A round-robin programme on interfacial test methods, *Compos. Sci. Technol.*, 48, (1993), 205–214.

[179] C. Zhi, H. Long, M. Miao, Influence of microbond test parameters on interfacial shear strength of fiber reinforced polymer-matrix composites, *Compos. Part A.*, 100, (2017), 55–63.

[180] M. Nishikawa, T. Okabe, K. Hemmi, and N. Takeda, Micromechanical modeling of the microbond test to quantify the interfacial properties of fiber-reinforced composites, *Int. J. Solids Struct.*, 45, (2008), 4098–4113.

[181] C. T. Chou, U. Gaur, B. Miller, The effect of microvise gap width on microbond

pull-out test results, *Compos. Sci. Technol.*, 51, (1994), 111–116.

[182] H. F. Wu and C. M. Claypool, An analytical approach of the microbond test method used in characterizing the fibre-matrix interface, *J. Mater. Sci. Lett.*, 10, (1991), 260–262.

[183] H. Wang, H. Wang, W. Li, D. Ren, Y. Yu, An improved microbond test method for determination of the interfacial shear strength between carbon fibers and epoxy resin, *Polym. Test.*, 32, (2013), 1460–1465.

[184] A. Le Duigou, P. Davies, C. Baley, Interfacial bonding of Flax fibre/Poly(l-lactide) bio-composites, *Compos. Sci. Technol.*, 70, (2010), 231–239.

[185] J .P. Craven, R. Cripps, C. Viney, Evaluating the silk/epoxy interface by means of the microbond test, *Compos. Part A.*, 31, (2000), 653–660.

[186] C. Baley, Y. Grohens, F. Busnel, P. Davies, Application of interlaminar tests to marine composites. Relation between glass fibre/polymer interfaces and interlaminar properties of marine composites, *Appl. Compos. Mater.*, 11, (2004), 77–98.

[187] D. A. Biro, P. Mclean, Y. Deslandes, Application of the microbond techniques: characterization of carbon fiber- epoxy interfaces, *Polym. Eng. Sci.,* 31, **17**, (1991), 1250-1256.

[188] B. K. Russell, S. Takeda, C. Ward, I. Hamerton, Examining the influence of carboxylic anhydride structures on the reaction kinetics and processing characteristics of an epoxy resin for wind turbine applications, *React. Funct. Polym.*, 144, (2019).

[189] ASTM D570-98(2018), Standard test method for water absorption of plastics, ASTM International, West Conshohocken, USA, 2018.

[190] ASTM E228-11, Standard test method for linear thermal expansion of solid materials with a push-rod dilatometer, ASTM International, West Conshohocken, USA, 2011.

[191] N. Patel, S. Mortimer, S. Stevens, Hexcel Composites Ltd., *Improvements in or relating to infusion moulding*, GB2554147, 2016.

[192] K.W. Lienert, M. Busi, N. Colombi, A. Paderzani, P. Gherardi, Elantas GmbH,

Epoxy resin curing indicator composition, US 2012/0225187 A1, 2010.

[193] H. Ishida and D. J. Allen, Mechanical characterization of copolymers based on benzoxazine and epoxy, *Polymer*, 37, **20**, (1996), 4487–4495.

[194] I. Hamerton, L. T. Mcnamara, B. J. Howlin, P. A. Smith, P. Cross, S. Ward, Examining the initiation of the polymerization mechanism and network development in aromatic polybenzoxazines, *Macromolecules,* 46, (2013), 5117–5132.

[195] C. Conreur, J. Francillette, and F. Lauprete, Synthesis and processing of model compound of PMR-15 resin, *J. Polym. Sci. Part A Polym. Chem.*, 35, **1**, (2000).

[196] D. Birney, T. K. Lim, H. P. Koh, B. R. Pool, J. M. White, Structural investigations into the retro-Diels-Alder reaction: experimental and theoretical studies, *J. Am. Chem.Soc.*, 124, (2002), 5091–5099

[197] Z. Cai, B. Shen, W. Liu, Z. Xin, H. Ling, Liquid-phase cracking of dicyclopentadiene by reactive distillation, *Energy Fuels,* 23, (2009), 4077–4081.

[198] C. S. Chen, B. J. Bulkin, E. M. Pearce, The preparation, characterization, and curing of epoxy resins and their copolymers, *J. Appl. Polym. Sci.*, 27, (1982), 3289–3312.

[199] M. G. González, J. C. Cabanelas, J. Baselga, Applications of FTIR on epoxy resins – identification, monitoring the curing process, phase separation and water uptake, *Infrared Spectrosc. Sci. Eng. Technol.*, 2, (2012).

[200] S. Masoumi, H. Valipour, Effects of moisture exposure on the crosslinked epoxy system: an atomistic study, *Model. Simul. Mater. Sci. Eng.*, 24, (2016).

[201] L. El-Sa'ad, M. I. Darby, B. Yates, Moisture absorption by epoxy resins: The reverse thermal effect, *J. Mater. Sci.*, 25, (1990), 3577–3582.

[202] M. H. Shirangi, X. J. Fan, B. Michel, Mechanism of moisture diffusion, hygroscopic swelling and adhesion degradation in epoxy molding compounds, Proceedings in: 41st International Symposium on Microelectronics, Rhode Island, USA, 2008.

[203] W. W. Wright, The effect of diffusion of water into epoxy resins and their carbo-fibre reinforced composites, *Composites,* (1981), 201–205.

[204] J. M. Barton, D. C. L. Greenfield, Use of dynamic mechanical methods to study

the effect of absorbed water on temperature-dependent properties of an epoxy resin-carbon fibre composite., *Br. Polym. J.*, 18, (1986), 51–56.

[205] K. J. Wong, Moisture absorption characteristics and effects on mechanical behaviour of carbon/epoxy composite : application to bonded patch repairs of composite structures, *PhD Thesis,* Université de Bourgogne, 2013.

[206] J. M. Ryan, R. Adams, S. G. R. Brown, Moisture ingress effect on properties of CFRP, Proceedings in: 17th International Conference on Composite Materials (ICCM), Edinburgh, UK, 2009.

[207] S .G. Taghavi, Moisture effects on high performance polymer composites, *PhD Thesis,* University of Toronto, 2000.

[208] C. L. Soles, A. F. Yee, Discussion of the molecular mechanisms of moisture transport in epoxy resins, *J. Polym. Sci. Part B Polym. Phys*., 38, (2000), 792–802.

[209] M. A. S. Shohag, E. C. Hammel, D. O. Olawale, O. I. Okoli, Damage mitigation techniques in wind turbine blades: a review, *Wind Eng*., 41, (2017), 185–210.

[210] J. Clark, The reaction of acid anhydrides with water, acholos and phenol, ChemGuide. (2004). available: https://www.chemguide.co.uk/organicprops/anhydrides/oxygen.html (accessed May 11, 2020).

[211] I. Hamerton, W. Tang, J. V. Anguita, S. R. P. Silva, Dramatic reductions in water uptake observed in novel POSS nanocomposites based on anhydride-cured epoxy matrix resins, *Mater. Today Commun*., 4, (2015), 186–198.

[212] T. Glaskova, A. Aniskevich, Moisture absorption by epoxy/montmorillonite nanocomposite, *Compos. Sci. Technol*., 69, (2009), 2711–2715.

[213] M. Shettar, U. A. Kini, S. Sharma, P. Hiremath, M. C. Gowrishankar, Study on the mechanical properties of nanoclay-epoxy composites under different hygrothermal aging conditions, *Mater. Res. Express*., 6, (2019).

[214] F. Liang, J. Gou, J. Kapat, H. Gu, G. Song, Multifunctional nanocomposite coating for wind turbine blades, *Int. J. Smart Nano Mater*., 2, (2011), 120–133.

[215] G. A. Pogany, The β-relaxation in epoxy resins; the temperature and time-

dependence of cure, *J. Mater. Sci.*, 4, (1969), 405–409.

[216] J. A. Dudek, J. A. Kargol, Linear thermal expansion coefficients for an epoxy/ glass matte-insulated solid cast transformer, *Int. J. Thermophys.*, 9, (1988), 245– 253.

[217] R. Hardis, Cure kinetics characterization and monitoring of an epoxy resin for thick composite structures, *Graduate Thesis and Dissertations,* Iowa State University, USA, 2012.

[218] J. Ding, W. Peng, T. Luo, H. Yu, Study on the curing reaction kinetics of a novel epoxy system, *RSC Adv.*, 7, (2017), 6981–6987.

[219] M. K. Um, I. M. Daniel, B .S. Hwang, A study of cure kinetics by the use of dynamic differential scanning calorimetry, *Compos. Sci. Technol.*, 62, (2002), 29–40.

[220] B. K. Russell, S. Takeda, C. Ward, I. Hamerton, The processing of a novel polymer matrix for wind turbine blades, Proceeding in: Thermosetting Resins, Berlin, Germany, 2018.

[221] S. M. Taylor and P. J. Fryer, A numerical study of the use of the kissinger analysis of DSC thermograms to obtain reaction kinetic parameters, *Thermochimica Acta*, 209, (1992), 111–125.

[222] T. Ozawa, Kinetic analysis of derivative curves in thermal analysis, *J. Therm. Anal.*, 2, (1970), 301–324.

[223] J. Barton, The application of differential scanning calorimetry (DSC) to the study of epoxy resin curing reactions, in: Epoxy Resins Composites I. Advances in Polymer Science, Springer, Berlin, Heidelberg, (1985), 111–154.

[224] M. A. Acitelli, R. B. Prime, E. Sacher, Kinetics of epoxy cure: (1) The system bisphenol-A diglycidyl ether/m-phenylene diamine, *Polymer*, 12, (1971), 335– 343.

[225] M. E. Ryan, A. Dutta, Kinetics of epoxy cure: a rapid technique for kinetic parameter estimation, *Polymer*, 20, (1979), 203–206.

[226] P. I. Karkanas, I. K. Partridge, Cure modeling and monitoring of epoxy/amine resin systems. I. Cure kinetics modeling, *J. Appl. Polym. Sci.*, 77, (2000), 1419– 1431.

[227] T. Mesogitis, A. Skordos, I. Hamerton, I. Partridge, J. Kratz, Developing cure kinetics models for interleaf particle toughened epoxies, Proceedings in: SAMPE International Conference, Long Beach, USA, 2016.

[228] S. Corezzi, D. Fioretto, G. Santucci, J. M. Kenny, Modeling diffusion-control in the cure kinetics of epoxy-amine thermoset resins: an approach based on configurational entropy, *Polymer*, 51, (2010), 5833–5845.

[229] N. Rabearison, C. Jochum, J. C. Grandidier, A cure kinetics, diffusion controlled and temperature dependent, identification of the Araldite LY556 epoxy, *J. Mater. Sci.*, 46, (2011), 787–796.

[230] ASTM D2584-18, Standard test method for ignition loss of cured reinforced resins, ASTM International, West Conshohocken, USA, 2018.

[231] Dynamax Corporation, Product datasheet: Ultra light-weld 3191 Structural plastic bonder with blue flourescence, 2012.

[232] F. Zhao, N. Takeda, K. Inagaki, N. Ikuta, A study on interfacial shear stength of GF/epoxy composites by means of microbond tests, *Adv. Compos. Lett.*, 5, (1996), 113–116.

[233] H. Wang, H. Wang, W. Li, D. Ren, Y. Yu, An improved microbond test method for determination of the interfacial shear strength between carbon fibers and epoxy resin, *Polym. Test.*, 32, (2013), 1460–1465.

[234] Prime ^{TM} 20LV- epoxy infusion system, Gurit, 2015, available: https://www.gurit.com/sitecore/content/Old-Product-Pages/Other-Products/Laminating-Infusion-Systems/PRIME-20LV (accesses May 18, 2020).

[235] Hexion, Technical data sheet: Epikure Curing agent RIMH037 and Epikote resin MGS RIMR 035, 2015, Personal communitcation, February 22, 2018.

[236] E. Dallies, Owens Corning, Strengthening the pultrusion market with high-performance glass reinforcement, Proceedings in: JEC Composites Show, Paris, France, 2011, available: http://www.owenscorningindia.com/OCIndia/Composites/Reinforcement/PDF/X_StrandH_presentatin_Final_03_23_11.pdf (accessed May 18, 2020).

[237] F. G. Garcia, B. G. Soares, V. J. R. R. Pita, R. Sánchez, J. Rieumont,

Mechanical properties of epoxy networks based on DGEBA and aliphatic amines, *J. Appl. Polym. Sci.*, 106, (2007), 2047–2055.

[238] M. Gottlieb, H. Dvir, Effect of silane sizing on polymer-glass adhesion, Proceedings in: ICCM 16th International Conference on Composite Materials (ICCM16), Kyoto, Japan, 2007.

[239] S. K. Kang, D. B. Lee, N. S. Choi, Fiber/epoxy interfacial shear strength measured by the microdroplet test, *Compos. Sci. Technol.*, 69, (2009), 245–251.

[240] T. G. Myers, N. D. Fowkes, Y. Ballim, Modeling the cooling of concrete by piped water, *J. Eng. Mech.*, 135, (2009), 1375–1383.

[241] M. P. O'Donnell, B. K. Russell, H. Jones, Y. Mahadik, S. Takeda, I. Hamerton, C. Ward, Cure management of thick composites using vascular networks. Submitted and under review, 2020.

[242] G. Ariu, The feasibility of embedded vascular networks in FRP as active/passive thermal management tools for cure processing, University of Bristol Internal Report, 2014.

[243] Saint-Gobain Vetrotex, Technical data sheet: E, R and D glass properties, Herzogenrath, Germany, 2002, available: https://glassproperties.com/glasses/E_R_and_D_glass_properties.pdf (accessed October 19, 2019).

[244] D. P. H. Hasselman, H. Bhatt, K. Y. Donaldson, J. R. Thomas Jr, Effect of fiber orientation and sample geometry on the effective thermal conductivity of a uniaxial carbon fiber-reinforced glass matrix composite, *J. Compos. Mater.*, 26, (1992), 2278–2288.

[245] C. J. Norris, I. P. Bond, R. S. Trask, The role of embedded bioinspired vasculature on damage formation in self-healing carbon fibre reinforced composites, *Compos. Part A,.* 42, (2011), 639–648.

[246] L. Khoun, P. Hubert, Cure shrinkage characterization of an epoxy resin system by two in-situ measurement methods, *Polym. Compos.*, (2010), 1603–1610.

[247] G. Struzziero, B. Remy, A. A. Skordos, Measurement of thermal conductivity of epoxy resins during cure, *J. Appl. Polym. Sci.*, 136, (2019).

[248] B. C. Chern, T. J. Moon, J. R. Howell, Measurement of the temperature and

cure dependence of the thermal conductivity of epoxy resin, *Exp. Heat Transf.*, 6, (1993), 157–174.

[249] J. McHugh, P. Fideu, A. Herrmann, W. Stark, Determination and review of specific heat capacity measurements during isothermal cure of an epoxy using TM-DSC and standard DSC techniques, *Polym. Test.*, 29, (2010), 759–765.

[250] B. Garnier, A. Sommier, Thermal property measuremens during cure of thermoset resins using steady periodic conditions, *J. Reinf. Plast. Compos.*, 21, (2002), 1193–1203.

[251] Guidance on technology readiness levels, UK Government, (2019). available: https://www.gov.uk/government/news/guidance-on-technology-readiness-levels (accessed September 19, 2019).

APPENDICES

APPENDIX A: FEA MODELLING THE VASCULAR CURE SETUP

A.1 Fortran code for the HETVAL subroutine

```
1    *USER  SUBROUTINES
2         SUBROUTINE HETVAL(cmname,temp,time,dtime,statev,flux,
3     1              predef,dpred)
4        INCLUDE 'ABA_PARAM.INC'
5        CHARACTER*80 cmname
6        DIMENSION temp(2),statev(1),predef(*),time(2),flux(2),
7     1        dpred(*)
8  C
9             FLUX(2)=0
10 C
11            if(statev(1).ge.0.89)then
12                FLUX(1)=0
13            else
14 C
15            dbdt=(7.257E7*exp(-78500/(8.314*(TEMP(1))))*((0.89-statev(1))**0.69))
16     &  +(1.199E7*exp(-69200/(8.314*TEMP(1)))*(statev(1)**0.75)
17     &  *((0.89-statev(1))**1.14))
18            fluxresin=((333E3)*2.15E3)*dbdt
19            statev(1)=statev(1)+dbdt*DTIME
20            FLUX(1)=0.43*fluxresin
21            end if
22        RETURN
23        END
24
```

Standard HETVAL format

If degree of cure is greater than 0.89, the reaction is complete therefore no flux- do not continue

Rate of cure – given by the cure kinetic model- Chapter 5

Calculation of heat flux- Section 7.3.1.1, Equation 28.

Final flux with 57% fibre volume in composite laminate (determined from burn off test following ASTM standard D2584 − 18)

Update degree of cure following this time step

A.2. Meshing of the FEA model

The sectioning of the part imposed on the model for the mesh generated to conform to quad element shapes, minimising distortions.
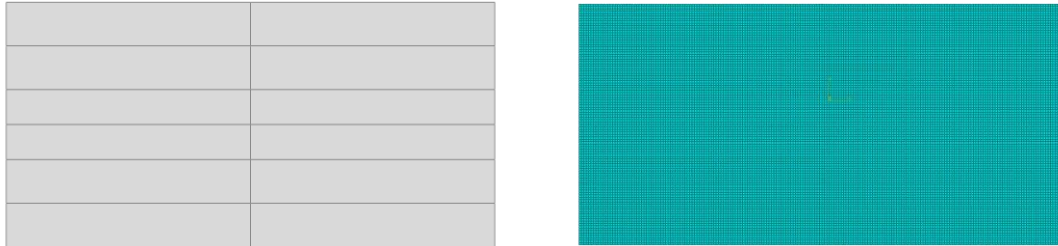
No vascule model

Figure A2.182: Images from FEA model with no vascule: a) partitioning b) mesh.

The partitions correspond to the through thickness location of the thermocouples and thus their intersection with the central vertical partition marks the position of the thermocouple which can easily be selected as a nodal element. Figure A2.1, shows the partitioning of the FEA model and the subsequent mesh.
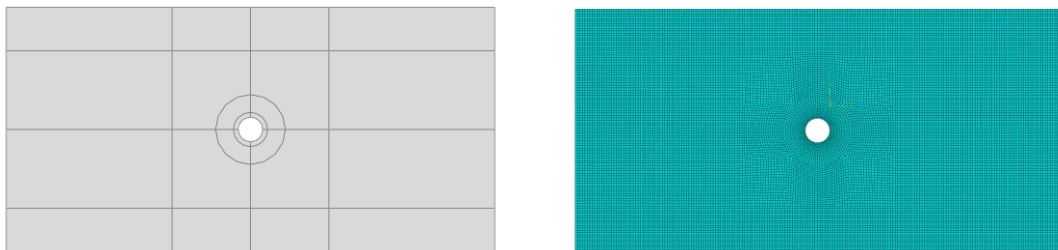
Vascule model

Figure A2.2: Images from FEA model with central vascule: a) partitioning b) mesh.

For the FEA model with a central vascule, partitioning was required to maintain quad elements over the part, as shown in Figure A2.2. These partitions are critical to prevent large distortions in the elements at the vascule location. So, some of these partitions are placed to help to minimise these/ minimise their effect over the whole part. As well as having partition intersections which as previously said can be used as the nodal elements for allowing data at the thermocouple locations to be selected.

APPENDIX B: FDA MODEL VALIDATED AGAINST THE FEA MODEL

As the FEA model had been initially used to predict the effect of the vascule placement, working in collaboration with O'Donnell to develop an FDA model which could be used more robustly to optimise the vascule temperature profile and placement within a part was sort after. The initial steps looked to ensure the FEA and FDA models matched in the predicted values to ensure there was no errors between the two which were using the same data inputs.

To do this the temperature data at each of the thermocouple locations was compared between the two models. This showed that they both predicted the same peak exotherms with matching curves, thus showing that the models were comparable and therefore the FDA model could be used to optimise the cure processes. This was also observed by looking at the temperature distribution in visual thermal mapping, as shown in Figure B.1, the same response was seen in both the FEA and FDA in both configurations. Therefore, the FDA could be used as an extension of the work conducted herein to allow for optimisation of the setup.

As already highlighted the FDA currently has the same limitations as the FEA, in terms of its oversimplification in the boundary conditions and the material property inputs, these limitations may be explored in future work.
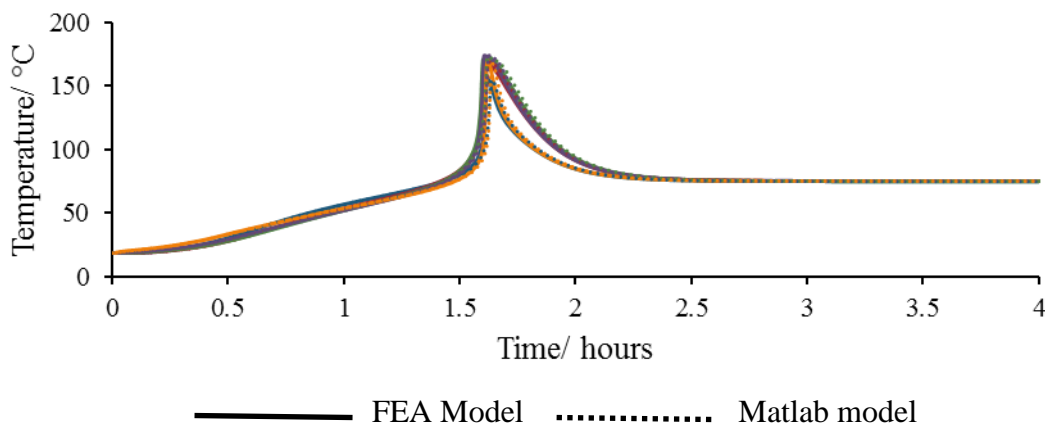

Figure B.1: Plot of the temperature profiles at the thermocouple positions for both the FEA and FDA (matlab) simulations with no vascule.